UNIVERSITY OF SOUTHAMPTON

FACULTY OF ENGINEERING, SCIENCE & MATHEMATICS

OPTOELECTRONICS RESEARCH CENTRE

Measurement of the local optical phase and amplitude in photonic devices using scanning near-field microscopy

James Christopher Gates

Submitted for the degree of Doctor of Philosophy

September 2003

UNIVERSITY OF SOUTHAMPTON

ABSTRACT

Optoelectronics Research Centre

Doctor of Philosophy

Measurement of the local optical phase and amplitude in photonic devices using scanning near-field microscopy.

By James Christopher Gates

This thesis presents the optical characterisation of various photonic devices using scanning near-field microscopy (SNOM). The SNOM technique has a unique capability of achieving a resolution beyond the diffraction limit. Placing the SNOM into the arm of a heterodyne interferometer also enables the measurement of both the optical phase and amplitude in the near infrared.

In this work three different photonic devices are investigated. The optical field distribution within a fibre Bragg grating is investigated as a function of wavelength. This work details the direct observation of the spatial shift of the standing wave across the stop band of a fibre grating. The shift is an explicit feature of fibre Bragg gratings and has previously only been theoretically predicted. The thesis also details three analytical techniques for measuring the microscopic loss of planar or channel waveguides. Two of the techniques are experimentally tested. The techniques exploit a standing wave generated within the waveguide, the visibility of the standing wave provides sufficient information to determine to loss between two points. The present limitations of the techniques are presented. The SNOM technique has also been applied to the measurement of a large mode holey fibre. The work details the accurate characterisation of the mode at the end face of the fibre and as it propagates into free space. The results are compared to theoretically predicted modes.

"I can't get no sleep"

Faithless, from the song *Insomnia.*

Acknowledgements

With some conviction I can say I've had fun in my last four years in the ORC. And with additional conviction I can also say its been hard work. But without the support and guidance of many people it would have been impossible and to all those I give my thanks.

An exceptionality big thanks you goes to the EPSRC and the ORC for their financial support and for putting the "fun" in funding.

I also like to thank Professor Michael Zervas for his helpful discussions, Charlie Tai for providing the potassium ion exchanged waveguides and Tanya Monro for the holey fibre modelling.

A big thanks goes to: Steve, Tim and Muggers for always dragging me down the pub; the office guys John, Peter, Ed and Chris for our intellectual deliberations? Rob and Barry for keeping an eye on me; Bill for his exceptional amount of patience and guidance; Joyce for all the jobs; Chris for whom there isn't enough whisky in the world to thank, my parents for all their support and of course Bryony who despite everything still cooks my dinner and washes my pants, a true angel. Cheers!

Contents

Chapter 1

Introduction

1.1 Chapter introduction

The invention of the optical microscope at the beginning of the seventeenth century was a crucial step in the development of modern science. From the 1660's Antoni van Leeuwenhoek (1632-1723) had began to work with single-lens microscopes. With this simple tool he was the first to observe blood corpuscles, the structure of nerves and microorganisms. He revolutionized the way in which people perceived the world around us giving rise to a new branch of science, microbiology. Since these initial discoveries the microscope has seen continual development and has been used as a standard tool by all disciplines of science. However due to diffraction, the resolution of the conventional optical microscope will always be fundamentally limited.

The 1980's saw the introduction of a new generation of microscopy, scanning probe microscopy (SPM). These systems enable far higher resolution than conventional techniques due to the exploitation of the near-field. They employ local probes that interact with the near-fields which exist in immediate proximity to the surface of materials. The optical SPM known as Scanning Near-field Optical Microscopy (SNOM) exploits the optical

evanescent fields at the materials surface. As the evanescent field is not propagating, diffraction does not occur and thus subwavelength resolution can be achieved. In fact the resolution of SPM techniques is limited only by the size of the local probe.

Characterisation is an essential part of the development of photonic devices. The combination of a high resolution microscope with a interferometer is ideally suited for the investigation of photonic materials. This thesis presents investigations of the electric field distribution of several photonic devices. This chapter starts by introducing the concepts this work is based upon and concludes by giving an summary of the following chapters.

1.2 Scanning near-field optical microscopy

In 1926 Synge [1] postulated that it would be possible to surpass the optical diffraction limit by bringing an aperture within one optical wavelength of the surface. An image could be generated by scanning the aperture across the surface and at each point recording the optical field. However the technological requirements of the system were far too advanced for the time. In the 1980's the Scanning Tunnelling Microscope (STM) was developed and with it the tools to create the system that Synge had suggest some 60 years earlier. The technique was defined as scanning near-field optical microscopy and is affectionately abbreviated to SNOM.

1.3 Interferometer techniques

Conventional SNOM experiments measure the optical information via a form of photodetector. The signal generated by these detectors is proportional to the incident photon flux and are therefore unable to measure the optical phase. The SNOM system used in this thesis adopts an heterodyne interferometer originally proposed by Balistreri *et al.* [2]. This elegant sys-

tem permits the simultaneous measurement of the magnitude and relative phase of the optical electric field. The heterodyne detection also increases the sensitivity of the detection system assisting research into the near infrared.

1.4 Characterisation of photonic devices

An extremely important part of the fabrication of photonic devices is the characterisation. As devices become increasingly smaller, the need for a high resolution characterisation tool becomes evident. Most characterisation methods rely on macroscopic techniques that investigate either the input/output dependence or imaging of the far-field mode profile. These results are then compared with theoretical models to acquire the average parameters of the system. However these methods do not show the individual mechanisms which occur inside the structure. The unique capabilities of SNOM provide an ideal tool for the measurement of the localised features of photonic devices. This thesis applies an interferometric SNOM system to analyse three different photonic devices.

1.4.1 Waveguide analysis with SNOM

An optical waveguide is the fundamental component of photonic devices. Optimisation of waveguides requires an accurate knowledge of the refractive index and optical fields propagating within the waveguide. Conventional optical microscopy provides an efficient method of imaging the modal properties of the waveguides, however it can only indirectly tell us about the electric field distribution inside the device. It is also desirable to gain information about the effects of fabrication defects and their associated losses. Conventional microscopy can provide useful information by imaging the surface scattering of the optical field of a waveguide [3]. However the resolution of this method is limited by diffraction and is only ap-

plicable to lossy waveguides. Characterisation of optical waveguides with SNOM allows many of these conventional limitations to be surpassed.

Reflection mode SNOM is capable of imaging the local refractive index of a waveguide [4], however it is unable to measure the optical field at the same time and is difficult to implement. Another variation of SNOM, photon scanning tunnelling microscopy (PSTM), enables both the local refractive index and optical field to be imaged. This is achieved by sampling the evanescent field of the mode propagating through the waveguide and provides non-invasive imaging of the optical field with sub-wavelength resolution. The first study of optical waveguides using this technique was presented by Tsai *et al.* in 1990 [5]. This work showed that measurement of the evanescent field decay length could be used to determine the local refractive index [6,7]. This technique was further developed by including a height modulation of the probe, to produce a direct method of mapping the local index changes on a surface [8].

The work presented in chapter 5 uses the SNOM technique to investigate the properties of potassium ion exchange waveguides. The investigation focuses on the determination of the microscopic losses of the waveguides by measuring the visibility of a standing wave excited within the waveguide.

1.4.2 Analysis of fibre Bragg gratings using SNOM

Fibre Bragg gratings are one of the most important components used in the telecommunication industry [9]. Characterisation of these components are usually achieved by the measuring the gratings transmission and reflection spectra. Information about the structure of the grating is obtained by a comparison with the theoretical models. Various other techniques can be used to analyse the index modulation [10]. However these techniques do not directly measure the sub-wavelength information about the refractive index profile or the electric fields within the grating.

As part of a larger investigation into the potential applications of PSTM, Tsai *et al.* showed that it was possible to image the intensity distributions at the core cladding interface of a fibre Bragg grating [11]. A more comprehensive study of fibre Bragg gratings was completed by Mills *et al.* [10,12]; showing both the refractive index modulation and the intensity distribution in a fibre Bragg grating. Chapter 4 presents an extension of this work. The development of the SNOM system permits an investigation of the gratings at their design wavelength in the near infrared. The work concentrates on the investigation of the optical field distributions within the grating, as a function of wavelength.

1.4.3 Characterisation of microstructured fibres with SNOM

Microstructured fibres present a novel method of guiding light, the diversity of the structures gives them unique optical properties [13]. As a result the topic has generated acute scientific and commercial interest in recent years. However the same properties that make them desirable also make them difficult to characterise using conventional methods. A prior investigation has proven SNOM to be well suited for the characterisation of microstructured fibres [14], showing that the technique is capable of achieving an accurate profile of the refractive index and optical mode.

The work presented in chapter 6 shows an extension of this work, permitting direct characterisation of the optical amplitude and phase of the propagating mode at telecomumications wavelengths.

1.5 Outline of thesis

This section outlines the contents of the future chapters.

1.5.1 Chapter 1 - Introduction

This chapter introduces the concepts and techniques used in this work. Along with a summary of each of the chapters.

1.5.2 Chapter 2 - Theory

An important role in SNOM is the interpretation of the collected data, thus this chapter commences by giving a brief account of the physics of near-field imaging. It also outlines the basic underlying principles of the SNOM operation, including height regulation of the near-field probe and the interferometric detection system.

1.5.3 Chapter 3 - Construction and analysis of the SNOM system

To acquire the data used in this thesis a scanning near-field optical microscope was developed with a complementing heterodyne detection system. This chapter presents an explanation of the basic SNOM arrangement, including details on the fabrication and characterisation of the SNOM probes. The heterodyne detection system is also described and the chapter concludes by characterising the system.

1.5.4 Chapter 4 - Investigation of fibre Bragg gratings

This chapter describes an investigation using the SNOM technique to image the standing waves excited within fibre Bragg gratings. The chapter commences by giving a brief introduction to fibre Bragg gratings and the motivation of the work. This is followed by a description of the investigated sample including details of its fabrication. The remaining part of the chapter presents the results and analysis of the research.

1.5.5 Chapter 5 - Investigation of single mode waveguides

This chapter details the work performed on the characterisation of single mode waveguides. The work concentrates on the development of a technique capable of measuring the microscopic loss of a waveguide. The chapter embarks by describing the proposed technique followed by details of the waveguides chosen to validate the technique. The SNOM results are presented including a discussion of the limitations of the technique with the current system.

1.5.6 Chapter 6 - Investigation of holey fibres

This chapter presents work on the characterisation of a large mode holey fibre. The chapter includes an introduction to holey fibres and a description of the mechanism responsible for the confinement of the mode. The electric field distribution of holey fibre mode is fully characterised including the effects of the propagation of the mode. The SNOM results are presented and compared to theoretical predictions.

1.5.7 Chapter 7 - Conclusions

This chapter provides a summary of the work presented in the thesis, including details of the most significant results.

1.6 References

[1] E.H. Synge. "A suggested method for extending microscopic resolution into the ultra-microscopic region". *Philosophical Magazine*, 6:356–362, 1928.

[2] M.L.M. Balistreri, J.P. Korterik, L. Kuipers, and N.F. van Hulst. "Phase Mapping of Optical Fields in Integrated optical waveguide structures.". *Journal of Lightwave Technology*, 19(8), 2001.

[3] G. J. Veldhuis, J. H. Berends, and P. V. Lambeck. "Design and characterization of a mode-splitting Psi-junction". *Journal of Lightwave Technology*, 14(7):1746–1752, 1996.

[4] M. Svalgaard, S. Madsen, J. M. Hvam, and M. Kristensen. "Direct characterization of ultraviolet-light-induced refractive index structures by scanning near-field optical microscopy". *IEEE Photonics Technology Letters*, 10(6):848–850, 1998.

[5] D. P. Tsai, H. E. Jackson, R. C. Reddick, S. H. Sharp, and R. J. Warmack. "Photon Scanning Tunneling Microscope Study of Optical Wave- Guides". *Applied Physics Letters*, 56(16):1515–1517, 1990.

[6] E. Bourillot, F. Defornel, J. P. Goudonnet, D. Persegol, A. Kevorkian, and D. Delacourt. "Analysis of Photon-Scanning Tunneling Microscope Images of Inhomogeneous Samples - Determination of the Local Refractive- Index of Channel Wave-Guides". *Journal of the Optical Society of America A-Optics Image Science and Vision*, 12(1):95–106, 1995.

[7] A. G. Choo, M. H. Chudgar, H. E. Jackson, G. N. Debrabander, M. Kumar, and J. T. Boyd. "Photon Scanning-Tunneling-Microscopy of Optical Channel Wave- Guides". *Ultramicroscopy*, 57(2-3):124–129, 1995.

[8] D. P. Tsai, C. W. Yang, S. Z. Lo, and H. E. Jackson. "Imaging local index variations in an optical waveguide using a tapping-mode near-field scanning optical microscope". *Applied Physics Letters*, 75(8):1039–1041, 1999.

[9] K. O. Hill and G. Meltz. "Fiber Bragg grating technology fundamentals and overview". *Journal of Lightwave Technology*, 15(8):1263–1276, 1997.

[10] J.D. Mills. *An investigation of Phase-Mask Diffraction Patterns And Fibre Bragg Gratings With Scanning Near-Field Optical Microscopy*. PhD thesis, University of Southampton, 2001.

[11] D. P. Tsai, J. Kovacs, and M. Moskovits. "Applications of Apertured Photon Scanning-Tunneling-Microscopy (APSTM)". *Ultramicroscopy*, 57(2-3):130–140, 1995.

[12] J.D. Mills, C. W. J. Hillman, W. S. Brocklesby, and B.H. Blott. "Evanescent field imaging of an optical fibre Bragg grating". *Applied Physics Letters*, 75(26):4058–4060, 1999.

[13] T. M. Monro and D. J. Richardson. "Holey optical fibres: Fundamental properties and device applications". *Comptes Rendus Physique*, 4(1):175–186, 2003.

[14] C. W. J. Hillman, W. S. Brocklesby, T. M. Monro, W. Belardi, and D. J. Richardson. "Structural and optical characterisation of holey fibres using scanning probe microscopy". *Electronics Letters*, 37(21):1283–1284, 2001.

Chapter 2

Theory

2.1 Chapter introduction

This chapter outlines the physical mechanisms and theoretical analysis required to understand the work presented in this thesis. The chapter is split into three sections. The first section (2.2) describes the basic principles and models behind the implemented SNOM system including details of the heterodyne detection system used to analysis the optical information. Section 2.3 addresses the imaging of counter propagating waves and details the Fourier transform technique used in their characterisation. The chapter concludes by describing the basic theory behind the operation of waveguides and fibre Bragg gratings.

2.2 SNOM theory

2.2.1 The resolution limit

Conventional optical microscopy is limited not by any technical limitation but by the fundamental physical restriction, diffraction. The limit was first defined by Abbe in 1873 [1] and later revised by Lord Rayleigh to give the

familiar format,

$$\delta x \geq \frac{1.22\lambda}{2n\sin(\frac{\theta}{2})} \tag{2.1}$$

where δx is the feature separation distance, λ is the wavelength of the electromagnetic radiation, n is the refractive index of the imaging medium and θ is the objective collection angle. To go beyond this resolution limit it is necessary to move from the conventional far-field to a near-field [1] regime.

To understand the relationship between near and far-field imaging, the angular spectrum model is introduced. The model gives a useful insight into the fields generated above a sample and hence the field collected by a near-field probe.

2.2.2 The angular spectrum model

The angular spectrum model provides a perception of the optical fields generated by a source and explains the nature of diffraction. This section presents the derivation of the angular spectrum model using scalar diffraction theory to introduce the origin and some of the physical properties of evanescent fields. The proof shown in this section is derived from references [2,3].

Consider a two dimensional spatially limited object with an optical property $f(x, y, 0)$, where the optical property could be transmittance or reflectance. The object may be described in the form of a two dimensional Fourier integral,

$$F_0(u, v) = \int \int_{-\infty}^{+\infty} f(x, y, 0)e^{-i2\pi(ux+vy)}dydx. \tag{2.2}$$

[1] In this thesis the term near-field is used in association with evanescent fields, rather than the definition used in classical geometrical optics.

where u and v are all the possible values of the spatial frequencies of the object. F_0 is the Fourier transform of the object and hence $f(x, y, 0)$ can also be written as an inverse Fourier transform of its spectrum:

$$f(x, y, 0) = \frac{1}{2\pi} \int \int_{-\infty}^{+\infty} F_0(u, v) e^{i2\pi(ux+vy)} du dv. \tag{2.3}$$

The function $f(x, y, 0)$ represents the optical property of the object. It can therefore be assumed that the electric field $U(x, y, 0)$ in close proximity to the object will be directly proportional to the function $f(x, y, 0)$, hence:

$$U(x, y, 0) \propto f(x, y, 0) \tag{2.4}$$

Uniting equations 2.3 and 2.4 it is possible to define the electric field at the object, as shown:

$$U(x, y, 0) \propto \int \int_{-\infty}^{+\infty} F_0(u, v) e^{i2\pi(ux+vy)} du dv. \tag{2.5}$$

As the absolute magnitude is not relevant in these relationships, factors such as the 2π in equation 2.3 have been neglected.

Equation 2.6 recalls the equation for a unit amplitude plane wave,

$$B(x, y, z) = e^{ik(\alpha x+\beta y+\gamma z)} \tag{2.6}$$

where the direction cosines are related through,

$$\gamma = \sqrt{1 - \alpha^2 - \beta^2} \tag{2.7}$$

and k is the wavevector. It is possible to observe that the electric field described in equation 2.5 may be regarded as the superposition of a set of plane waves, specified by the variables:

$$\begin{aligned} \alpha &= \lambda u \\ \beta &= \lambda v \end{aligned} \tag{2.8}$$

Revising equation 2.5 in terms of the variables stated in 2.8 gives:

$$U(x,y,0) \propto \int\int_{-\infty}^{+\infty} F_0\left(\frac{\alpha k}{2\pi}, \frac{\beta k}{2\pi}\right) e^{ik(\alpha x+\beta y)} d\alpha d\beta. \tag{2.9}$$

Equation 2.9 expresses the objects electric field as a superposition of plane waves, each with a corresponding spatial frequency and direction cosine. Hence this relation is referred to as the angular spectrum.

To gain more insight into this model it is necessary to observe the propagation of the angular spectrum, to enable this, the z dependence must be included:

$$U(x,y,z) \propto \int\int_{-\infty}^{+\infty} F\left(\frac{\alpha k}{2\pi}, \frac{\beta k}{2\pi}, z\right) e^{ik(\alpha x+\beta y)} d\alpha d\beta. \tag{2.10}$$

The solutions to equation 2.10 must also fulfil the Helmholtz equation:

$$\nabla^2 U + k^2 U = 0 \tag{2.11}$$

Application of the Helmholtz equation to relation 2.10, yields a solution in the form:

$$F\left(\frac{\alpha k}{2\pi}, \frac{\beta k}{2\pi}, z\right) \propto F_0\left(\frac{\alpha k}{2\pi}, \frac{\beta k}{2\pi}\right) e^{\left[ikz\sqrt{(1-\alpha^2-\beta^2)}\right]} \tag{2.12}$$

The result provides a interesting relation between each plane waves' capability to propagate and the value of the direction cosines, α and β. If $\alpha^2 + \beta^2 < 1$ the effect is a change in the relative phase between the plane wave components. This is intuitive as each plane wave component propagates at a different angle and hence has a different path length between the planes of observation. For condition $\alpha^2 + \beta^2 = 1$ the corresponding plane wave propagates parallel to the object plane. However when $\alpha^2 + \beta^2 > 1$ the plane wave components are exponentially attenuated in the z-direction and are referred to as evanescent waves. These correspond to high frequency components. It is therefore apparent that for the measurement of any sub-wavelength features it is necessary to collect the evanescent components.

As previously stated the angular spectrum model is derived using scalar theory. However the evanescent field described here is predicted under

the same conditions in which the scalar theory is ambiguous. Despite this the theory provides an extremely useful insight into the role of evanescent and propagating components. An exact model for quantitative analysis may be derived from a full vectorial approach or by solving Maxwell's equations.

2.2.3 Principles of SNOM

There are three basic criteria for collecting sub-wavelength optical information. Foremost a sub-wavelength probe is required. Secondly a method of monitoring and maintaining the probe in proximity with the sample, and finally a method of positioning the probe with nanometer precision. This section describes the basic theory governing these mechanisms.

2.2.3.1 Light collection mechanism

The most important component of a scanning probe microscope and hence SNOM is the probe. A great deal of time and effort has been devoted to the fabrication and characterisation of the probes [4, 5].

The probe or tip can act in two modes: a nano-collector and a nano-emitter. The nano-collector acts as a scattering center, converting the non-radiating optical components of the sample into propagating components. The tip is sufficiently small enough to avoid integration effects, and hence its size defines the optical resolution of the system. By reciprocity the nano-collector can also act as a nano-emitter. The non-radiating components of the nano-source scan the sample, and are converted into propagating components able to be collected by a detector.

In general the probe tends to be in the form of either a tapered optical fibre or a silicon cantilever. Other probes have been developed which employ laser trapped particles as a probe [6, 7], however the complexity of the system deems it less practical.

In this thesis the tapered fiber probes are exclusively used as a nano-collector. The work presented in chapter 4 employs a bare tapered fiber and exploits the exponential nature of the evanescent field to obtain high resolution. The remainder of the work presented in chapters 5 and 6 employ tapered fibres preferentially coated with aluminium. The very apex of the probe is left un-coated to produce an aperture. This prevents propagating light from coupling into the probe via the side walls, and hence reducing the resolution.

The following sections outline the light collection mechanisms behind coated and un-coated probes. Basic models are presented which although do not give an exact solutions, extract a valuable insight into the working of the probe. The fabrication method used to produce probes for the work presented here is shown in section 3.1.1.

2.2.3.2 Un-coated probes

For an un-aluminised probe the simplest model is to consider the apex as a polarisable dipole. When placed within a non-radiating field it is excited and generates both propagating and non-propagating optical fields [8]. The propagating components are guided to the detector via the fibre. The system is therefore characterized by its polarisability α. An evanescent field $\mathbf{E}$ induces an electric dipole $\alpha\mathbf{E}$ and the detected intensity I_d is given by, [9]

$$I_d(x,y,z) = \frac{\omega^4}{96c^3}|\alpha|^2[(|E_x|^2 + |E_y|^2)(16 - 15\cos\alpha - \cos 3\alpha) + \\ +|E_z|^2(16 - 18\cos\alpha + 2\cos 3\alpha)] \quad (2.13)$$

where α is the taper angle of the tip. ω is the frequency of the incident light and c is the speed of light in a vacuum. For tapered fibre probes the apex is often considered to approximate a sphere of radius R and dielectric constant ϵ_{tip}, whose polarisability can be written as:

$$\alpha = \left(\frac{\epsilon_{\text{tip}} - 1}{\epsilon_{\text{tip}} + 2}\right) R^3 \quad (2.14)$$

This model is considered to be a first approximation of the system. More rigorous models have been developed that are able to properly account for the finite size of the tip and the tip-sample coupling. Barchiesi *et al.* have addressed the issue of the finite size of the tip by applying Mie theory [10]. However in this model the probe plays a passive role, collecting energy in the near-field but without interacting with it. Full models where the tip and sample are always associated have been developed by many groups. The general approach towards these models is to numerically solve Maxwell's equations for the specific system. One of the most popular numerical techniques is the Finite-Difference Time-Domain method (FDTD) [11,12]. A review of the different modelling techniques is given in reference [13].

2.2.3.3 Coated probes

The concept of a coated probe was first suggested in a private communication between Synge and Einstein, in which a metalised quartz cone with a metal free extremity was proposed as a near-field probe. The suggestion was developed from a previous proposal of a nanometer aperture in an opaque screen. This basic system can be used as an approximation and facilitates its theoretical treatment. The first theoretical analysis of such a system was conduced by Bethe [14], in which he defined the transmission coefficient of a sub-wavelength hole in a infinitely thin, perfectly conducting screen. This was later revised by Bouwkamp [15] to correct for small errors. The theory predicts that the transmission of a sub-wavelength hole scales as d^4, where d is the diameter of the aperture [16]. The Bethe-Bouwkamp model has been further developed to investigate the optical properties of near-field optical probes [17] [18] [19]. Roberts [18] showed that by accounting for the tip geometry and the non-ideal conduction of the probe coating, the transmission follows a d^6 relationship, resulting in extremely low transmission coefficients. Typically aperture diameters of 60 to 100 nm yield transmissions of 10^{-4} to 10^{-7} respectively [4].

2.2.3.4 Configuration of the SNOM technique

There are several different configurations of the SNOM technique, the distinguishing feature is the mode of illumination [20]. The configuration generally employed in this thesis is that of the photon scanning tunnelling microscope (PSTM) first proposed by Reddick *et al.* in 1989 [21]. In this configuration the near-field probe acts as a nano-collector; collecting the evanescent fields generated by total internal reflection (TIR). In these initial experiments the evanescent fields were generated at the interface of a prism. However within a year it was also shown that the technique could be used to measure the evanescent fields generated by the optical modes in a waveguide [22].

Chapter 6 images the electric field distribution of the homogeneous waves of a holey fibre mode. This employs a less stringent imaging technique and does not require the probe to be in close proximity with the sample.

2.2.3.5 Height regulation

Owing to the exponential dependence of the evanescent field, the separation between the near-field probe and the surface must be kept to nanometers. Also the distance must be maintained to prevent the tip from hitting and surface and being damaged. This requires a technique of detecting the surface and a method of spatially controlling the probe with nanometer accuracy. The spatial control is provided by piezo-electric actuators which were initially developed for scanning tunnelling microscopy. The surface detection has been achieved using mechanisms such as: electron tunnelling, various optical systems, and a technique called shear force detection.

2.2.3.6 Shear force detection

The most exploited method of height regulation used in SNOM is the shear force method. Of all the methods it is the least stringent on the properties of the sample. The method was first proposed by Betzig *et al.* [23], and method employs a fibre tip oscillating at its resonance frequency. As the tip approaches the surface the oscillation amplitude is damped. This interaction occurs within tens of nanometers of the surface. A variety of mechanisms and combinations are proposed to be responsible for the interaction between the probe and sample. Initially the interaction was explained by a mixture of various van der Waals' and capillary forces [24] [25]. At ambient room conditions contamination layers are considered to play the dominant role [26]. However shear force height regulation has been observed in vacuum and liquid helium [27], therefore collapsing the argument for a purely contamination layer driven interaction. Accordingly Gregor *et al.* [27] proposed a nonlinear bending force as the primary mechanism in cryogenic conditions.

In this mechanism the force is generated by the tapping and bending of the probe on the surface [28, 29, 30]. More recent work [31, 32, 33, 34, 35] confirms that in addition to the nonlinear bending force, water layers govern at ambient conditions. The diversity of the results from many groups implies that the shear force system, sample and environmental conditions determine the dominance of the mechanisms involved in the surface interaction.

The interaction length of the damping force is typically 10 to 25 nm depending on the sensitivity of the detection system. Thus the height can be regulated between the point of contact with the surface and the minimum detectable damping force. The resolution of the technique is strongly dependent on the system, specifically the feedback system. An investigation by the van Hulst group in the Netherlands has imaged DNA strands using shear force feedback, which showed the height of the DNA to be 1.4 ± 0.2

nm [36].

2.2.3.7 The scanning system

The final physical requirement for the SNOM system is a method of controlling the position of the probe with nanometer resolution. The development of the STM in the 1980's brought refined techniques for scanning on a nanometer scale. The methods generally utilise the piezo-electric properties of PZT (lead zirconate titanate) ceramics. In these materials an applied voltage results in a corresponding change in its dimensions. Today xyz translation stages are commercially available combining micrometer screw based translation with piezo-electric transducers.

2.2.4 Heterodyne detection technique

One of the main developments of the SNOM system presented in this thesis is the heterodyne detection system. This section presents the principles behind its operation and highlights the advantages of the technique. Since the development of the laser in the 1960's laser interferometry has been employed in science and industry to provide high accuracy measurements. Interferometers have the unique ability to measure the complex amplitude of an optical field, in comparison to standard photo-detection which is only sensitive to photon flux. The technique involves the detection of the superposition of an optical signal and a coherent reference wave.

There are two generally used interference measurement techniques, homodyne and heterodyne. The homodyne system is the technique used in traditional optical interferometers such as the Michelson interferometer. In such a system the signal and reference signals have the same frequency. In the heterodyne method the signal and reference signals are at different frequencies. This is the same technique used in FM (frequency modulated)

radio transmitters and receivers. Both techniques enable the detection of the optical phase, however the heterodyne technique also provides low noise gain of the optical signal. The following section explains the principles of the technique.

2.2.4.1 The principle

A heterodyne system requires a small frequency shift between two interfering waves. Mixing of these two waves generates an amplitude modulation at the beat frequency $\Delta\nu$. Figure 2.1 shows a typical optical heterodyne interferometer.

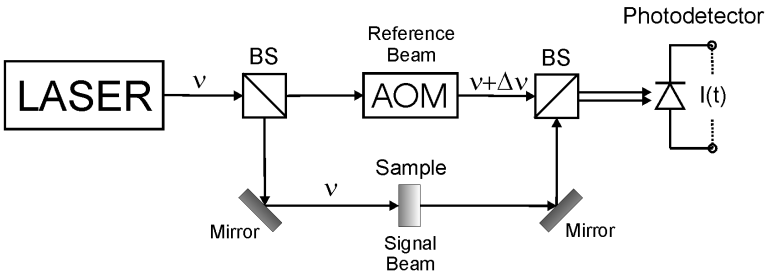

Figure 2.1: An example of a optical heterodyne interferometer.

The laser source is split using a beam splitter (BS) into a signal arm and a reference arm. The acoustic optical modulator (AOM) is used to introduce a frequency shift ($\Delta\nu$) in the reference arm, while the signal beam passes through the object under investigation. The beams are then recombined using another beam splitter and measured using a photodetector. The subsequent signal contains information about the amplitude and phase of the optical signal.

The complex electric fields of the signal (E_{sig}) and reference (E_{ref}) beams can be defined as,

$$E_{\text{sig}} = A_{\text{sig}} e^{i(2\pi\nu t)} \tag{2.15}$$

$$E_{\text{ref}} = A_{\text{ref}} e^{i(2\pi(\nu+\Delta\nu)t+\beta)} \tag{2.16}$$

A_{sig} and A_{ref} are the electric field amplitudes of the signal and reference beams, respectively. β is the phase difference between the optical paths of the signal and reference beams, it contains contributions from environmentally induced phase drift. The combined signal of the two beams is $E = E_{\text{ref}} + E_{\text{sig}}$ and hence the intensity I, is given by:

$$I = |E_{\text{sig}} + E_{\text{ref}}|^2 = A_{\text{sig}}^2 + A_{\text{ref}}^2 + A_{\text{sig}}A_{\text{ref}}\left[e^{i(2\pi\Delta\nu t+\beta)} + e^{i(-2\pi\Delta\nu t-\beta)}\right] \quad (2.17)$$

Using the expression $2\cos(x) = e^{ix} + e^{-ix}$, equation 2.17 can be simplified:

$$I = A_{\text{sig}}^2 + A_{\text{ref}}^2 + 2A_{\text{sig}}A_{\text{ref}}\cos(2\pi\Delta\nu t + \beta) \quad (2.18)$$

Collection of the optical field on to an detector generates a photocurrent which is proportional to the incident photon flux and hence the intensity (I). Equation 2.18 therefore shows that the induced photocurrent oscillates at a beat frequency of $\Delta\nu$ with an amplitude of $2A_{\text{sig}}A_{\text{ref}}$. The information about the sample is given by the amplitude and phase (β) of this modulation.

Using a lock-in technique the amplitude and phase can be measured. The synchronous detection of the heterodyne signal using a lock-in amplifier, generates two electrical output signals,

$$\begin{aligned} X &= R\cos(\theta) \\ Y &= R\sin(\theta) \end{aligned} \quad (2.19)$$

where the R is proportional to the amplitude of the input signal, modulating at the reference signal frequency. θ is the phase difference between the input signal and the reference signal. If the reference signal is equal to the beat frequency $\Delta\nu$, and the input signal is proportional to the intensity given in equation 2.18, then the value R is proportional to the value $2A_{\text{sig}}A_{\text{ref}}$ and the phase (θ) is equal to β. The values R and θ can be derived from equations in 2.19:

$$\begin{aligned} R &= \sqrt{X^2 + Y^2} \\ \theta &= \arctan 2\left(\frac{Y}{X}\right) \end{aligned} \quad (2.20)$$

2.2.4.2 Gain of the heterodyne detection technique

As previously discussed the heterodyne technique enables the measurement of the complex electric field of an optical system. However, the heterodyne technique also provides a signal enhancement with a factor of $A_{\text{ref}}/A_{\text{sig}}$. Due to the relatively low optical throughput of SNOM probes mentioned in 2.2.3.3, high gain photo-detectors such as photomultipliers and avalanche photodiodes (APD's) are employed. The heterodyne system supplies an alternative technique to provide sufficient low noise gain, enabling detection in the near infrared region using InGaAs photodiodes. It can be seen from equation 2.18 that the gain is obtained by increasing the value of I_{ref}. If I_{ref} is sufficiently large the shot noise of the system dominates the Johnson noise. A mathematical treatment of the noise can be found elsewhere [37] [38].

2.2.5 Imaging artifacts

In all forms of microscopy there are parasitic effects that produce image features that are unrelated to the sample being imaged. These are referred to as artifacts. A significant task in microscopy is to distinguish, understand and if possible remove the artifacts. This section will outline the origins of the artifacts associated with PSTM. However it should stressed that the work formed in this thesis is not impeded by many of the discussed artifacts, due to careful selection and processing of the samples. The discussion will be separated into two sections, artifacts associated in scanning probe microscopy and those specific to PSTM. The latter will be predominately concerned with the misinterpretation of data due to channel mixing [39].

2.2.5.1 SPM artifacts

The basic artifacts associated with all SPM systems is scanning non- uniformities and tip convolution. Scanning non-uniformities come about due to the imperfect properties of the piezoelectric scanners, leading to distorted images. These effects are compensated for with calibration of the stage, this will be addressed in section 3.1.3. Most scanning force microscopy artifacts are generated from a phenomenon called tip convolution. Each data point in a image represents a spatial convolution of the shape of the tip and the feature being imaged. Provided the tip is much sharper than the feature, the image data will approximate the feature being imaged [40]. In order to confirm the shape of a probe, the measured topography of a known sample may be used to deconvolve the shape of the probe.

2.2.5.2 PSTM artifacts

Artifacts specific to PSTM originate due to the imaging plane being undefined. The amplitude of the evanescent field at the surface of a sample varies exponentially with collection distance. Therefore motion perpendicular to the surface generates a correlation between the optical image and the topographical image. Comparison between the topographical and optical images enables these artifacts to be determined. Misinterpretation of the data occurs when the topographical image is not presented with the optical image [39]. Thus whenever appropriate the association topography data is presented with the optical data.

2.3 Imaging of counter-propagating fields

In chapters 4 and 5 the SNOM system is used to image the standing waves generated by the interference between two counter-propagating fields. In section 2.2.4.1 the response of the heterodyne system to a individual plane

wave was considered. The following section presents a simple model describing the complex electric field of a standing wave measured with the SNOM system.

The treatment is similar to that used in section 2.2.4.1. The evanescent field along the length of the waveguide can be described by two interfering plane waves. The electric field sampled by the probe is E_{sig} and is given by the expression,

$$E_{\text{sig}} = C_{\text{f}} A_{\text{f}} e^{i(2\pi\nu t - kx)} + C_{\text{b}} A_{\text{b}} e^{i(2\pi\nu t + kx + \gamma)} \tag{2.21}$$

where A_{f} and A_{b} are the electric field amplitudes of the forward and backward signal components. In this case x defines the absolute position along the waveguide. γ is the phase difference between the forward and backward components. C_{f} and C_{b} are the amplitude coupling coefficients of the forward and backward propagating fields respectively. These describe the amplitude coupling functions of the tip, and are a complex function of the tip-sample system [41]. The effects of the amplitude coupling functions is discussed in more detail in section 5.5.3. For the following discussion the coefficients are set equal to unity ($C_{\text{f}} = C_{\text{b}} = 1$). The polarisation state of the two interfering beams also defines the magnitude of the fringes. The difference in the state of the polarisation of the two beams can be defined by the angle ψ. The visibility of the interference fringes are then reduced by a polarisation overlap factor $\cos(\psi)$. In the following treatment the polarisation of the counter propagating fields are parallel ($\psi = 0, \pi$), thus the overlap factor is equal to unity and can be disregarded. The intensity of this standing wave (I_{sw}) is given by:

$$I_{\text{sw}} = |E_{\text{sig}}|^2 = A_{\text{f}}^2 + A_{\text{b}}^2 + 2A_{\text{b}}A_{\text{f}} \cos(2kx + \gamma) \tag{2.22}$$

The heterodyne detection requires a reference beam given by equation 2.16. The total electric field detected by the photo-detector is obtained by combining 2.21 and 2.16 as shown,

$$E_{\text{sig}} + E_{\text{ref}} = A_{\text{f}} e^{i(2\pi\nu t - kx)} + A_{\text{b}} e^{i(2\pi\nu t + kx + \gamma)} + A_{\text{r}} e^{i[2\pi(\nu + \Delta\nu)t + \beta]} \tag{2.23}$$

As in equation 2.15, β is the optical path difference between the signal and reference arms of the interferometer. Thus the total intensity becomes,

$$\begin{aligned} I = |E_{\text{sig}} + E_{\text{ref}}|^2 = A_{\text{f}}^2 + A_{\text{b}}^2 + A_{\text{r}}^2 + A_{\text{b}}A_{\text{f}}\cos(2kx + \gamma) \\ +2A_{\text{r}}A_{\text{b}}\cos(2\pi\Delta\nu t - kx - \gamma + \beta) \\ +2A_{\text{r}}A_{\text{f}}\cos(2\pi\Delta\nu t + kx + \beta) \end{aligned} \tag{2.24}$$

It is the signal modulated at the frequency $\Delta\nu$ that contains the desired information and therefore the DC signal is neglected. Applying the relationship $\cos(A \pm B) = \cos(A)\cos(B) \mp \sin(A)\sin(B)$. The intensity of the modulated signal I_{mod} can be resolved into two relative phases. As shown:

$$\begin{aligned} I_{\text{mod}} = 2A_{\text{r}}\{\cos(2\pi\Delta\nu t)[A_{\text{f}}\cos(kx + \beta) + A_{\text{b}}\cos(kx + \gamma - \beta)] - \\ \sin(2\pi\Delta\nu t)[A_{\text{f}}\sin(kx + \beta) + A_{\text{b}}\sin(kx + \gamma - \beta)]\} \end{aligned} \tag{2.25}$$

With inspection it is apparent that the lock-in outputs from the heterodyne detection system (X and Y) describe the two phases shown in equation 2.25. Thus:

$$\begin{aligned} X &\propto A_{\text{f}}\cos(kx + \beta) + A_{\text{b}}\cos(kx + \gamma - \beta) \\ Y &\propto -A_{\text{f}}\sin(kx + \beta) + A_{\text{b}}\sin(kx + \gamma - \beta) \end{aligned} \tag{2.26}$$

Describing equation 2.21 by its real and imaginary components gives the following expression:

$$\begin{aligned} Re[E_{\text{sig}}] &= A_{\text{f}}\cos(kx + \omega t) + A_{\text{b}}\cos(kx + \gamma - \omega t) \\ Im[E_{\text{sig}}] &= -A_{\text{f}}\sin(kx + \omega t) + A_{\text{b}}\sin(kx + \gamma - \omega t) \end{aligned} \tag{2.27}$$

As previously shown in section 2.2.4.1 optical heterodyne detection allows the complex amplitude of the optical signal to be deduced [38]. For this to be possible the relative path differences between the signal and reference beams caused by thermal drift (β) must remain constant. Changing the value of β alters the relative phase measured by the interferometer. The optical mixing of the interferometer transfers any change in the phase

of the optical signal to the relatively slowly changing beat frequency detected by the photodetector. A comparison between equations 2.26 and 2.27 supports this observation. It shows that the LIA outputs (X and Y) are proportional to the real and imaginary components of the standing wave if $\beta + 2n\pi = \omega t$ where n is an integer. Implying that if the interferometer is stable ($\frac{\delta\beta}{\delta t} = 0$) the components measured by the system correspond to the standing wave at a particular point in its optical cycle. A stable system can therefore be considered to detect a snap shot of the complex optical field at a particular time t, even though the measurement has a finite time.

2.3.1 Measurement of the relative amplitudes of counter-propagating fields

In chapters 4 and 5 the visibility of the standing wave will be used to characterise the samples. This section looks at the methods required to calculate the relative amplitudes of the forward and backward propagating modes.

The intensity due to the interference of two counter propagating fields of amplitude $\mathrm{A_f}$ and $\mathrm{A_b}$ is given by equation 2.22. The relation shows that the interference has a spatial period at half the wavelength of the light in the medium. The intensity of the standing wave varies as a function of $\cos(2kx + \gamma)$. In order to determine the magnitude of the two components it is obviously necessary to measure the intensity or electric field at its limits, i.e. $\cos(2kx + \gamma) = \pm 1$. This can be achieved by modulating one of the variables k, x and γ, the most convenient being the spatial modulation x. The x modulation can be achieved by scanning the probe along the optical axis of the waveguide, thereby providing the information to determine the relative magnitudes of the counter propagating modes.

2.3.1.1 Characterising the standing wave visibility

This section describes the method used to acquire the visibility of the standing wave from the SNOM images. The definition of the visibility ratio used in this thesis is the ratio $\mathrm{A_b}/\mathrm{A_f}$. A standard technique of determining this is to measure the maximum and minimum amplitudes of the oscillation. From this the relative amplitudes of the forward and backward propagating components may be derived and consequently the visibility. This is a valid technique in an ideal situation where the spatial frequency spectrum is composed of an individual frequency and the noise is negligible. However real data comprises typically of several discrete frequencies as a result of scattered light and topographical artifacts. It is therefore necessary to select only the spatial frequency components corresponding to the interference of the counter-propagating guided modes. To achieve this a fast Fourier transform (FFT) technique was used.

In order to assist the FFT technique the square of the electric field signal is used, the resulting signal is a pure sine wave. The data analysed will be a series of line scans, an ideal line scan of 1 μm period is shown in figure 2.2 (a).

The relative amplitudes of the two components is given in the figure caption. The discrete Fourier transform of the data in (a) is presented in (b), it shows the amplitude frequency spectrum of two components at 0 and 1 $\mu\mathrm{m}^{-1}$. The amplitude of these two peaks yields sufficient information to calculate the amplitude of the forward and backward components. The amplitudes are given by the expressions:

$$\begin{aligned} A_\mathrm{f} &= \frac{E_\mathrm{max} + E_\mathrm{min}}{2} \\ A_\mathrm{b} &= \frac{E_\mathrm{max} - E_\mathrm{min}}{2} \end{aligned} \tag{2.28}$$

where

$$\begin{aligned} E_\mathrm{max} &= \sqrt{A_\mathrm{DC} + A_\mathrm{AC}} \\ E_\mathrm{min} &= \sqrt{A_\mathrm{DC} - A_\mathrm{AC}} \end{aligned} \tag{2.29}$$

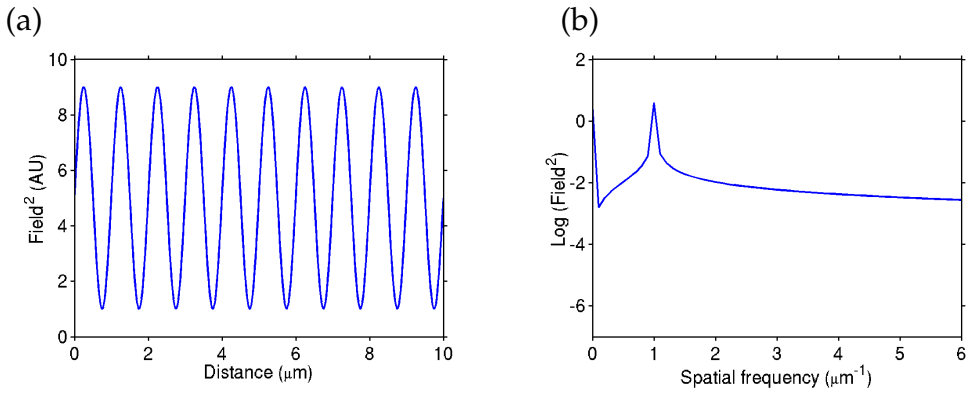

Figure 2.2: (a) Plot showing an ideal line scan of the electric field squared along the axis of the waveguide. The amplitude of the forward and backward propagating components is 2.0 and 1.0 respectively. (b) The discrete Fourier transform of (a) displaying its intensity spectrum. A log scale is used to display the lower amplitude features.

A_{DC} and A_{AC} are the amplitudes of the spectral components at 0 and 1 $\mu\mathrm{m}^{-1}$ respectively. In this experimental configuration the condition $A_{\mathrm{f}} \geq A_{\mathrm{b}}$ is always true. However in situations where there are no experimental limits on the values of A_f and A_b, determination of the dominant component can be acquired from the phase of the electric field. The discrete nature of the Fourier transform, results in a broadening of the frequency spectrum. Broadening is also increased if the number of periods sampled is a non-integer. This is demonstrated in figure 2.3 and is called leakage error.

The leaked power is spread over many nearby frequency bins, thus the measurement of the amplitude of an individual frequency component requires the integration over the entire peak. With real signals, summation of a frequency band results in an increased amount of noise and leakage from other components, and consequently an increased error in the measurement. The standard signal processing technique to reduce leakage is to multiply the data segment in the spatial domain by a window before performing the FFT [42]. The choice of window depends on the information desired from the frequency spectra. In this case a Hann or Hanning

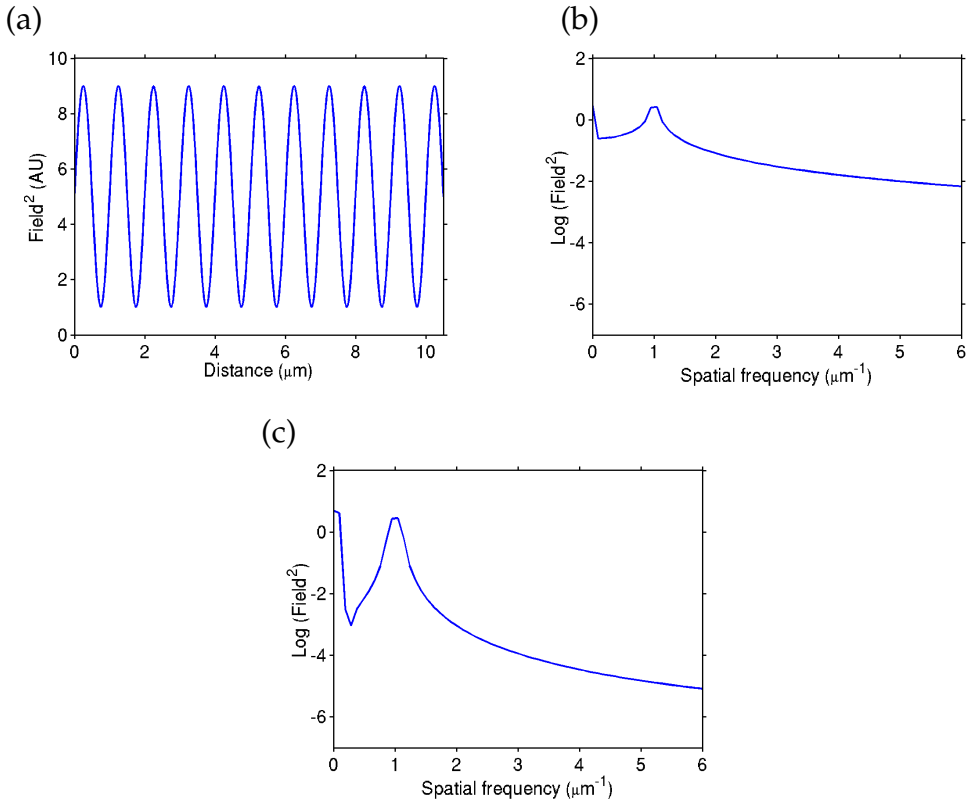

Figure 2.3: (a) Similar to figure 2.2, except the sampled data has a non integer number periods. (b) The FFT of (a) showing the increased leakage of the frequency spectrum. (c) The effect of applying a Hann window.

window is chosen, it is a simple cosine window given by the expression,

$$A(x) = 0.5\left[1 - \cos\left(\frac{2\pi x}{d}\right)\right] \tag{2.30}$$

where A is the amplitude of the window, x is the spatial position and d is the spatial length of the scan. The result of windowing is seen by comparing the amplitude spectrums in figure 2.3 (b) and (c), where (b) has its original rectangular window and (c) has been Hann windowed. The windowing increases the quality factor of the spectral component and thus the integration is reduced to only a few bins either side of the main lobe. The amplitude reduction caused by the application of a window can be accounted for by introducing a single multiplicative correction factor F_{c}. It can shown empirically that the correction factor for a Hann window is $F_{\mathrm{c}} = 1.633$. This value is independent of the phase or frequency of the signal to better than 1% [43]. To illustrate the advantage of this technique we shall analyse some real data where there is a large quantity of scattered light. The red line in figure 2.4 (a) shows a line scan of the electric field data along the axis of a 3μm waveguide it displays the characteristic modulation caused by scattered light. Figure 2.4 (b) and (c) are the FFT of the data shown in (a), (b) is without additional windowing and (c) is with. The scattered light component is clearly visible in both (b) and (c) by the slightly smaller peak at a lower frequency. The lobes in Hann windowing technique have a much higher roll-off, thus reducing the leakage between the scattered component and the frequency of interest. The values for the forward and backward propagating components have been acquired from the FFT shown in (c) and are used to plot the blue line shown in figure 2.4(a).

In practice 2D scans of the sample are acquired, permitting the frequency spectra of several line scans to be averaged to reduce the noise level. From the averaged FFT the DC and AC components are deduced. An example of this is shown in figure 2.5, where the area between the green lines define the sampled data. The integration bandwidth used to determine the amplitude of the AC component is limited to one bin either side of the

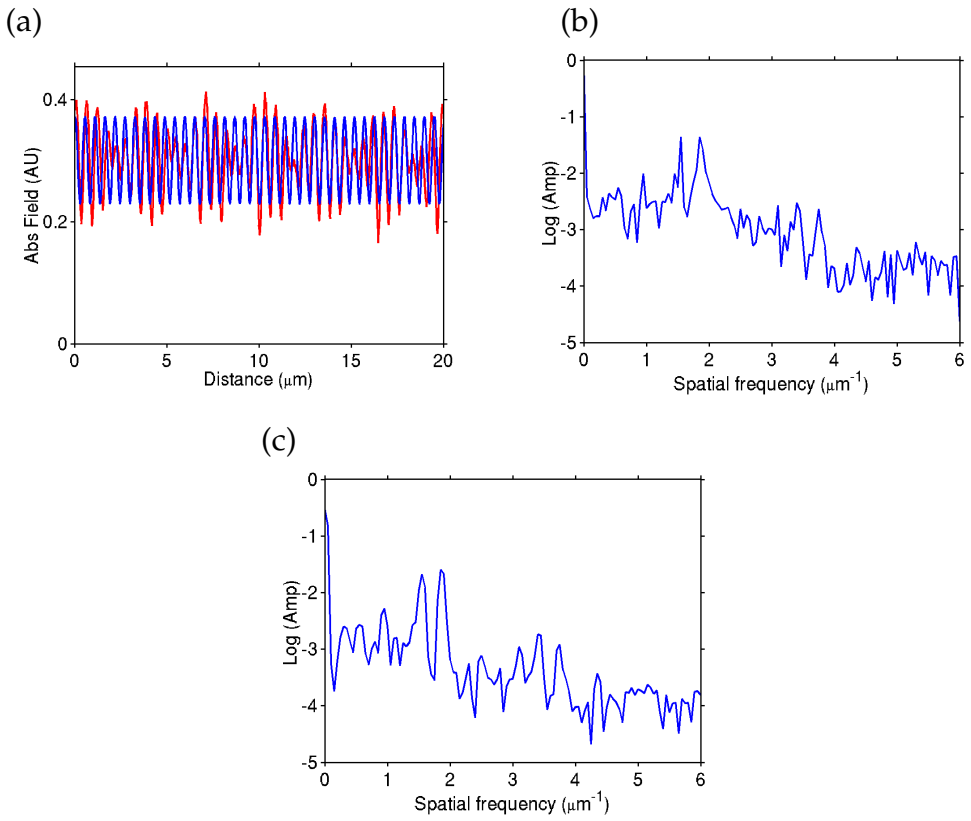

Figure 2.4: (a) The electric field magnitude as a function of distance along the axis of a waveguide, the red line represents real data. The blue line is a fit generated using the values derived from the FFT in (c). (b) and (c) are the amplitude spectra of (a) without and with Hann windowing respectively.

lobe. The calculated ratios from each of these lines scans typically yields a standard deviation of 2-3%.

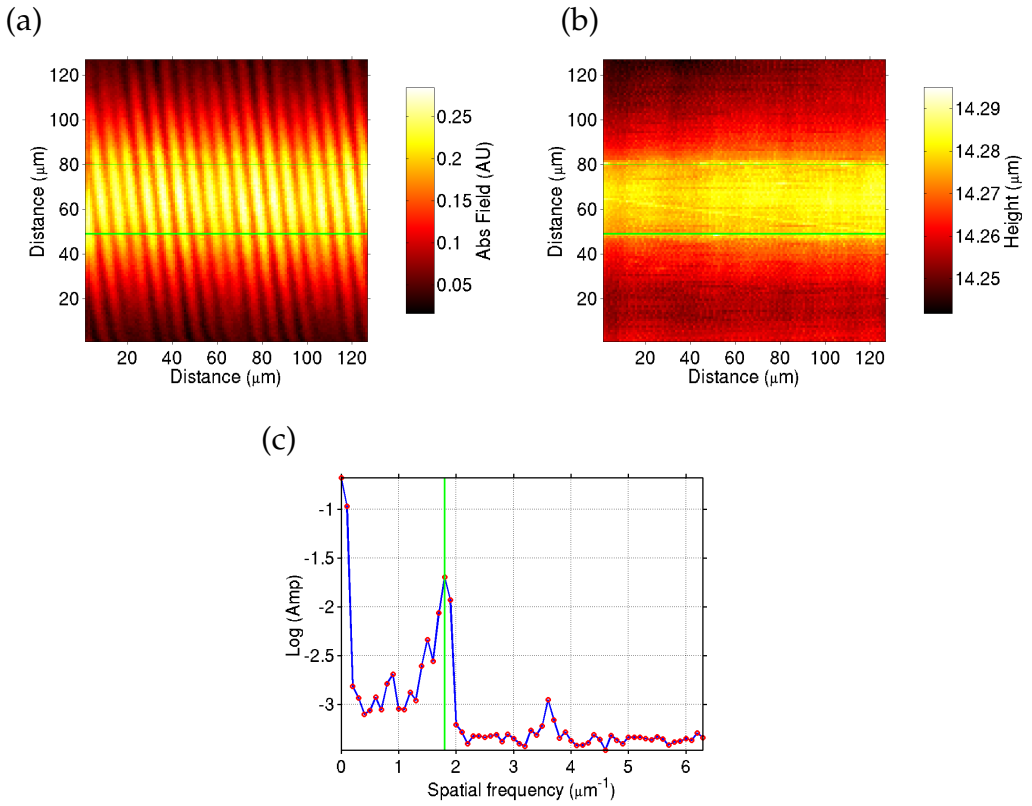

Figure 2.5: A 2D surface scan of the electric field above a 4μm waveguide. (a) Shows the electric field magnitude and (b) shows the topographical data. The green lines represent the boundaries of the selected line scans. (c) Is the average amplitude spectra of the lines scans specified in (a) and (b). From the amplitude spectra the value of A_b/A_f is equal to 0.191 ± 0.005.

2.4 Waveguide theory

The work presented in this thesis is all performed on different forms of waveguides. This section looks at the basic properties of waveguide modes. For the purposes of this analysis the most simplistic form of waveguide is considered, the symmetric slab waveguide. The treatment presented here

is derived from reference [44]. A schematic of the waveguide is shown in figure 2.6. The core and cladding refractive indices are denoted as n_{co} and n_{cl}, where $n_{\text{co}} > n_{\text{cl}}$. The guiding layer occupies the region $-d < x < d$,

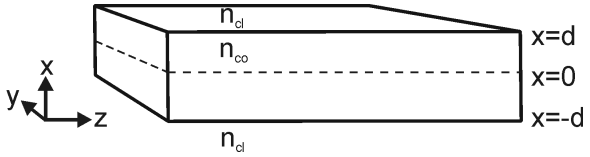

Figure 2.6: A symmetric slab waveguide.

and the field propagates in the z direction. The starting point for solving the waveguide modes is Maxwell's equations:

$$\begin{aligned} \nabla \times \mathbf{H} &= \mathbf{i} + \frac{\delta \mathbf{D}}{\delta t} \\ \nabla \times \mathbf{E} &= -\frac{\delta \mathbf{B}}{\delta t} \end{aligned} \tag{2.31}$$

where $\mathbf{E}$ and $\mathbf{H}$ are the electric and magnetic displacement field vectors, respectively; $\mathbf{D}$ and $\mathbf{B}$ are the electric and magnetic displacement vectors and $\mathbf{i}$ is the current density. All of these vectors are time varying functions. The time behavior can be assumed to take the form $\exp(i\omega t)$. As a result of the 2 dimensional geometry of the waveguide there is no variation in the y axis, therefore $\delta/\delta y = 0$. Applying these conditions to Maxwell's equations yields:

$$\begin{aligned} \tfrac{\delta E_y}{\delta z} &= i\omega\mu H_x \\ \tfrac{\delta E_x}{\delta z} - \tfrac{\delta E_z}{\delta x} &= -i\omega\mu H_y \\ \tfrac{\delta E_y}{\delta x} &= -i\omega\mu H_z \\ \tfrac{\delta H_y}{\delta z} &= -i\omega\varepsilon E_x \\ \tfrac{\delta H_x}{\delta z} - \tfrac{\delta H_z}{\delta x} &= i\omega\varepsilon E_y \\ \tfrac{\delta H_y}{\delta x} &= i\omega\varepsilon E_z \end{aligned} \tag{2.32}$$

Examination of the relations in 2.32 shows two self-consistent types of solutions. The solutions relate to the TE and TM modes of the waveguide, since the electric field (E_y) is restricted to the y and x plane respectively. The solutions for the TE and TM modes are very similar, and thus the TE case will be considered. The z dependence of the modes can also be assumed to take the form $\exp(-i\beta z)$ where β is the propagation constant,

thus $\delta/\delta z = -i\beta$. Thus Maxwell's equations condense to the two relations:

$$\begin{aligned} E_y &= -\frac{\omega\mu}{\beta}H_x \\ \frac{\delta E_y}{\delta x} &= -i\omega\mu H_z \end{aligned} \tag{2.33}$$

As the waveguide is symmetrical about the $x = 0$ plane, the solutions must be even or odd, such that for the even modes,

$$E_y(x, z, t) = E_y(-x, z, t) \tag{2.34}$$

and subsequently the odd modes:

$$E_y(x, z, t) = -E_y(-x, z, t) \tag{2.35}$$

The even solutions describe the symmetric modes and the odd solutions describe the asymmetric modes. In most of the work presented in this thesis the fundamental mode is exploited which is symmetric, therefore the solution for the even modes takes the form:

$$\begin{aligned} E_y &= A\exp[-p(|x| - d) - i\beta z] && |x| \geq d \\ E_y &= B\cos(hx)\exp(-i\beta z)] && |x| \leq d \\ H_z &= \pm\tfrac{ipA}{\omega\mu}\exp[-p(|x| - d) - i\beta z] && |x| \geq d \\ H_z &= -\tfrac{ihB}{\omega\mu}\sin(hx)\exp(-i\beta z)] && |x| \leq d \end{aligned} \tag{2.36}$$

Valid solutions must provide continuity at the boundaries ($|x| = \pm d$), and therefore

$$\begin{aligned} A &= B\cos(hd) \\ pA &= hB\sin(hd) \end{aligned} \tag{2.37}$$

The constants p and h can solved by applying the wave equation, for further details of the solution the reader is directed to the source [44]. The solutions of E in equation 2.36 present the form of the guided modes. In the core region ($|x| \leq d$) the mode has a sinusoidal profile in the x direction and propagates in the z axis defined by the propagation constant β. In the cladding region ($|x| \geq d$) the field again propagates in the z direction with the propagation constant β, however the fields exponentially

decay in the x direction. These same fields were described by the angular spectrum model and are called evanescent waves. It is important to note from the equations in 2.37 that the evanescent fields have an amplitude proportional to that of the propagating modes.

Two of the investigations presented in this thesis exploit the evanescent fields to gain information about the waveguide and the optical fields within. In chapter 5 a channel waveguide is investigated, the waveguide has an asymmetric index profile with air acting as the top cladding. The evanescent component of the mode exists at this interface, permitting the field to be collected with the near-field probe. In chapter 4 an optical fibre is investigated, the evanescent field is normally contained within the cladding of the fibre. To gain access to the evanescent field it is necessary to remove some of the cladding.

2.5 Fiber Bragg grating theory

Chapter 4 presents an investigation of the evanescent field distribution above a fibre Bragg grating. The fibre gratings analysed were fabricated to have a uniform periodic refractive index change along the optical axis of the fibre, this is known as a "uniform grating". This section introduces the theory behind uniform fibre Bragg gratings required to support some of the analysis presented in the corresponding chapter. For the work presented in this thesis a quantitative description of fibre gratings is not required and therefore a qualitative picture of the basic mechanisms is presented.

The grating is produced by exposing the fibre to a spatially varying pattern of ultraviolet light, the details of which are specified in section 4.1.1. The resulting index perturbation to the effective index n_{eff} of the optical modes is described by [45],

$$\delta n_{\text{eff}}(x) = \overline{\delta n}_{\text{eff}}(x)\left[1 + \upsilon \cos\left(\frac{2\pi}{\Lambda}x + \phi(x)\right)\right] \tag{2.38}$$

where $\overline{\delta n}_{\text{eff}}$ is the spatially averaged index change over a grating period, υ is the fringe visibility of the index modulation, Λ is the period of the grating and $\phi(x)$ defines the grating chirp. By definition there is no chirp in uniform gratings and therefore the $\phi(x)$ term can be neglected. This index modulation functions as a simple diffraction grating, the effect of which can be described by the familiar grating equation [46],

$$n \sin\theta_2 = n \sin\theta_1 + m\frac{\lambda}{\Lambda} \tag{2.39}$$

where θ_1 and θ_2 are the angles of the incident and diffracted waves respectively and m is the order of the diffracted wave. The equation predicts the angles of which constructive interference occurs, but it also capable of determining the wavelength at which the grating couples most efficiently between the two modes. The propagating constant of a mode is given by,

$$\beta = n_{\text{eff}} k = nk \sin\theta \tag{2.40}$$

where n_{eff} is the average effective refractive index of mode. Therefore equations 2.39 can be redefined in terms of β,

$$\beta_2 = \beta_1 + m\frac{2\pi}{\Lambda} \tag{2.41}$$

For the situation where the light is reflected into the original mode but with opposing direction, the condition $\beta_1 = \beta_2$ can be assumed. The most common configuration explored in this thesis is the first order diffraction (m = -1), this is also the strongest resonance of fibre gratings [45]. Applying these conditions to equation 2.41, yields the phase matching condition for the first order resonance of the grating,

$$\lambda_{\text{B}} = 2n_{\text{eff}}\Lambda \tag{2.42}$$

where λ_{B} is the Bragg wavelength. This simple model can also predict the wavelength of the cladding mode resonances which are encountered in chapter 4. The cladding modes have a effective index bound by the inequality $1 < n_{\text{eff}} < n_{\text{cl}}$. A more generalised version of the previous equation is,

$$\lambda_{\text{B}} = (n_{\text{eff},1} + n_{\text{eff},2})\Lambda \tag{2.43}$$

where $n_{\text{eff},1}$ and $n_{\text{eff},2}$ are the effective refractive indices of the coupled modes. As the effective index of the cladding modes is lower than that of that of the core mode, the cladding mode resonances exist at proportionally shorter wavelength than that of the core mode resonance.

This simple model however does not give any quantitative information such as the coupling strength or the spectral dependence. A good tool for obtaining these properties in fibre Bragg gratings is coupled mode theory, an excellent review of the applications of this technique is presented in reference [45].

2.6 Interpretation of the measured field

In order to analyse the SNOM data an appreciation of the mechanisms affecting the evanescent field is required. This section briefly discusses the origin of optical mechanisms responsible for the electric field distributions observed in chapters 4 and 5.

In chapters 4 and 5 the SNOM probe samples a cross section of the mode/s electric field propagating through the waveguide. The complex amplitude of the field at the surface of the sample is dependent on localised properties of the waveguide, such as the refractive index and the thickness of the cladding. An ideal uniform waveguide would therefore have an electric field amplitude which was constant along the optical axis. However imperfections in the fabrication of the waveguide can induce local changes in the refractive index and the thickness of the cladding. The detected electric field therefore becomes a function of these perturbations. The only effects due to the fluctuations in the thickness of the cladding was observed during the investigation shown in chapter 5. The fluctuations were in the form of surface defects, such features are normally classed as imaging artifacts as discussed in section 2.2.5.2. However the index contrast mechanism has implications for the investigation of fibre Bragg gratings presented in

chapter 4.

The periodic index modulation in the core of fibre Bragg gratings can produce an optical contrast in the evanescent field. The effect has been observed in a prior SNOM investigation of fibre Bragg gratings [47]. When the phase matching condition is satisfied (see section 2.5), a proportion of the mode is reflected and the resulting counter propagating fields interfere to generate a standing wave. The detected field is thus a function of both the standing wave and the refractive index modulation. However at wavelengths away from any grating resonance the electric field can be assumed to be uniform, and the detected field is dominated by the refractive index variation along the grating. In order to show the true electric field distribution and to decouple these effects it is necessary to measure the electric field distribution both on and off-resonance.

2.7 Chapter summary

This chapter has shown the necessity of collecting the evanescent components in order to break the resolution limit defined by the Rayleigh criterion. In order to define the features of evanescent fields the angular spectrum model was introduced. A large portion of the chapter describes the principles behind the SNOM technique including an outline of the heterodyne detection system. The remainder of the chapter introduces the background theory and techniques required for the analysis of the data presented in the following chapters.

2.8 References

[1] E Abbe. "Beitrage zur Theorie des Mikroskops und der mikroskopischen Wahrnehmung". *Archiv f. Miroskop. Anat.*, 9:413, 1873.

[2] J. W. Goodman. *Introduction to Fourier Optics*. McGraw-Hill, New York, 1968.

[3] D. Courjon, J. M. Vigoureux, M. Spajer, K. Sarayeddine, and S. Leblanc. "External and internal reflection near field microscopy:experiments and results". *Applied Optics*, 29(26):3734–3740, 1990.

[4] G. A. Valaskovic, M. Holton, and G. H. Morrison. "Parameter Control, Characterization, and Optimization in the Fabrication of Optical-Fiber near-Field Probes". *Applied Optics*, 34(7):1215–1228, 1995.

[5] S Madsen, N.C.R. Holme, P.S. Ramanujam, S Hvilsted, J.M. Hvam, and S.J. Smith. "Optimizing the fabrication of aluminium-coated fiber probes and their application to optical near-field lithography". *Ultramicroscopy*, 71:65–71, 1998.

[6] S. Kawata, Y. Inouye, and T. Sugiura. "Near-Field Scanning Optical Microscope with a Laser Trapped Probe". *Japanese Journal of Applied Physics Part 2-Letters*, 33(12A):L1725–L1727, 1994.

[7] H. M. Hertz, L. Malmqvist, L. Rosengren, and K. Ljungberg. "Optically Trapped Nonlinear Particles as Probes for Scanning near-Field Optical Microscopy". *Ultramicroscopy*, 57(2-3):309–312, 1995.

[8] E. Wolf and M. Nietovesperinas. "Analyticity of the Angular Spectrum Amplitude of Scattered Fields and Some of Its Consequences". *Journal of the Optical Society of America A-Optics Image Science and Vision*, 2(6):886–889, 1985.

[9] D.W. Pohl and D. Courjon. *Near Field Optics*, volume 242 of *Applied sciences*. Kluwer Academic Publishers, Dordrecht, 1993.

[10] D. Barchiesi and D. Vanlabeke. "Application of Mie Scattering of Evanescent Waves to Scanning Tunneling Optical Microscopy Theory". *Journal of Modern Optics*, 40(7):1239–1254, 1993.

[11] D. Christensen. "Analysis of near field tip patterns including object interaction using finite-difference time-domain calculations". *Ultramicroscopy*, 57:189–195, 1995.

[12] H. Furukawa and S. Kawata. "Analysis of image formation in a near-field scanning optical micrscope: effect of multiple scattering". *Optics Communications*, 132:170–178, 1996.

[13] D. Courjon. *Near-field microscopy and near-field optics*. Imperial College Press, 2003.

[14] H. A. Bethe. "Theory of Diffraction by Small Holes". *Phys. Rev.*, 66:163–182, 1944.

[15] C. J. Bouwkamp. "On the Diffraction of Electromagnetic Waves by Small Circular Disks and Holes". *Phillips Res. Rep.*, 5:401–442, 1950.

[16] D. Vanlabeke, D. Barchiesi, and F. Baida. "Optical Characterization of Nanosources Used in Scanning near- Field Optical Microscopy". *Journal of the Optical Society of America A-Optics Image Science and Vision*, 12(4):695–703, 1995.

[17] U. Durig, D. W. Pohl, and F. Rohner. "Near-Field Optical-Scanning Microscopy". *Journal of Applied Physics*, 59(10):3318–3327, 1986.

[18] A. Roberts. "Small-hole coupling of radiation into a near-field probe". *Journal of Applied Physics*, 70(8), 1991.

[19] A. Drezet, J. C. Woehl, and S. Huant. "Extension of Bethe's diffraction model to conical geometry: Application to near-field optics". *Europhysics Letters*, 54(6):736–740, 2001.

[20] D. Courjon and C. Bainier. "Near-Field Microscopy and near-Field Optics". *Reports on Progress in Physics*, 57(10):989–1028, 1994.

[21] R. C. Reddick, R. J. Warmack, and T. L. Ferrell. "New Form of Scanning Optical Microscopy". *Physical Review B*, 39(1):767–770, 1989.

[22] D. P. Tsai, H. E. Jackson, R. C. Reddick, S. H. Sharp, and R. J. Warmack. "Photon Scanning Tunneling Microscope Study of Optical Wave- Guides". *Applied Physics Letters*, 56(16):1515–1517, 1990.

[23] E. Betzig, P. L. Finn, and J. S. Weiner. "Combined Shear Force and near-Field Scanning Optical Microscopy". *Applied Physics Letters*, 60(20):2484–2486, 1992.

[24] R. L. Williamson, L. J. Brereton, M. Antognozzi, and M. J. Miles. "Are artefacts in scanning near-field optical microscopy related to the misuse of shear force?". *Ultramicroscopy*, 71(1-4):165–175, 1998.

[25] R. Toledocrow, P. C. Yang, Y. Chen, and M. Vaeziravani. "Near-Field Differential Scanning Optical Microscope with Atomic Force Regulation". *Applied Physics Letters*, 60(24):2957–2959, 1992.

[26] P.K. Wei and W.S. Fann. "Interactions between hydrophobic and hydrophilic silicon surfaces using a tapered probe in near-field scanning optical microscopy". *Journal of Microscopy*, 194:445–447, 1999.

[27] M.J. Gregor, P.G. Blome, J. Schofer, and R.G. Ulbrich. "Probe-Surface interaction in near-field optical microscopy: The nonlinear bending force mechanism". *Applied Physics Letters*, 68(3):307–309, 1996.

[28] II Smolyaninov, W. A. Atia, S. Pilevar, and C. C. Davis. "Experimental study of probe-surface interaction in near-field optical microscopy". *Ultramicroscopy*, 71(1-4):177–182, 1998.

[29] D A Lapshin, E.E. Kobylkin, and V.S. Letokhov. "Shear force distance control in near field optical microscopy: experimental evidence of the frictional probe-sample interaction". *Ultramicroscopy*, 83:17–23, 2000.

[30] G. T. Shubeita, S. K. Sekatskii, B. Riedo, G. Dietler, and U. Durig. "Scanning near-field optical microscopy based on the heterodyne phase-controlled oscillator method". *Journal of Applied Physics*, 88(5):2921–2927, 2000.

[31] R. Brunner, O. Marti, and O. Hollricher. "Influence of environmental conditions on shear-force distance control in near-field optical microscopy". *Journal of Applied Physics*, 86(12):7100–7106, 1999.

[32] J. U. Schmidt, H. Bergander, and L. M. Eng. "Experimental and theoretical analysis of shear-force interaction in the non-contact regime with 100 pN force resolution". *Applied Surface Science*, 157(4):295–301, 2000.

[33] A. D. Muller and F. Muller. "Resonance frequency shifts caused by the friction of a drop of water in air: An approach to estimate shear forces in scanning probe microscopies". *Applied Physics Letters*, 78(14):2079–2081, 2001.

[34] D. A. Lapshin, V. S. Letokhov, G. T. Shubeita, S. K. Sekatskii, and G. Dietler. "Direct measurement of the absolute value of the interaction force between the fiber probe and the sample in a scanning near-field optical microscope". *Applied Physics Letters*, 81(8):1503–1505, 2002.

[35] C. L. Jahncke and H. D. Hallen. "Stabilizing wide bandwidth, tuning fork detected force feedback with nonlinear interactions". *Journal of Applied Physics*, 93(2):1274–1282, 2003.

[36] A.G.T. Ruiter, K.O. van der Werf, J.A. Veerman, M. GarciaParajo, and N. van Hulst. "Tuning fork shear-force feedback". *Ultramicroscopy*, 71:149–157, 1998.

[37] A Yariv. "Optical Electronics". pages 352–363. CBS College Publishing, New York, third edition, 1985.

[38] B.E.A Saleh and M.C Teich. "Fundamentals of Photonics". pages 907 –911. J. Wiley and Sons, New York, 1991.

[39] B. Hecht, H. Bielefeldt, Y. Inouye, and D. W. Pohl. "Facts and artifacts in near-field optical microscopy". *Journal of Applied Physics*, 81(6):2492–2498, 1997.

[40] S. I. Park, J. Nogami, and C. F. Quate. "Effect of Tip Morphology on Images Obtained by Scanning Tunneling Microscopy". *Physical Review B*, 36(5):2863–2866, 1987.

[41] S. I. Bozhevolnyi, B. Vohnsen, and E. A. Bozhevolnaya. "Transfer functions in collection scanning near-field optical microscopy". *Optics Communications*, 172(1-6):171–179, 1999.

[42] Robert.W Ramirez. In *The FFT fundamentals and concepts*, pages 137–143. Prentice-Hall, N.J., 1985.

[43] T.C. Ferree. "Inferring signal amplitudes from discrete (FFT) power values". Technical report, Electrical Geodesics, Inc., 5 Oct 2000.

[44] A Yariv. "Optical Electronics". pages 402–409. CBS College Publishing, New York, third edition, 1985.

[45] T. Erdogan. "Fiber grating spectra". *Journal of Lightwave Technology*, 15(8):1277–1294, 1997.

[46] M Born and E. Wolf. "Principles of Optics. Fourth Edition". In *Principles of Optics*, page 449. Pergamon Press, Oxford, 1970.

[47] J.D. Mills, C. W. J. Hillman, W. S. Brocklesby, and B.H. Blott. "Evanescent field imaging of an optical fibre Bragg grating". *Applied Physics Letters*, 75(26):4058–4060, 1999.

Chapter 3

Construction and analysis of the SNOM system

3.1 Chapter introduction

This chapter describes the realisation and the characterisation of the SNOM system used in the succeeding chapters. The chapter begins by briefly reviewing the SNOM system and dividing it into its relevant subsystems. Each subsystem is then individually addressed and analysed. The chapter concludes with a brief summary and possible future developments of the apparatus.

The previous chapter has described the three physical requirements for successful near-field imaging, each of these requirements can be considered as a subsystem of the SNOM apparatus. Without exception, the most important component is the near-field probe which samples the electric field, be it propagating or non-propagating. The fabrication and characterisation of the probes are discussed in section 3.1.1. The second subsystem is the ability to locate the surface of the sample to enable height regulation of the probe at a constant height above the sample. The height regulation system will be described in section 3.1.2. Section 3.1.3 describes the third

relatively trivial function of the nanometer control of the position of the probe. This outlines the basics of the SNOM system, however the work presented in this thesis also employs a heterodyne detection system, its construction is shown in section 3.1.4.

Figure 3.1 shows the schematic setup of the SNOM apparatus. Each subsystem has been highlighted in red.

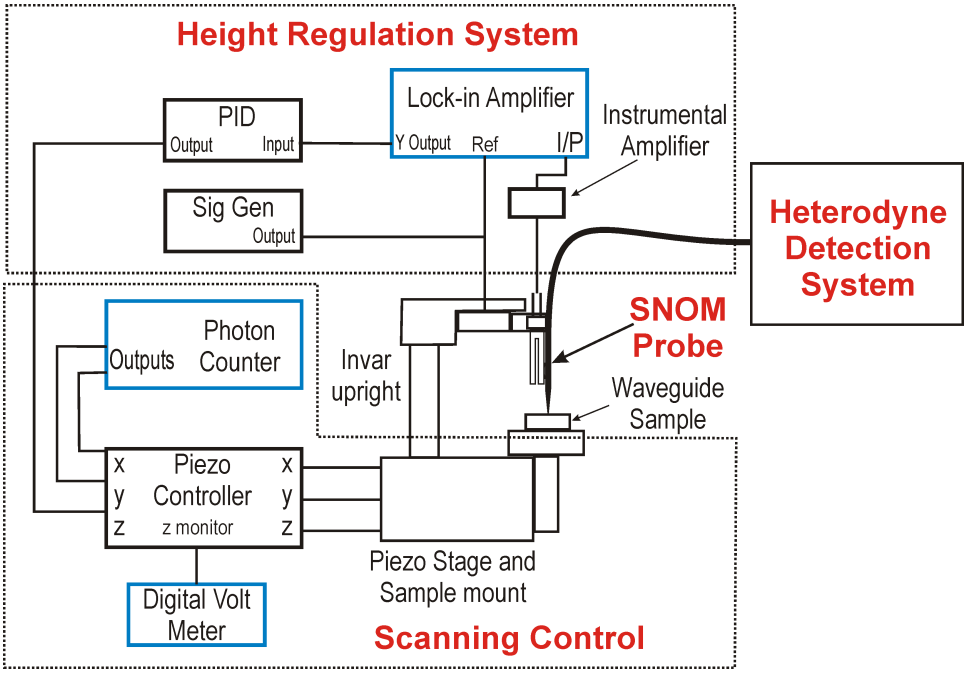

Figure 3.1: Schematic of the SNOM apparatus used to collect the data presented in this thesis. Each of the subsystems are highlighted in red and the components which are controlled via a GPIB interface are shown in blue. Connection details will be addressed within the relative subsystems. The optical signal coupled into the sample is not shown and will be presented in the heterodyne detection section 3.1.4. The PID is an abbreviation for Proportion, Integral and Differential controller.

3.1.1 Near-field probe fabrication and characterisation

In this thesis tapered fibers are exclusively used as the near-field probes. This type of probe has as several functions, it provides the small aperture

required for sub-wavelength resolution. It also acts as a sharp probe necessary to collect the topographical information of the surface. Its secondary function is to transmit the electric field collected by the aperture to the remote detection system.

There are two dominating techniques used to fabricate this type of probe, chemical etching [1] and the hot stretching technique [2]. Each method has advantages and drawbacks, however in these investigations the stretching technique has been exploited for its ease of application in standard laboratory environment. Two forms of these probes have been used in this thesis, coated and un-coated, their collection mechanisms have been previously highlighted in section 2.2.3.1. This section presents the fabrication and characterisation of these probes.

3.1.1.1 Fabrication of un-coated probes

The first step in the fabrication of both coated and un-coated probes is the drawing or pulling of the tip. The process involves the laser-heated pulling of an optical fibre. It is a complex process governed by a number of parameters. Extensive research has been applied to the optimisation of these parameters [3]. A commercial Sutter-P2000 pipette puller modified to pull optical fibres was used to fabricate the bare probes. The shape and dimensions of the probes were controlled by five basic parameters which were externally programmed into unit. A summary of the parameters is shown in table 3.1. The fibre used to fabricate the probes was standard telecoms fibre made by 3M with a single mode cutoff at $\approx$ 1230nm. The cladding and core diameter was 125 μm and 9μm respectively. The Sutter puller was switched on approximately 1 hour prior to fabricating the probes to allowing the CO_2 heating laser to thermally stabilise. The fibre was initially prepared by mechanically stripping a $\approx$30mm section of the fibre approximately 15cm from one end of the fibre. The stripped section was then cleaned using a lens tissue wetted with methanol. The fibre was

then mounted on the fibre carriage of the Sutter puller and the gripped in place with the fibre clamps. A successful pull would only be achieved with a good alignment of the fibre. On initiation of the program the stripped section of the fibre is heated with the 10W CO_2 laser and sensors measure the displacement of the carriages. The relative power of the laser is defined by the "heat" parameter. At a specific carriage velocity, predefined by the "velocity" parameter the CO_2 laser is turned off. After a delay determined by the "delay" parameter the fibre is pulled by a solenoid actuator. The force applied to the fibre is determined by the "pull" parameter. The time for which the laser is active is fed back to the operator as a indication of the success of the pulling process. Empirically it was found that a value of 0.16 ± 0.01 seconds indicates success. Further details of the micropipette puller operation can be found elsewhere [4]. Visual inspection via an optical microscope is performed on the tip with the shorter length of fibre. This allows the other identical probe to be used directly in the SNOM or coated with aluminium. Figure 3.2 shows two optical microscope images of a tip suitable for use as a probe.

Characterisation with the optical microscope provides a quick method of checking the quality of the taper. However to check the nanoscale dimensions of the apex of the probe, a scanning electron microscope (SEM) inspection is required. Figure 3.3 shows a SEM image of the apex of a typical fibre probe, the "laser on" time was 0.17 seconds. SEM images have

Parameter Name	Quantity used
Heat	300
Filament	0
Velocity	20
Delay	126
Pull	150

Table 3.1: The parameters of the Sutter-P2000 pipette puller used to fabricate the bare fibre probes. The quantities are all arbitrary units.

(a)

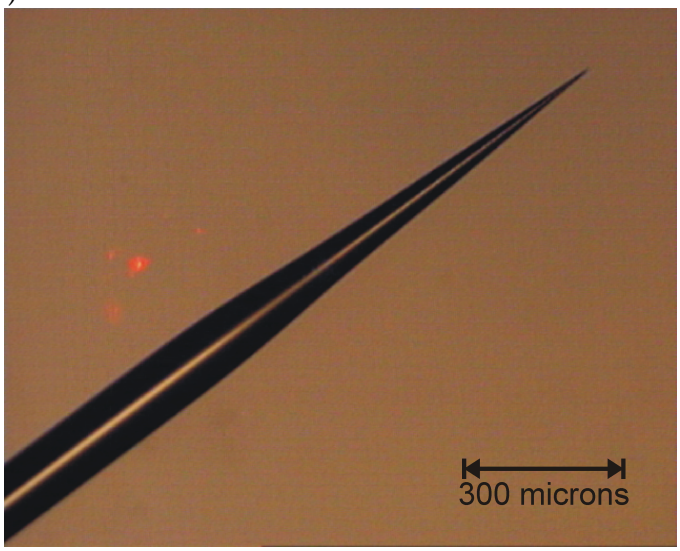

(b)

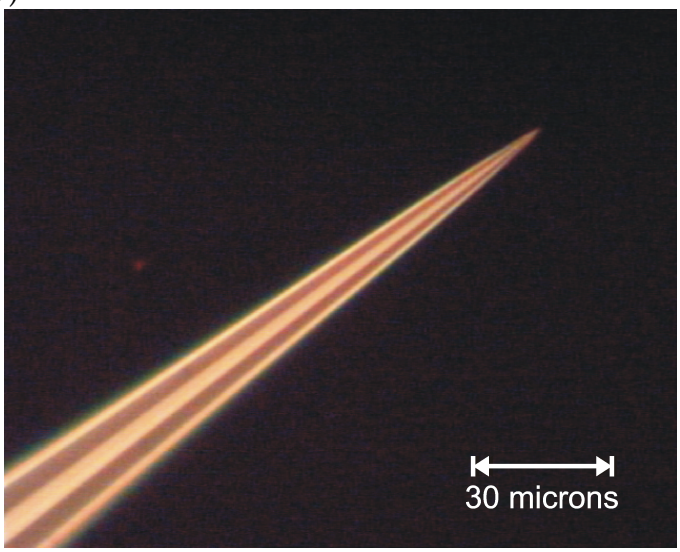

Figure 3.2: Far-field optical microscope images of a near-field probe, the "laser on" time was 0.18 seconds. [5].

confirmed that the fabrication technique can reproducibly generate probes with apex diameters of 60 nm. This form of probe is used image the electric field distributions within fibre Bragg gratings shown in chapter 4. The following section describes the technique used to produce aluminum coated fibre probes.

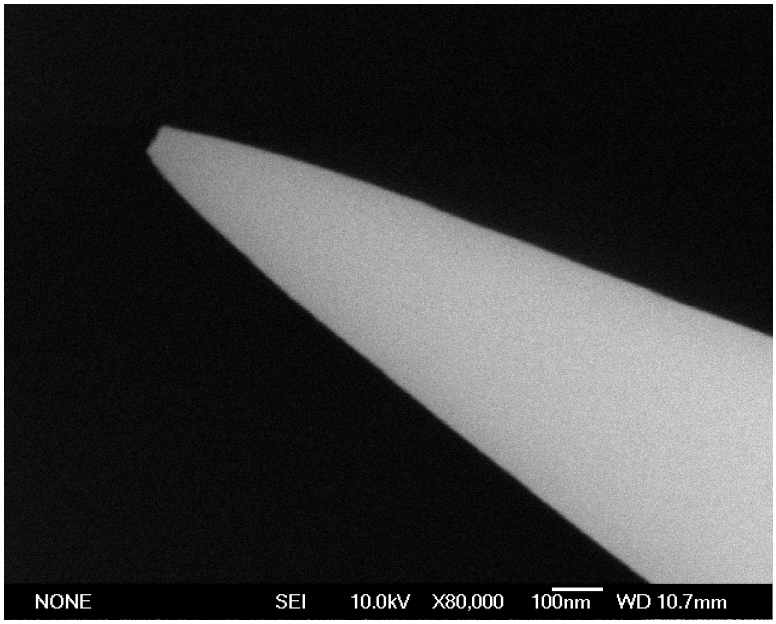

Figure 3.3: An SEM image showing the apex of a fibre probe. The apex diameter is ≈60nm [5].

3.1.1.2 Fabrication of coated probes

For many applications it is necessary to prevent propagating light from coupling into the probe via the side walls of the tip, reducing the resolution. This is achieved by preferentially coating the probes to leave a sub-wavelength aperture. The technique used in this thesis is that of the oblique evaporation technique, which exploits the sharp features of the tip apex to act as a mask. Figure 3.4 depicts the basic principle. The experimental process has been arduously characterised [6,3]. The probes are mounted on a rotating stage and placed in an vacuum chamber, which is promptly evacuated. The process is completed within minutes of the fibre

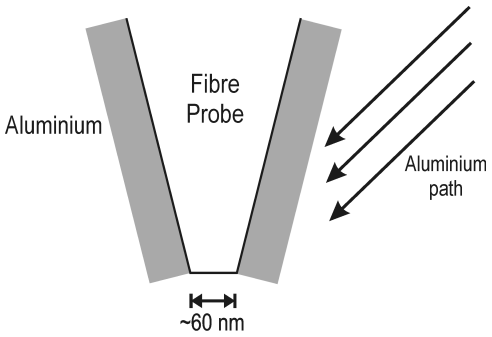

Figure 3.4: The basic principle of oblique evaporation.

being drawn, preserving the cleanliness of the probe. Coating was not performed before the chamber achieves a vacuum of $\approx 5 \times 10^{-5}$ Torr thereby reducing the oxidation and the formation of pin holes in the aluminium layer [6]. The low vacuum is also required to maximise the mean free path of the evaporated aluminium. Evaporation of the aluminium was achieved by the electrical heating of a multicore tungsten helicoil filament. The helicoil filament provides a high atomic flux with minimal heat [7]. A schematic of the oblique evaporation equipment is shown in figure 3.5. During evaporation the probe is rotated around its central axis at approx-

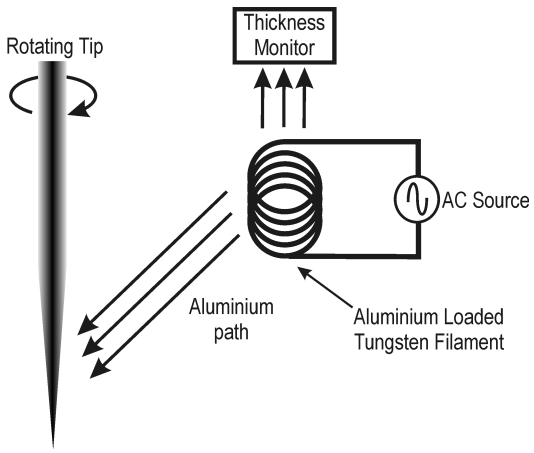

Figure 3.5: A schematic if the evaporation equipment.

imately 2 Hz. The thickness of the deposited aluminium was observed using a Polaron film thickness monitor. A glass slide placed in close proximity with the fibre probe enables the quality of the aluminum film to be

checked after the deposition. The thickness and quality of the aluminium on the test sample may be measured using an atomic force microscope (AFM) and may be used to calibrate the thickness monitor. It is necessary that the thickness of the aluminium is sufficient to prevent light coupling through the side walls of the probe. This is especially important for the work on holey fibres in chapter 6. For this it was necessary to achieved an attenuation of $\approx 10^{-6}$, corresponding to 14 skin depths of aluminium. At 1550nm the skin depth of aluminium is 8nm, thus a layer approximately ≈ 110 nm thick is required. However for the work in chapter 5 it was only necessary to coat the probe with 7 skin depths of aluminum, as the collected light is predominately evanescent. Over aluminisation causes a reduction in the topographical resolution, however for the work presented in this thesis this is not a concern due to the flat nature of the samples.

Characterisation of the coated probes is again achieved via a SEM. It gives direct information about the quality of the aluminium coating and size of the aperture at the tip. A SEM image of the side of a tip can be seen in figure 3.6(a) it shows the apex of the tip to have a diameter of ≈ 180nm. The figure also shows the collection of dust particles as the result of being left in a sealed container for a day between fabrication and imaging. Figure 3.6(b) shows an axial view of a different probe, and shows an aperture of approximately 100nm. Again dust can be seen on the walls of the probe, but is significantly reduced due to the probe being fabricated only two hours prior to imaging.

3.1.2 Height regulation

The height regulation method is based on a system developed by Karrai *et al.* [8]. The method uses the mechanical resonance of the probe to detect damping forces produced by the interaction with the surface. The change in the mechanical resonance is used as feedback to a piezo stage, to maintain a constant height above the surface. This section describes the method

(a)

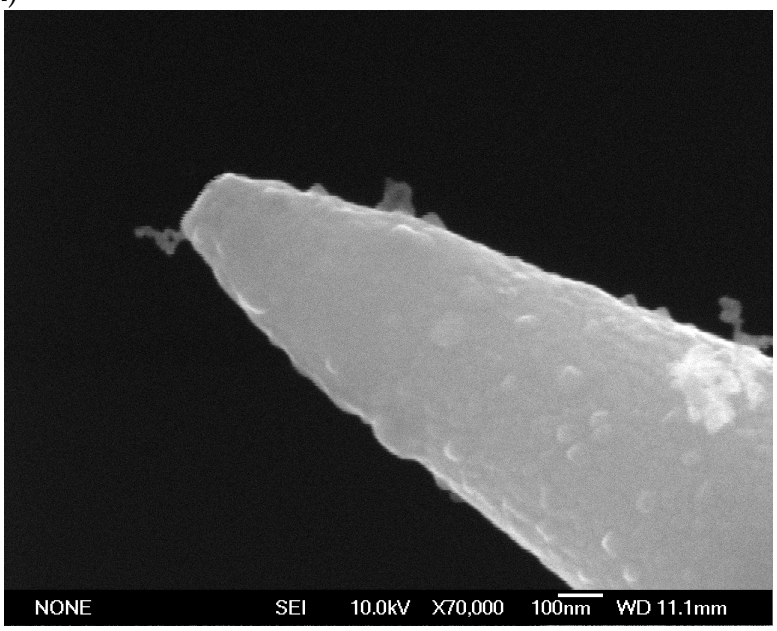

(b)

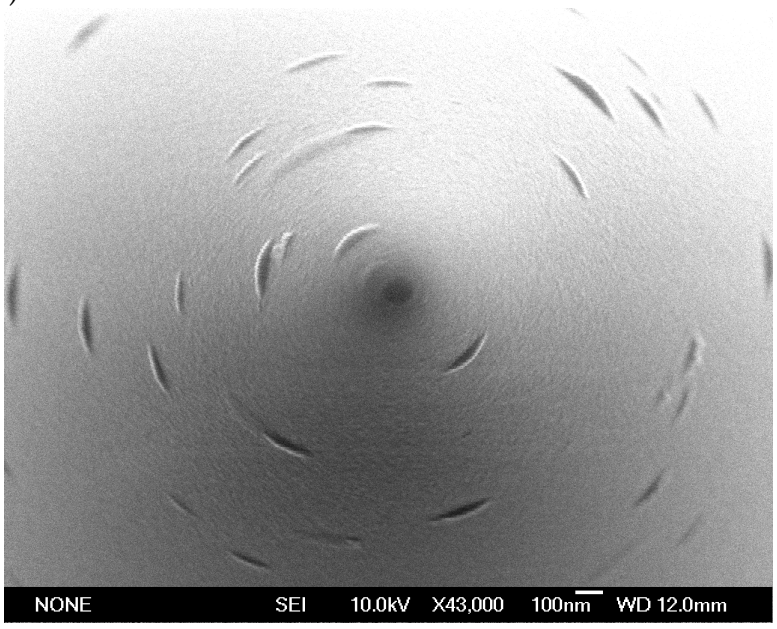

Figure 3.6: SEM images of coated near-field probes. (a) shows a side view of a tip with an apex size of approximately ≈180nm. (b) presents an axial view of the probe, showing a ≈100nm aperture at the apex [5].

in which this done.

The first prerequisite of the system is the method of dithering the tip and detecting the amplitude of the oscillation. In order to detect the small interaction forces with the surface, a relatively high quality (Q) factor is required to achieve the necessary sensitivity. The system proposed by Karrai *et al.* exploits the mechanical resonance of a piezoelectric tuning fork, frequently used as the timing crystals in watches. The system uses a separate piezo-electric disk to excite the tuning fork. The amplitude of the oscillation of the tuning can then be monitored via the induced voltage from the piezo elements built into the tuning fork. The magnitude of signal is proportional to the amplitude of the oscillation. A diagram of the arrangement is shown in figure 3.7. A sinusoidal voltage of approximately

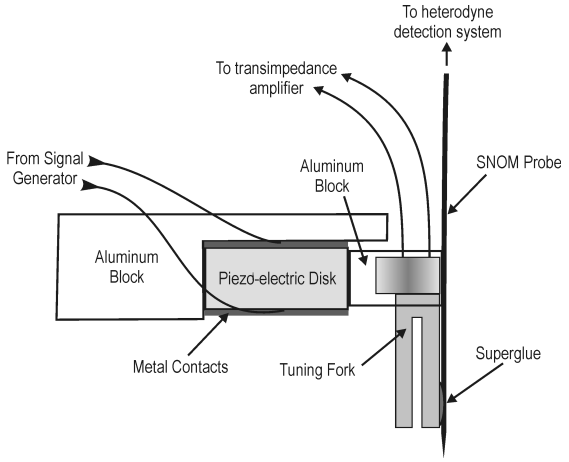

Figure 3.7: A diagram of the probe oscillation and detection system.

$50\mathrm{mV_{p-p}}$ is applied to the piezo-electric disk using a signal generator, the frequency of which is tuned to the resonant frequency of the tuning fork (≈ 32.768 kHz). The voltage produced by the tuning fork is amplified by a local instrumental amplifier and then measured using a Stanford SR530 dual channel lock-in amplifier (LIA). This arrangement forms the basis of the detection system. The tip is carefully mounted on the side of the tuning fork using cyanoacrylate adhesive (super glue). Super glue is favored for its quick drying time, easy removal and rigid mechanical bond. However even with its fast curing time, changes in the resonance of the tuning

fork are observed for several hours after gluing. It is therefore beneficial to keep the amount of glue to a minimum. Figure 3.8 shows a typical resonance curve of a tuning fork with a fibre attached. The resonant frequency

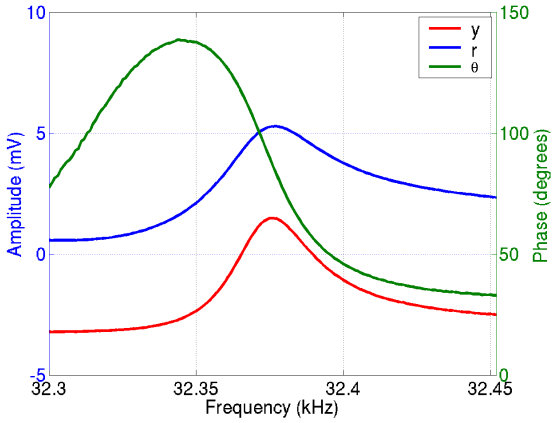

Figure 3.8: The resonance curve of a tuning fork with a tip attached. The three curves are the R, θ and Y ($\mathrm{R}\cos\theta$) outputs of the lock-in [5].

and the Q factor changes significantly during the mounting and attachment of the fibre probe. The resultant Q factor of the system was in the range of 500 to 1000, providing sufficient signal and sensitivity for monitoring the tuning fork oscillation. The Q factor of the system also defines the time response of the feedback and thus a compromise must be made between sensitivity and the time response of the system.

As the probe is brought into proximity with the surface, interactions between the surface and probe occur. The origins of these shear forces was discussed in section 2.2.3.5. The interaction with the surface perturbs the oscillation of the probe and therefore changes the amplitude and phase of the signal. The relationship between probe-sample separation and the Y ($\mathrm{R}\cos\theta$) output of the lock-in amplifier is shown in figure 3.9. The data shows the typical interaction length for this arrangement of ≈10nm. The position of the surface is difficult to define from the data, therefore the probe height scale is relative and thus the zero position is arbitrary. The Y output of the lock-in was chosen in preference to the R output to monitor the perturbation of the probe oscillation. The approximation was made

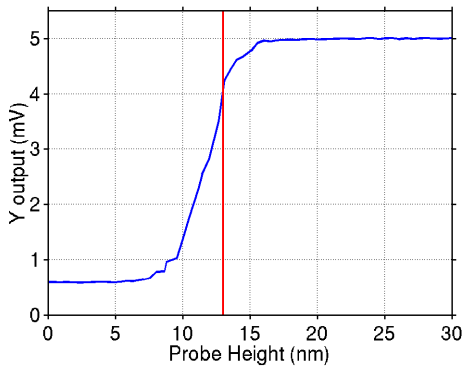

Figure 3.9: Plot showing the magnitude of the Y output of the lock-in as a function of the probe/sample separation. The sample was a plain glass slide.

due to the digital method in which the R output was calculated within the lock-in. The digitisation was found to produced additional noise in the feedback system. As the samples investigated here have consistent topography or are scanned in constant height mode the phase of the lock-in output remains constant and thus Y $\propto$ R.

As shown by figure 3.9 the Y output is a simple function of the probe - sample separation. It is therefore possible to implement a feedback system that uses the deviation of the Y output from a set point to control the probe height. The first stage of the system is to produce an offset in the Y output value, this defines the value of Y at which the feedback system regulates. The value chosen for this system is ≈75% of the undamped signal and is indicated by a vertical line in figure 3.9. The value also defines the magnitude of the probe/sample separation. The Y output of the lock-in is now called the error signal and is proportional to the deviation of Y from the set point.

The next stage of the feedback is the PID controller, it produces a signal that alters the height of the probe. The magnitude and direction is determined by the transfer function $G(e)$ which is a function of the error signal, e. The transfer function is defined by three components shown in equation

3.1:

$$G(e) = c_p e + c_p c_i \int e dt + c_p c_d \frac{de}{dt} \tag{3.1}$$

The three components of the equation are termed proportional (P), integral (I) and differential (D) respectively. The optimum values of the constants c_p, c_i and c_d are determined by experimentation with the specific probe and sample. The PID system was in-house built, the specifications and design can be found elsewhere [9]. The proportional component of the PID is a pure gain adjustment and provides the initial compensation for the changes in the error signal. The integral component is used to compensate for low frequency changes in the error signal. This is extremely useful for slow thermal fluctuations, and compensates for drift. The differential component increases the damping in the system and compensates for rapid fluctuations. However the derivative term also amplifies the existing noise which can cause problems including instability. As a result the differential component is rarely used. The next section illustrates the method used to scan the tip across the surface.

3.1.3 Scan control

In order to collect an image of the electric field and the topography, the probe must be moved about the surface to address each spatial position. This is achieved by employing a 3-axis piezo-electric flexure stage. Two different stages were used during the investigations presented in this thesis, both having similar piezo control with a maximum range of 20 μm. Both stages were specified as having 5nm resolution [10]. For the work presented in chapter 5 a Melles Griot Nanomax-HS 3 axis flexure stage was used. This stage had additional stepper motor control allowing up to 4.5 mm coarse adjustment with 25 nm resolution [10]. The remaining work present in this thesis was completed using a Melles Griot Nanoblock 3 axis flexure stage with manual coarse adjustment. The general operation of the stages was similar, however the characteristics of the piezo response dif-

fered and will be addressed in section 3.2.4. Both stages use internal strain gauges for position feedback to reduce hysteresis effects, common in piezo actuators. Spatial calibration of the stages was performed by optical interferometry or with a sample of know period, such as a phase mask. The x and y channels define the location in the plane of the sample. In chapters 4 and 5 the y axis is chosen to be collinear to the optical axis of the waveguides. The position is controlled by the computer via the analogue outputs of the photon counter (see figure 3.1). The z channel of the stage defines the probe/sample separation and was controlled by the output of the PID feedback system or with an analogue output of the SR830 LIA.

3.1.4 The optical heterodyne detection system

This section looks at the heterodyne detection system used to analyse the optical signal collected by the SNOM probe. As previously shown in section 2.2.4, the heterodyne system permits the measurement of the complex electric field. This section describes the physical arrangement of the system, and is based on a system original suggested by Balistreri *et al.* [11]. A schematic of the heterodyne detection system can be seen in figure 3.10. The system uses two optical sources, a 5mW 633nm polarised HeNe laser and an Agilent 81600B tunable diode laser with a wavelength range of 1500 to 1640nm. The diode laser was fully automated via GPIB interface, allowing the wavelength and power to be externally controlled. The HeNe laser was used to assist in the butt coupling of the fibre to the sample and in locating the waveguide with the SNOM probe. The sources are coupled into the system using a 50:50 4 port fibre coupler. All the fibre couplers used in this arrangement were fabricated by JDS Uniphase and specified for use in the C-band (1520-1570nm) wavelength region. One of the outputs of the coupler provides the signal for the device under investigation, the polarisation of which is controlled by a fibre polarisation rotator. The other output is collimated using a $\times$20 AR coated objective. The free space beam was then frequency shifted by two similar acoustic opti-

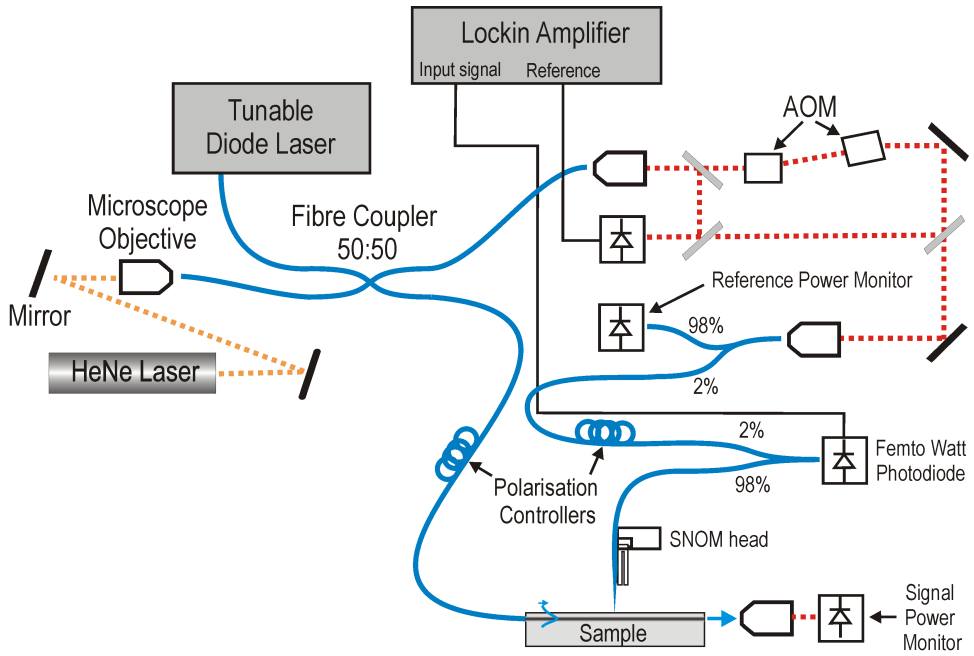

Figure 3.10: A schematic of the optical heterodyne detection system. Blue lines represent optical fibre, the orange and red lines correspond to free space beams at 633mm and ≈1550nm respectively.

cal modulators (AOMs) (Gooch and Housego, model No.M080-1F-GH2). The modulators were aligned with opposing diffraction orders to produce a frequency shift equal to the difference between the drive signals of the AOMs. The frequency of one of the drivers was adjusted to provide a frequency difference of ≈600 Hz.

A small proportion of beam before and after the frequency shift is combined collinearly on to a photodiode, the amplified photocurrent is used as a reference input to a dual channel lock-in amplifier (Stanford Research Systems SR830). The remaining frequency shifted beam is used at the optical reference beam and is coupled back into a fibre via a ×10 AR coated objective. A three port fibre coupler allows 98% of the power to be used as a reference monitor. While the remaining 2% is coupled into a 2% port of another 98:2 fibre coupler, where it recombines with the signal detected by the SNOM probe. The polarisation of the reference beam is controlled by another fibre polarisation rotator. The ratios of the fibre couplers are cho-

sen to maximise the signal acquired. The combined beams are detected by a femtowatt photodetector (NewFocus 2153IR) to generate a beat signal at the AOM frequency difference. The signal from the detector is then measured using the lock-in amplifier. The X and Y outputs of the lock-in are acquired directly from the lock-in via GPIB. The lengths of the arms of the interferometer are kept as short as possible (≈3.5 meters) to reduce thermal related phase drift. The two arms are also kept to similar lengths reducing the effects of fluctuations in the optical frequency. The optical output of the sample is monitored using the optical power meter integral to Agilent laser system, this provided a calibrated reading of the optical power. More details about optical fibre heterodyne interferometers can be found elsewhere [12].

The system is completely controlled by a Unix PC via a GPIB interface. The acquisition software was in the form of Tcl and Tk scripts which were executed via a VNC (virtual network computing) connection. This allowed the equipment to be controlled externally from any networked terminal. Post analysis of the data was performed using Matlab.

3.2 Optimisation and characterisation of the SNOM

This section discusses additional optimisation of the system required to reduce noise in the system and therefore produce reliable data. It also looks at aberrations caused by the piezo scanning system. The chapter starts by looking at the environmental isolation of the apparatus.

3.2.1 Environmental isolation

The origin for most of the noise seen in SPM techniques is the effect the environment has on the probe. In the present SNOM system there are three sources: mechanical vibration propagating through the bench and cables

etc., acoustic vibrations from the surrounding air and, thermal fluctuations of the lab. The feedback system of the SNOM apparatus compensates for much of these effects, however the same external sources equally effect the stability of the heterodyne interferometer. As a heterodyne system has no active feedback, additional isolation was required.

Mechanical vibrations were reduced by floating the table on partially inflated pneumatic tyre inner tubes, this sufficiently dampened most building vibrations. All electrical equipment was kept off the optical bench to reduce line frequency noise. Cables between the table and electrical equipment were kept to a minimum. General thermal fluctuations were reduced by surrounding the SNOM and interferometer in thermally insulating boxes. The insulation also served to noticeability reduce the acoustic noise. The thermal effects in the SNOM system was also reduced by fabricating much of the scanning system from Invar, known for its low thermal expansion. The largest cause of phase drift in the interferometer is thermally induced refractive index change in the fibres. Consequently, in addition to insulating boxes the optical fibres were surrounded in plastic sleeving and held close to the optical bench. Figure 3.11 illustrates the stability of the phase by presenting consecutive line scans at the same location. It shows a thermal change in the phase of 60 degrees over the duration of the scan, corresponding to change of 210 deg/hour. The typical length of time for a scan is $\approx$ 10 to 17 minutes depending on the spatial size number of points, equating to a phase drift of $\approx$ 35 to 60 degrees. The topographical data was used to confirm the repeatability of the location. To reduce air currents the room was isolated by sealing off any possible sources of drafts. In addition the room was not entered during scanning. Figure 3.12 shows the thermal stability of the room over a 24 hour period. The data commences at 17:00 hours and shows the equipment stabilising after the thermocouple was installed. The purpose of the insulation was not to maintain a constant operating temperature, but to reduce the speed of the temperature fluctuations to a time constant longer than the duration

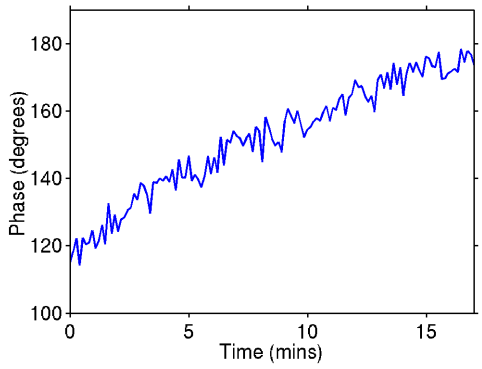

Figure 3.11: Graph demonstrating the change of the phase above a waveguide as a function of time.

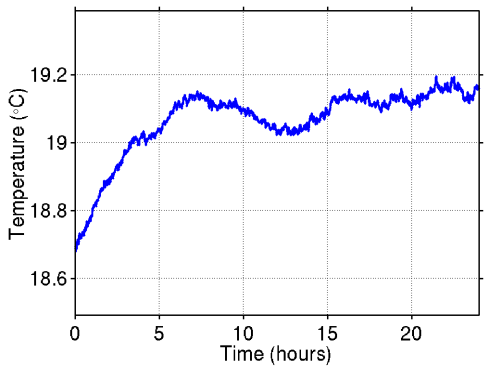

Figure 3.12: Graph showing the temperature of thermally isolated apparatus.

of a scan.

3.2.2 Data repeatability

The repeatability of the data can be tested by showing consecutive scans of the same region. Figure 3.13 shows two consecutive scans of the topography of a fibre Bragg grating (see chapter 4) taken 3 hours apart. The data shows a thermal drift of 174nm in the z axis and 90nm in the xy plane over the 3 hour period. Surface features can be used to determine the drift. This magnitude of drift was typical for this system. Several scans in the same position were also taken in the intervening period, the repeatability of the surface features confirm that significant tip damage did not occur.

(a) (b)

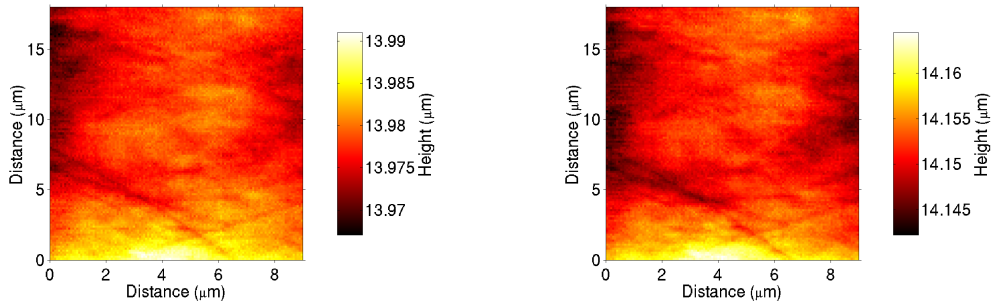

Figure 3.13: (a) and (b) show false colour images of the plane removed topography of a fibre Bragg grating. The scans were taken at the same position 3 hours apart.

3.2.3 Resolution

The topographical resolution of the system is defined by the size and shape of the probe. The characterisation of the near-field probes in section 3.1.1, confirmed that the apex of the un-coated probes are $\approx$ 60nm. Coating the probes reduces the spatial resolution; the extent is dependent on the

amount of aluminum. The samples investigated throughout this project have large feature sizes and thus the topographical resolution of the probes was not a limiting factor.

The optical resolution of the system is again defined by the probe dimensions. For un-coated and coated probes the optical resolution is determined by the size of the apex and aperture of the probe respectively, the size of which have been confirmed by SEM measurement. Experimentally confirmation the optical resolution can be achieved by imaging a topographically free sample with optical contrast. However the fabrication of such a sample is not trivial, the details of such a method is given in reference [13]. Another potential method suggested by [14] is the use of counter propagating evanescent fields. The aperture size is determined by comparing the measured visibility of the standing wave to that of the visibility predicted from the known amplitudes of the two fields. However it has been correctly remarked [15] that this only gives a indication of the symmetry of the probes. The work in chapter 5 images such a system, and was shown to produce values for the visibility approximating that expected, indicating the probes have a high quality. However the aperture size can not be determined from the results.

3.2.4 Scanning non-uniformities

The SNOM system in chapter 5 uses a Melles Griot Nanomax-HS 3 axis flexure stage, to allow the imaging of larger areas. It was noticed during the scanning that the acquired images were distorted. The effect was characterised using the topography of a phase mask. Figure 3.14 shows two scans of the phase mask, between the two scans the phase mask was rotated by 90 degrees. The angle of the rulings of the phase mask differ by $\approx$97 degrees and is the result of cross talk between the x and y channels of the piezo stage [16]. The stage also exhibits a variation in the calibration of the piezo as a function of distance along the grating, an example of this

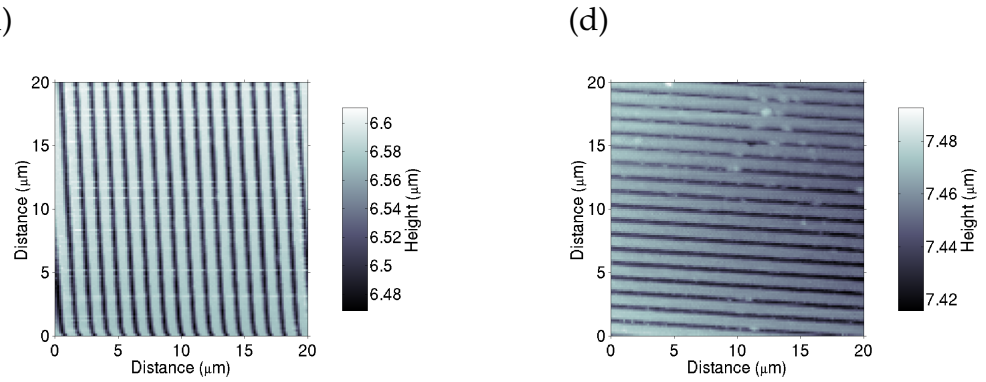

Figure 3.14: Two false colour images showing the topographical of a 1.136 μm period phase mask. The phase mask has been rotated by 90 degrees between scans.

change in can be seen in figure 3.15. It was decided that due to the spa-

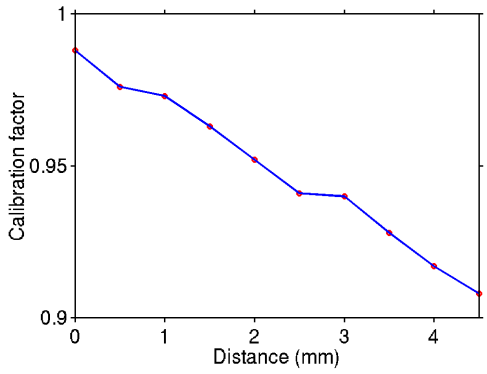

Figure 3.15: A plot showing the calibration factor of the piezo x axis as a function of the stepper motor position.

tial dependence of the distortion it was not feasible to correct for it with image processing [17]. This distortion is evident on the images presented in the chapter 5. However the nature of investigation did not require accurate spatial measurements, and thus did not impede the research. The increased scanning range of the stepper motors also made the selection of this stage preferable. To assist in the analysis of the data, the sample is orientated with the optical axis collinear with the x axis. The variation in the calibration of the stage generated large errors in the spatial measurements

shown in chapter 5. To achieve accurate spatial measurements the sample was removed and calibrated without changing the xy position.

The remaining work presented in this thesis uses the Melles Griot Nanoblock piezo stage, an image of a calibration sample is shown in figure 3.16. The scan is slightly rotated due to the alignment of the sample relative to the axis, however there are no distortions. The stage exhibited limited scan range of 18 μm in the x and y axis, as a result of the age of the stage.

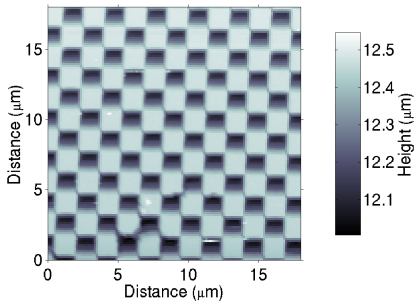

Figure 3.16: Topography image of a checkerboard grating (MikroMasch silicon grating TGX01) using the Nanoblock piezo stage. The period of the grating is 3$\pm$0.005 μm

3.3 Chapter summary

This chapter documents the construction and characterisation of the SNOM system used to acquire the data presented in this thesis. The chapter includes a comprehensive description of the near-field probe fabrication process. SEM analysis has shown the fabricated silica probes to have a reproducible tip features of $\approx$ 60 nm. SEM results have also confirmed that the aluminium coating process produces probes with aperture sizes of $\approx$ 100 nm.

Documentation is included on the feedback and scanning mechanism used to scan the probe about the sample surface at a constant height. Details of

the heterodyne detection system used to measure the complex electric field are also outlined. There is an additional discussion of the environmental isolation required to reduce noise in the SNOM and interferometer system. The thermal and mechanical stability of the interferometer was sufficient enough to provide a optical phase constancy of 210 degrees/hour.

The chapter concludes by analysing the performance of the fully operating system, including a description of the scanning non-uniformities observed in one of the piezo-electric stages.

3.4 Future work

A substantial part of this project was the development of the heterodyne SNOM technique described in this chapter. During the investigations valuable developments to the system became evident, this section identifies some of these improvements.

A substantial improvement to the system would be the introduction of a new piezo-stage, with a larger spatial range and minimal scan distortions. To increase the bandwidth of the scanning system the phase of the tuning fork signal can be employed as the feedback error signal [18]. The quality of the near-field probes could also be significantly improved by employing ion beam etching to produce the aperture in the end of the coated probes. This may also be possible to fabricate polarising SNOM probes, where the aperture of a coated probe is designed to collect only a single polarisation. The stability of the heterodyne detection system could be improved by using polarisation maintaining fibre, details of which are given in section 5.7.

3.5 References

[1] A. Sayah, C. Philipona, P. Lambelet, M. Pfeffer, and F. Marquis-Weible. "Fiber tips for scanning near-field optical microscopy fabricated by normal and reverse etching". *Ultramicroscopy*, 71(1-4):59–63, 1998.

[2] E. Betzig and J.K. Trautman. "Breaking the diffraction barrier: Optical Microscopy on a nanometric scale". *Science*, 251(5000):1468–1470, 1991.

[3] G. A. Valaskovic, M. Holton, and G. H. Morrison. "Parameter Control, Characterization, and Optimization in the Fabrication of Optical-Fiber near-Field Probes". *Applied Optics*, 34(7):1215–1228, 1995.

[4] Sutter Instrument Company Operational Manual. *P-2000 Micropipette Puller*, volume Rev. 1.0/060297.

[5] C. W. J. Hillman. *Scanning near-field optical microscope characterisation of microstructered optical fibre devices.* PhD thesis, University of Southampton, 2002.

[6] S Madsen, N.C.R. Holme, P.S. Ramanujam, S Hvilsted, J.M. Hvam, and S.J. Smith. "Optimizing the fabrication of aluminium-coated fiber probes and their application to optical near-field lithography". *Ultramicroscopy*, 71:65–71, 1998.

[7] J Strong, H.V. Neher, A.E. Whitford, C.H. Cartwright, and R. Hatward. *Procedures in Experimental Physics*. 1938.

[8] K. Karrai and R. D. Grober. "Piezo-electric tuning fork tip-sample distance control for near field optical microscopes". *Ultramicroscopy*, 61(1-4):197–205, 1995.

[9] J.D. Mills. *An investigation of Phase-Mask Diffraction Patterns And Fibre Bragg Gratings With Scanning Near-Field Optical Microscopy*. PhD thesis, University of Southampton, 2001.

[10] Melles Griot Ltd. *Nanomax-HS 3 axis flexure stage*. Instruction Handbook for the Melles Griot Nanopositioning modular system. Melles Griot, Cambridge, 1998.

[11] M.L.M. Balistreri, J.P. Korterik, L. Kuipers, and N.F. van Hulst. "Phase Mapping of Optical Fields in Integrated optical waveguide structures.". *Journal of Lightwave Technology*, 19(8), 2001.

[12] B.A.W.H Knarren. *Application of optical fibres in precision heterodyne laser interferometry*. PhD thesis, TU Eindhoven, 2003.

[13] T. Kalkbrenner, M. Graf, C. Durkan, J. Mlynek, and V. Sandoghdar. "High-contrast topography-free sample for near-field optical microscopy". *Applied Physics Letters*, 76(9):1206–1208, 2000.

[14] B. Vohnsen and S. I. Bozhevolnyi. "Optical characterization of probes for photon scanning tunnelling microscopy". *Journal of Microscopy-Oxford*, 194:311–316, 1999.

[15] S. I. Bozhevolnyi and E. A. Bozhevolnaya. "Near-field imaging of the interference pattern of counterpropagating evanescent waves". *Optics Letters*, 24(11):747–749, 1999.

[16] R. Weisendanger. "Scanning Probe Microscopy and Spectroscopy". pages 95 –97. Cambridge University Press, 1994.

[17] D. Courjon. *Near-field microscopy and near-field optics*. Imperial College Press, 2003.

[18] W.A. Atia and C.C. Davis. "A phase-locked shear-force microscope for distance regulation in near-field optical microscopy". *Applied Physics Letters*, 70(4):405–407, 1997.

Chapter 4

Characterisation of fibre Bragg gratings

4.1 Chapter introduction

This chapter presents some of the data acquired during the investigation of a uniform fibre Bragg gratings using the previously described SNOM system. Direct imaging of the complex electric fields in fibre grating was achieved by probing the evanescent field of the fibre modes. The chapter starts by introducing fibre Bragg gratings and motivation behind the work. This is followed by a description the fibre grating sample and the experimental technique used to acquire the SNOM data. The results and analysis section presents the evanescent field distributions observed at the different spectral regions of the waveguide. The chapter concludes by summarising the key results and discussing potential future work.

4.1.1 Fibre Bragg Gratings

Fibre Bragg gratings (FBGs) have revolutionised the field of telecommunications and fibre sensor technology. They are the key component used

in dispersion compensation, add/drop multiplexors, distributed feedback (DFB) lasers and many others [1]. The technology is based on the modulation of the refractive index of the core of a optical fibre. The periodic modulation acts as a selective mirror reflecting wavelengths that satisfy the Bragg condition. The refractive index modulation is produced by the photosensitivity of the optical fibre and was first observed in germanosilica fibres by Hill *et al.* in 1978 [2]. The refractive index modulation or grating was permanently written into the core of the optical fibre using a argon ion line at 488nm. A back reflection from the end face of the fibre generated a standing wave in the fibre, the high intensity at the antinodes altered the refractive index to generate a modulation with a period of half the wavelength.

The application of these devices was limited, as the method was unable to produce gratings with resonances in the infrared, for use in telecommunications. In the late 1990's an alternative technique by Meltz *et al.* was introduced [3]. The research showed that a relatively large increase in the refractive index could be created by exposing the core through the side of the fibre. The large index change was induced by making the exposure wavelength close to a germanium absorption peak at ≈240nm. The mechanism of the photoinduced refractive index change is not fully understood, however it has been associated to the germanium-oxygen defects [4]. The form of the induced index modulation is controlled by the pattern of the exposing field, allowing the operating wavelength to be independent of the exposure wavelength. The significant advantage is the tunability of the technique enabling fabrication of components for use in the near infrared. The periodic ultraviolet pattern used in the inscription is generated by two beam interference, this may be achieved directly or via a phase mask. Each method having distinct advantages and disadvantages. The technique has numerous parameters such as: induced index change, length, apodisation, chirp, fringe tilt, phase shifts and superstructure. Varying these parameters permits the properties of the grating to be

tailored to the application. Comprehensive reviews of UV written fibre Bragg gratings can be found elsewhere [5,4,1].

4.1.2 Investigation of fibre Bragg gratings with SNOM

The characterisation of the FBG is principally achieved by reflection and transmission spectra of the gratings, these can be acquired during the exposure process to serve as feedback. However the spectra do not give any insight into the mechanisms behind the source of the imperfections in the structure of the grating. One of the most common causes is the low spatial coherence of the excimer writing laser. Insight into these mechanisms can only be obtained by direct measurement of the refractive index profile, an example of this is the work by Dragomir *et al.* [6] who have imaged the refractive index perturbation in a fibre grating using a differential interference contrast imaging technique. The investigation reveals addition index structure suspected to be generated by the interference pattern from the phase mask, used to fabricate the grating [7].

However these types of imaging techniques are not able to investigate the sub-wavelength refractive index modulation and the electric field distribution concurrently. SNOM offers a unique capability of providing a tool to directly measure both the index and field directly. The disadvantage with the technique is the necessity to gain access to the evanescent field, which requires the removal of a large portion of the cladding, therefore making the technique destructive. Previous studies have validated the use of SNOM as an effect tool for the characterisation of FBGs [8,9]. This chapter presents a extension of this work. The development of the SNOM system permits investigation of the gratings at the design wavelength in the NIR. This replaces the former technique of measuring the second order Bragg reflection or fabricating specialised gratings with first order resonance in the preceding SNOM spectral band. This work concentrates on the imaging of the standing waves generated in the fibre Bragg grating

and the information which can be obtained from them.

The motive of the work is to acquire details about the physical operation of the gratings and compare these findings against theory. The structures are also interesting to investigate for pure scientific interest, as they present an example of an operational one-dimensional photonic band gap crystal. The theory behind the operation of one-dimensional band gap structures and thus fibre Bragg gratings is well understood. However the ability to directly map the electric field distribution inside photonic bad gap structures is necessary for devices that include defects such as microcavity lasers [10] and bent waveguides [11]. This investigation is hoped to be an initial step into the investigation of two and possibly three dimensional photonic crystals.

4.2 Imaging fibre Bragg gratings

This section will describe the experiment method used to acquire the data shown in the following section, it will begin with a brief description of the fibre Bragg sample and its preparation to permit access to the gratings evanescent field.

4.2.1 Fibre Bragg grating sample

The sample used in this investigation was fabricated for a prior project and was original designed to be used as part of a grating-frustrated coupler [12]. The grating was written using the two beam interference from a Lambda Physik EMG-150 KrF excimer laser. The resulting grating had a uniform index modulation. A summary of the samples properties is given in table 4.1. The fibre Bragg grating was then glued using EpoTek 353ND epoxy resin into a groove cut in a Pyrex glass block of dimensions 44mm $\times$ 25mm $\times$ 10mm. The groove which was cut into the surface of the block

Bragg wavelength (λ_B):	1535nm
Single mode cut-off unexposed fibre:	1250nm
Fibre cladding diameter	125μm
Cladding material:	Silica
Core material:	Silica/Germania/Boron
Exposure Method:	Side exposure for ≈10mins to excimer (KrF) laser interfermeter
Index modulation (Δn):	$\approx 1 \times 10^{-3}$
Grating length:	15mm

Table 4.1: Properties of the fibre Bragg grating used in this investigation.

had a radius of 1m, the epoxy glue allows the fibre to be held securely while the sample was polished. The grating was positioned at the highest point of the groove. The sample was subsequently polished until the minimum depth of the cladding was estimated to be 1μm [13], the shallowest point corresponds to the location of the grating. The pigtails were removed and the end faces of the block polished to allow optical coupling. Removal of the pigtails ensured that the polarisation of the mode inside the FBG was identical to that initially coupled. A more thorough description of the fabrication and preparation of the sample can be found elsewhere [8]. A diagram of the final prepared sample is illustrated in figure 4.1.

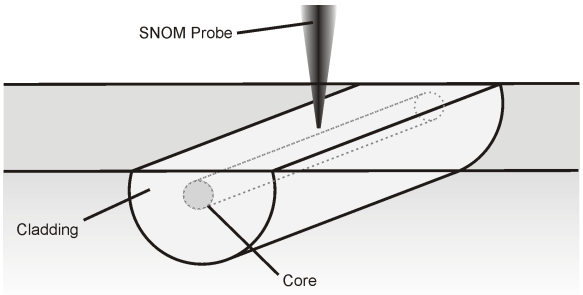

Figure 4.1: A cross section of the fibre grating, illustrating the removal of the cladding to permit access to the evanescent field.

The transmission and reflection spectra serve a very important role throughout this investigation, as they provide information about the state of the operation of the fibre Bragg grating. Figure 4.2 shows the reflection and transmission spectra for the grating, the stop band is visible at 1535nm.

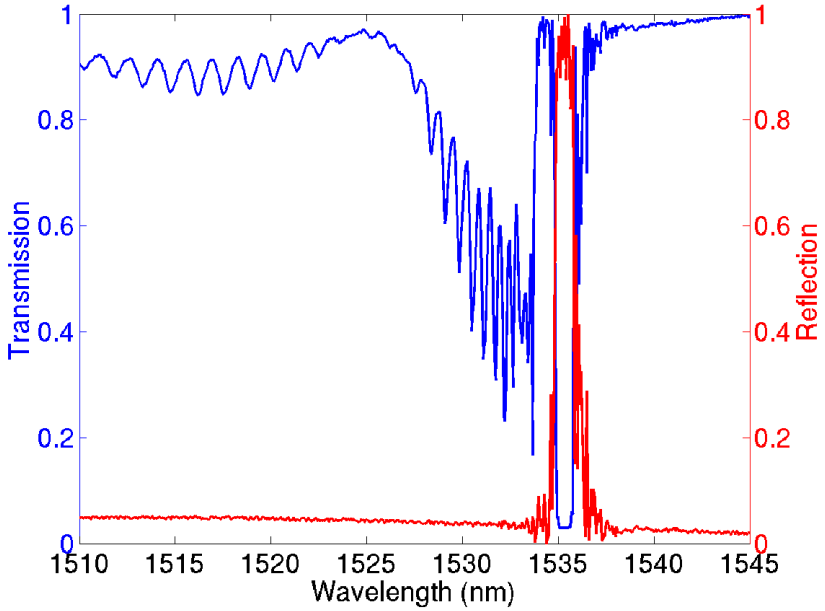

Figure 4.2: Transmission and reflection spectra of the fibre Bragg grating.

The transmission spectrum shows two regions of decreased transmission at wavelengths below the stop band. A corresponding increase is not seen in the reflection spectrum and thus the light must be leaving the system. This loss is the result of the core mode coupling to radiation modes. The modulation is a consequence of phase matching between the radiation modes and cladding modes. The cladding modes being confined by the cladding-epoxy interface. The end result is that the core mode couples into discrete counter propagating cladding modes, each cladding mode having an associated dip in the transmission spectra. The generated cladding modes are extremely lossy and as a result these counter propagating modes are not observable in the reflection data.

The invasive nature of the preparation technique promotes concern that

it may perturb the mode and therefore change the operation of the grating. The ideal way in which to characterise this effect is a comparison of the transmission and reflection spectra before and after polishing. Unfortunately an accurate spectrum was not available prior to polishing. An alternative technique is a comparison between the spectra of orthogonal polarisations. The removal of the cladding will perturb the TE and TM modes by a different magnitude, therefore changing the propagation constant and the hence the Bragg wavelength (λ_B). Figure 4.3 shows the transmission spectra for the grating with both TE and TM polarised light.

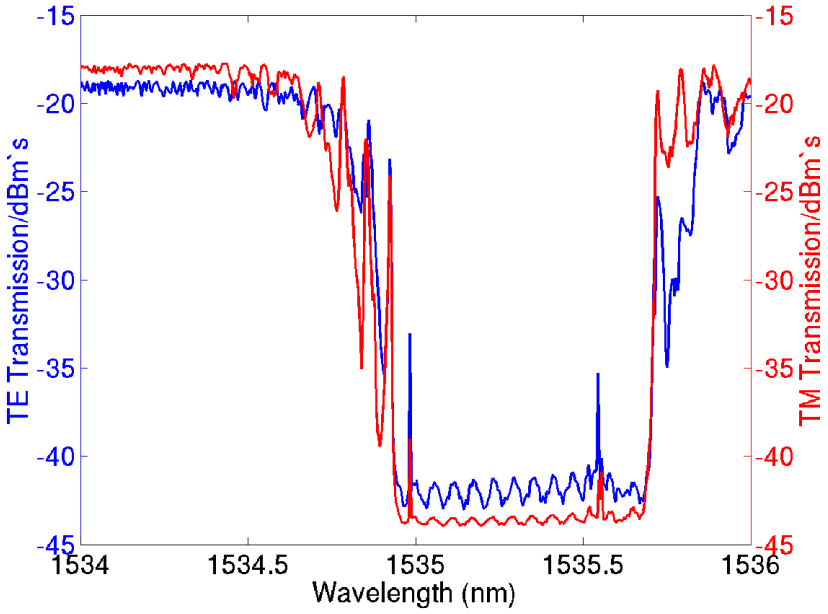

Figure 4.3: The transmission spectra of the fibre Bragg grating near the stop band for the TE and TM modes.

The figure shows the spectra for TE and TM modes in the stop band region which shows no measurable shift in frequency of the stop band. However on either side of the stop band there are additional features not associated with cladding mode resonances. This additional structure is a common feature of in uniform gratings and may be qualitatively explained by the "effective medium picture" developed by Sipe *et al.* [14]. For frequencies outside the stop band the boundaries of the grating act as abrupt interfaces

and thus the system can be treated like a Fabry-Perot filter. At the wavelengths satisfying the cavity conditions, the light is trapped oscillating inside the grating. The resulting reflection and transmission spectrum have a familiar sinc like function. Similar features can be seen in the transmission spectrum shown in figure 4.3 on both the short and long wavelength sides of the stop band.

The resonances in the short wavelength edge of the spectrum are also expected to be enhanced by another effect most commonly associated with apodised gratings. The effect is produced by the increase in the space averaged index of the core mode by the grating. This additional mechanism is expected due to the large induced index change during the fabrication of the sample [12]. The increase shifts the Bragg wavelength to longer wavelengths, the largest effect being in the centre of the grating where the index change is greatest. Thus at wavelengths near the lower edge of the stop band the ends of the grating act as short Bragg gratings, whereas the centre of the grating is transmitting, this results in additional internal Fabry-Perot resonances at the short wavelength edge of the stop band [15]. The transmission spectra shown in figure 4.3 exhibits such resonances. The remaining losses are generally associated with fabrication defects such as non-uniformity of the index modulation and the average index along the grating [12].

4.2.2 Experimental procedure

This section describes the general procedure used to collect the SNOM data presented in the following section and in chapter 5. Figure 4.4 shows the sample arrangement. The sample is held stationary on the SNOM stage. Light is coupled into the sample with a single mode fibre mounted on a Martock flexure stage and index oil is used to increase the coupling efficiency and suppress back reflections. For the FBG sample a 6 degree Pyrex glass wedge was placed on the end face of the sample to prevent

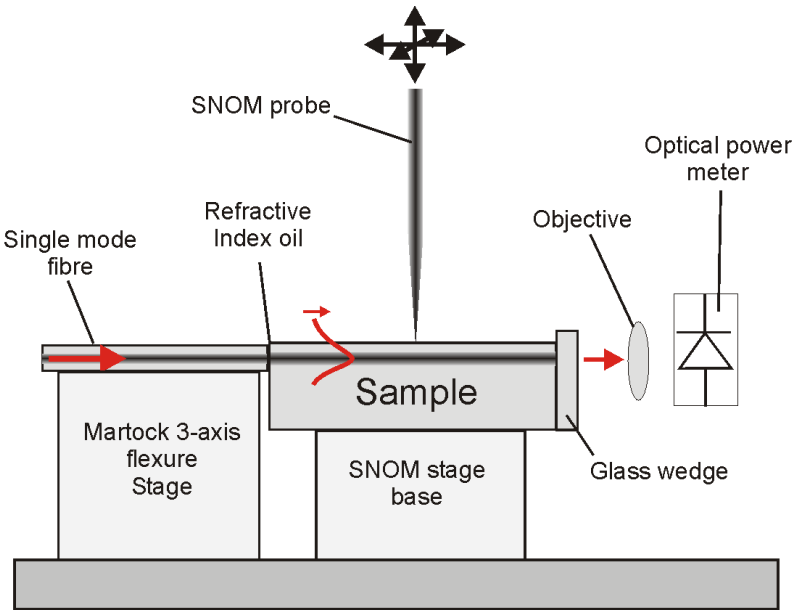

Figure 4.4: Schematic of the SNOM arrangement.

back reflections. Refractive index gel was used to prevent reflections from the interface between the grating sample and the glass wedge. The output light was collected using an anti-reflection coated objective and monitored using an Agilent power meter. An un-coated near-field probe was used throughout this investigation, due to the low quantity of scattered propagating light. The sample was highlighted with the 633nm light from the HeNe laser, the stereo microscope was then used to position the SNOM tip approximately 15 μm above the waveguide. The insulating case was enclosed and the room is vacated to allow the apparatus to thermally stabilise. Scanning was then implemented from outside the room. One of the addition concerns with this investigation was the thermal stability of the fibre Bragg grating. Some of the data was taken on or near resonances with spectral features of 10 pm, thus small temperature changes can induce large changes in the standing wave. To minimise these effects the laboratory was kept isolated and transmission spectra were acquired at frequent intervals to inspect the spectral change. Figure 4.5 shows a series of transmission spectra taken at 6 hour intervals. The data shows a spectral drift of 9 pm and a 7% drift in transmitted power over the 12 hour

period. The polarisation coupled into the sample was also checked, however this was much less frequent due to the additional disruption caused to the system. Polarisation changes were only detectable after the system was realigned.

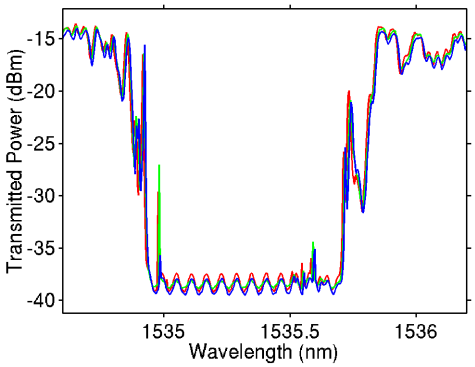

Figure 4.5: Transmission spectra near the stop band of the fibre grating, the red, blue and green lines demonstrate the transmitted power at 0, 6 and 12 hours. The core mode had TE polarisation.

4.3 Results and analysis

This section presents and discusses some of the data acquired from the previously described fibre grating. The section will describe the field distributions observed at different spectral positions.

4.3.1 Off-resonance

This section starts by briefly discussing electric field distribution in a spectral region away from the grating resonances where $A_b = 0$. Away from the grating resonances the dominant contrast mechanism is the index modulations in the core (see section 2.6). Figure 4.6 shows a false colour image of the electric field magnitude well above the stop band and the cladding

mode resonances. The image shows a relatively flat profile with little evi-

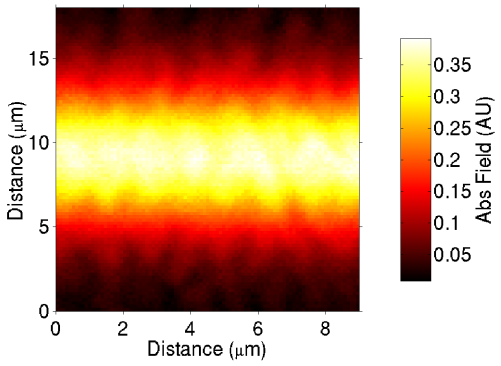

Figure 4.6: The electric field distribution off-resonance, showing the refractive index change in the core. $\lambda = 1600\text{nm}$.

dence of a perturbation at the period of the refractive index modulation. It is expected that the refractive index variations are not large enough to produce sufficient contrast at the depth of the cladding. The data presented in the following sections is taken at the same location on the sample as that shown here. Thus the effects of the grating index on the electric field distributions can be neglected.

4.3.2 Cladding mode resonances

The section explores the standing waves excited due to the interference between the forward propagating core mode and the backward propagating cladding modes. Figure 4.7 shows a typical set of SNOM data taken in the cladding mode region. The images are displayed using a false colour map, which are defined on the right of the image. The electric field distribution is the result of interference between the core propagating mode and the counter propagating cladding mode. The core mode propagates into the waveguide from the right to left of the page and thus the back reflection travels from left to right, and will be the scanning convention used in this thesis. The topographical data shown in (a) shows that the surface is flat

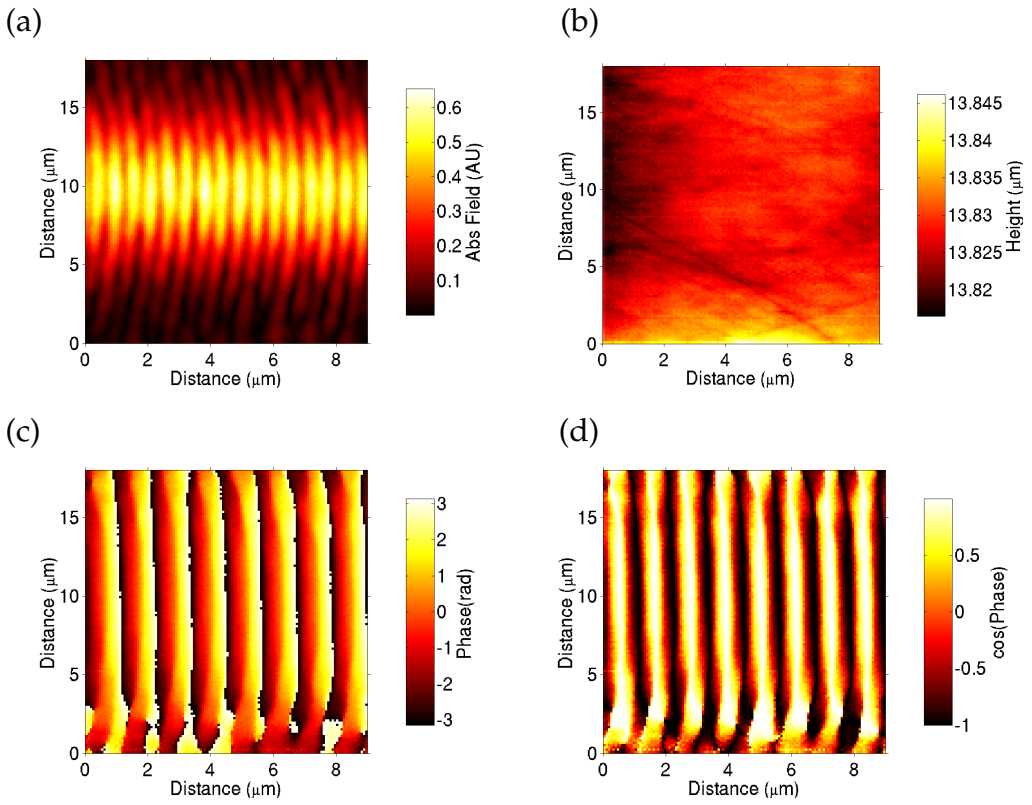

Figure 4.7: SNOM data taken at the surface of a fibre Bragg grating. (b) shows a false colour image of the topography of the surface. (a) and (c) present images of the electric field magnitude and phase. (d) shows the cosine of the phase. $\lambda = 1518.9$ nm.

to within ± 15nm, therefore removing any potential imaging artifacts. The small scratches seen at the bottom of the page are polishing defects, however inspection shows no associated topographical artifacts. It should be noted that the electric field plotted in this thesis is the absolute value if not otherwise stated. The field modulation reveals a low back reflected component as expected for a cladding mode. Using the FFT technique described in section 2.3.1.1 the visibility ratio (A_b/A_f) immediately above the core is $\approx$0.18. Cross sections shown in figure 4.8 illustrate the electric field variation along the optical axis. The red circles show the experimental data, while the blue lines correspond to a fit generated from the expressions presented in section 2.3. The fit is a function of four parameters, the magnitude of the forward and backward propagating components ($\mathrm{A_f}$ and $\mathrm{A_b}$), the phase between the components (γ) and the effective refractive index of the mode ($\mathrm{n_{eff}}$). The parameters of the fit are given in the figure caption. The fit agrees very well with the experimental data. The fluctuations visible on the electric field magnitude are suspected to be the result of phase errors in the refractive index profile of the grating, producing various cladding modes. The phase errors are generally associated with the low spatial coherence of the excimer writing laser [9]. The data previ-

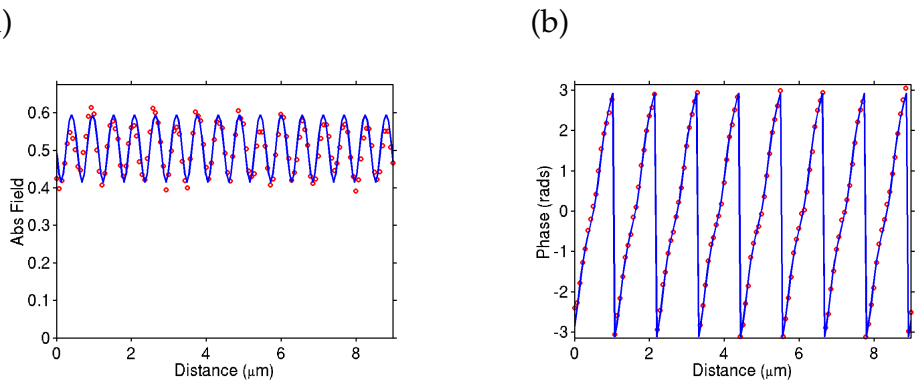

Figure 4.8: (a) and (b) cross sections of the electric field magnitude and phase along the optical axis of the fibre grating. Experimental data is shown by red circles and a fit is shown by the blue lines. The parameters of the fit are $\mathrm{A_f} = 0.491$, $\mathrm{A_b} = 0.088$, $\gamma = 0.43$ rad and $\mathrm{n_{eff}} = 1.46$.

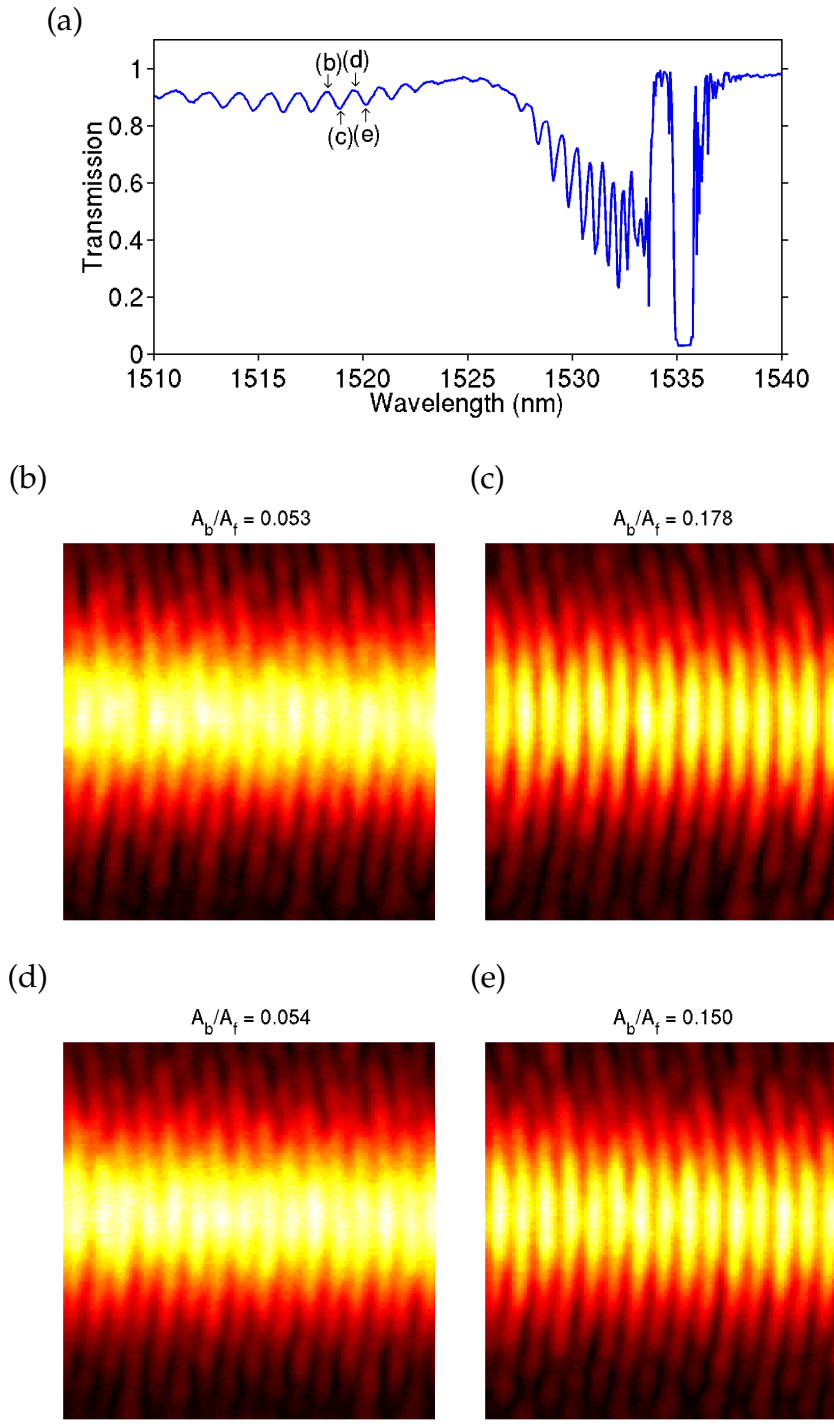

Figure 4.9: (a) shows the transmission spectra for the grating, the arrows mark the spectral location of the electric field distributions presented in (b)-(e).

ously shown was taken at a dip in the transmission spectra, corresponding to a specific cladding mode resonance. The resonance increases the backward propagating mode and thus produces a higher visibility standing wave. This is verified by series of scans taken on and off cladding mode resonances in figure 4.9.

The spectral location of each of the scans is marked on the transmission spectra presented in (a). The visibility (A_b/A_f) is marked above each scan proving the relation between the cladding mode resonance and the visibility of the standing wave. In this way the visibility may be used to evaluate the magnitude of the cladding modes and thus the radiative modes as a function of distance along the grating. To quantify the relative magnitude of the counter propagating components the modal overlap at the surface must be evaluated. In the waveguide geometry presented here this is quite challenging, however this task would be made significantly easier by imaging a grating within a D-fibre.

Another feature of the cladding modes is the curved nature of the standing waves as demonstrated in figure 4.10. This effect is only seen in the

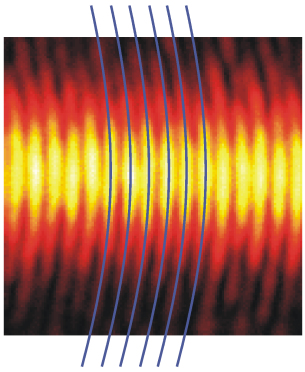

Figure 4.10: A false colour image of the standing wave produced between a cladding mode and the core mode. The lines illustrate the curved nature of the standing wave.

shorter wavelength cladding mode region, these correspond to the high order modes cladding modes. The effect is suspected to be the result of

the leaky nature of the cladding mode, this may also be enhanced by the polishing of the cladding. As it is not truly guided the wavefronts of the mode may not flat; consequently the phase of the cladding mode will vary across the optical axis and thus produce a lateral shift in the position of the standing wave. Again in order to verify this effect the exact solution of the cladding mode must be calculated in order to determine the cross section of the field at the surface.

It has been theoretically and experimentally shown by several authors that cladding mode resonances are dominated by symmetric modes [16, 17]. Throughout this investigation the cladding modes were also found to be predominately symmetric. However in one spectral region where the lowest order cladding modes are generated, a distinct alternating fringe pattern is observed, shown in figure 4.11 (b). The spectral location of the pattern is defined by the vertical line in (a). The distribution is suspected to be the result of interference between a core mode (LP_{01}) and an antisymmetric mode such as a (LP_{11}). The situation is graphically represented in figure 4.12. The lobes of the even mode have opposing E-field directions, this can also be described as a π phase difference between the lobes. This causes one lobe to destructively interfere while the opposing lobe constructively interferes, thus producing the alternating fringe pattern. The phase information in figure 4.11(c) shows the result of the cladding mode axial phase shift. To confirm this hypothesis the cladding modes for this structure must be calculated, however this is beyond the scope of this thesis.

The next section moves to different spectral region and investigates the electric field distributions around the stop band of the grating.

4.3.3 Core mode resonances

At the stop band the LP_{01} core mode satisfies the phase matching condition described in section 2.5, producing a counter propagating LP_{01} mode. Figure 4.13 commences this section by illustrating the general properties

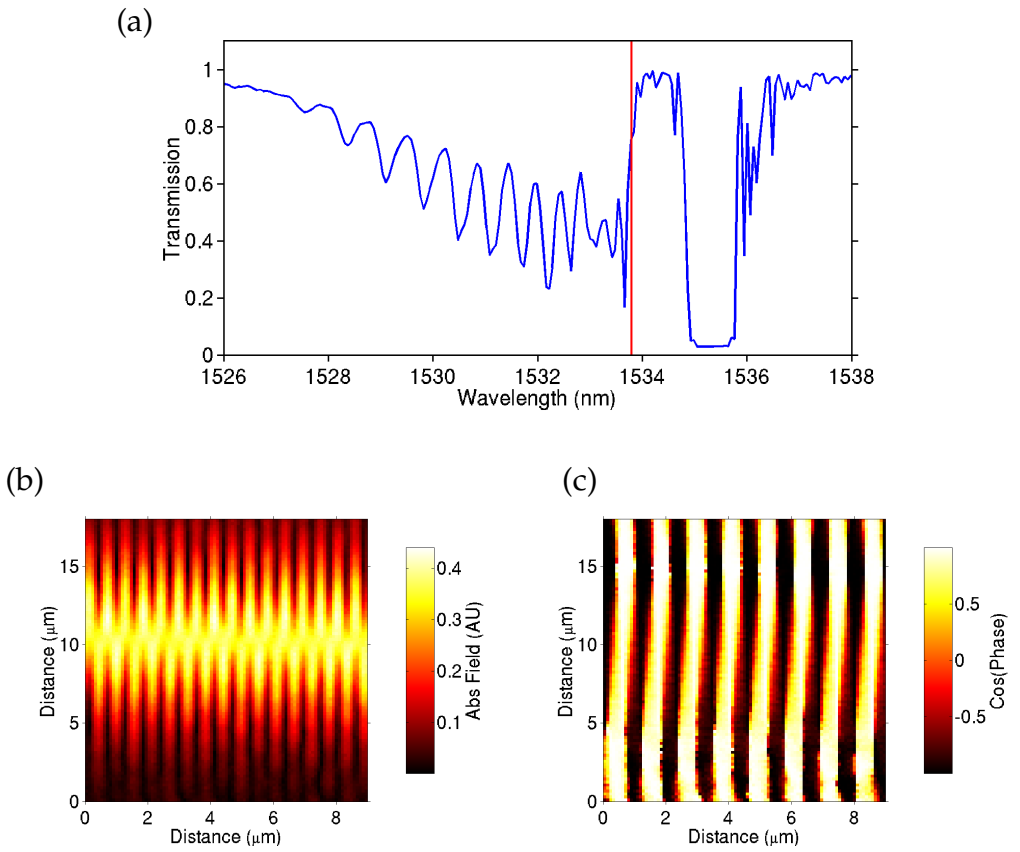

Figure 4.11: (a) shows the transmission spectra of the sample, the vertical line specifies the wavelength at which the electric field amplitude and phase in (b) and (c) was acquired. The core mode had TM polarisation and a wavelength of $\lambda = 1533.8$nm.

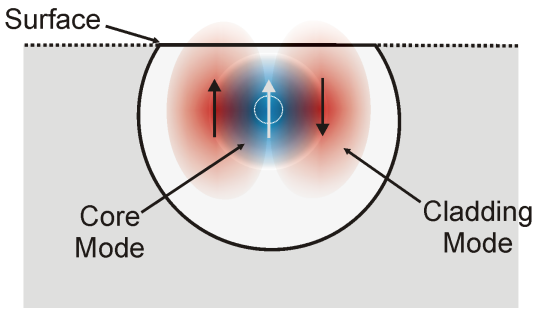

Figure 4.12: Cross-section of the grating sample, showing a low-order LP_{11} mode in red and the LP_{01} mode in blue. The polarisation of each mode is defined by the associated arrows.

of the standing waves generated in this region. The spectral location of

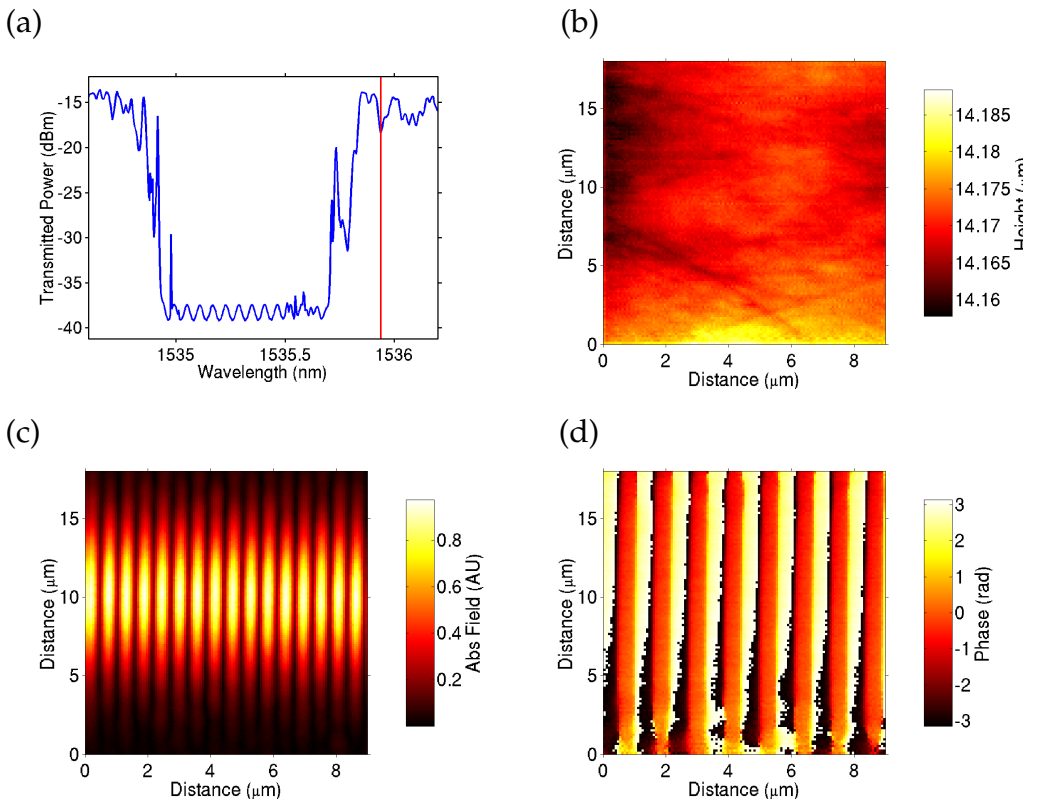

Figure 4.13: A set of SNOM data taken at the wavelength specified in (a). (b), (c) and (d) presents the topographical, E-field magnitude and phase respectively. $\lambda = 1535.94\text{nm}$.

the acquired data is highlighted in (a). The electric field displays a much higher contrast standing wave than that observed in the cladding mode region. This is the result of significantly greater modal overlap and coupling strengths between the counter propagating modes. The greater visibility produces substantially different electric fields, which is made clearer by cross sections along the optical axis shown in figure 4.14.

Again both the amplitude and phase variation fits well to the simple theory. The phase variation is very distinctive angular shape, a result of the visibility being close to unity. Similar phase dependence has been seen in the evanescent standing wave patterns produced at a prism interface [18].

One of the unique features of this SNOM arrangement is the ability to

(a) (b)

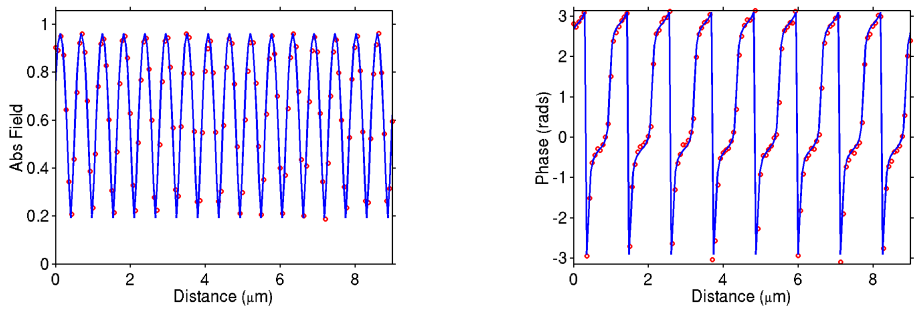

Figure 4.14: Cross sections of figure 4.13 showing the variation of the electric field magnitude (a) and phase (b). The SNOM data is represented by red circles and the fit by blue line. The parameters of the fit are $A_f = 0.57$, $A_b = 0.385$, $\gamma = 0.44$ rad and $n_{eff} = 1.47$.

measure the spatial dependence of the standing wave with nanometer resolution at different wavelengths. Figure 4.15(a) shows the standing wave as a function of wavelength, across the stop band. The image is compiled

(a) (b)

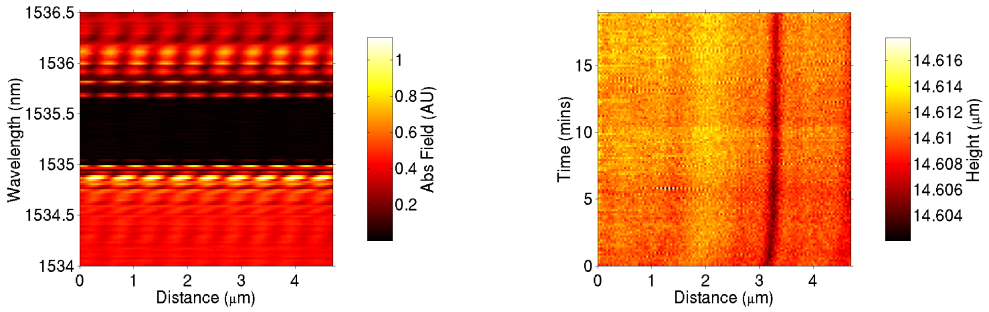

Figure 4.15: (a)A false colour image showing the standing wave as a function of wavelength. (b) Corresponding topographical data.

from a series of lines scans acquired at the same position along the optical axis of the waveguide. Each line scan is taken at a different optical wavelength. The topographical data shown in (b) exhibits a ≈ 5 nm surface feature, the constant location of the defect confirms the spatial repeatability. The dark band across the centre of (a) indicates the stop band region.

The collected field is negligible in the band, indicating that all the light is reflected by the grating before reaching the location of the SNOM probe. The nodes of the standing wave are visible in (a), the location of the nodes are seen to change position as a function of wavelength. The data yields several pieces of information. The most obvious is the magnitude of the forward and back propagating components as a function of wavelength. Figure 4.16 shows the magnitude of the forward (A_f) and backward (A_b) propagating modes as a function of wavelength. The red and green lines

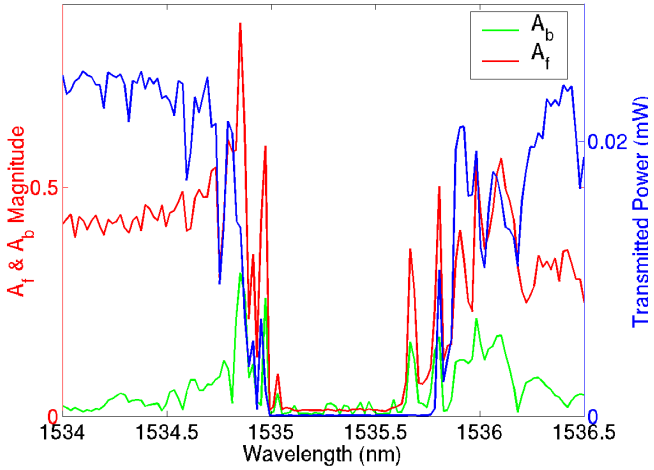

Figure 4.16: Plot showing the magnitudes of the forward and backward propagating components. The blue line represents the transmitted power.

represent the amplitude of the forward and backward propagating components respectively and the blue line presents the transmission spectra which was concurrently acquired. The transmission spectra defines the stop band region from 1535 nm to 1535.8 nm. The plot again shows very little light propagating in either direction in the stop band. Attempts to image the field closer to the beginning of the grating were hampered due to the increased depth of the cladding and consequently a reduced amplitude of the evanescent field.

The most prominent standing waves and thus largest values of A_f and A_b are generated at the short wavelength edge of the stop band. These

are suspected to be the result of the Fabry-Perot cavity generated by the ends of the grating as previously discussed in section 4.2.1. The present SNOM system is adequate for a qualitative analysis of forward and backward propagating components. However the accuracy of this technique is limited due to wavelength dependent birefringence of the fibre, these effects are discussed in more detail in section 5.5.3.

The other piece of information available from figure 4.15 is the spatial position of the standing wave. The location of the standing wave can be represented by its relative phase as a function of wavelength. This is shown in figure 4.17. The transmission spectra is also plotted to provide a reference.

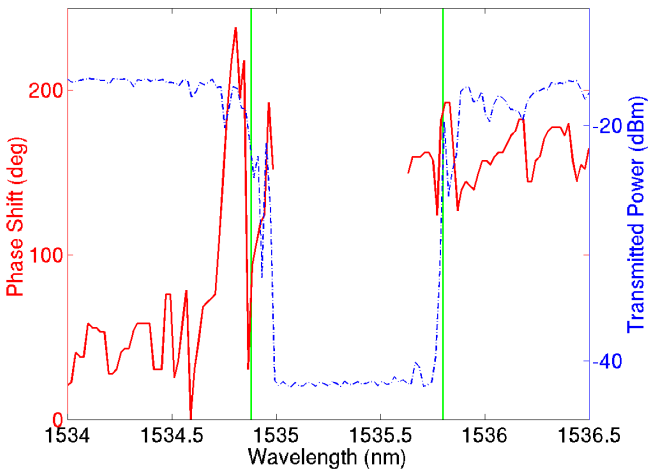

Figure 4.17: A plot showing the relative spatial phase of the standing wave as a function wavelength across the stop band.

The phase in the stop band region is not defined due to the low magnitude of the standing wave. The large feature at 1534.8 nm is again the result of an internal cavity mode, the phase of which is purely dependent on the length of the grating. The smaller features are also expected to be due to internal resonances. The plot shows a distinct change in the phase of the standing wave across the stop band. This spatial shift of the electric field is predicted explicitly for fibre gratings [19]. It is also a feature associated with photonic band gap systems [20]. In fact the stop band can be considered to be a direct consequence of the phase shift. The width of the

stop band is defined by the degree to which the photons are distributed in the high and low index regions. At the long wavelength edge of the stop band the electric field is concentrated in the high index region as shown in figure 4.18 (a). Using the Bragg condition 2.41 this defines the high wavelength edge of the stop band. Conversely at the short wavelength edge the energy of the field is concentrated in the low index regions, thus defining the lower wavelength edge of the stop band shown in figure 4.18 (b) [21]. A complete description of this phase shift can be acquired by solving the Maxwell equations for the system. The corresponding result is a π phase

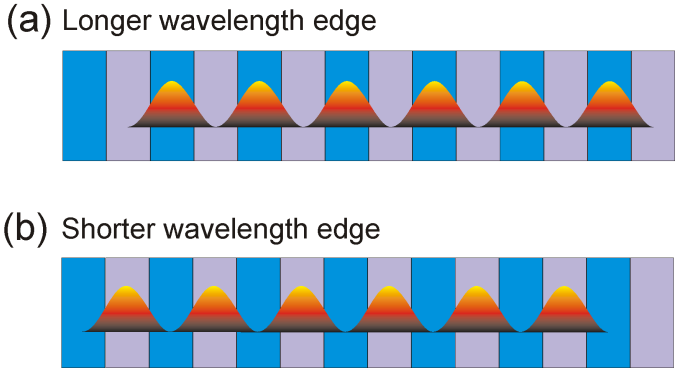

Figure 4.18: Diagram showing the relative positions of the standing wave across the stop band. (a) shows the situation at the longer wavelengths, while (b) the shorter wavelengths. The blue areas define the regions of high refractive index. After reference [20].

change in the location of the standing wave across the stop band. Figure 4.19 illustrates this shift, by presenting two scans of the measured electric field magnitude above and below the stop band. The image is composed of two halves, the top half was acquired at the lower wavelength edge of the stop and the bottom half was acquired at the higher wavelength edge of the stop band. The position of the two scans was registered by the location of surface defects on the matching topography. The image clearly shows the π shift in the location of the standing waves. The respective wavelengths of the two halves of the image are indicated by the vertical lines in figure 4.17. Inspection of the positions show that the electric field images are taken very near the Fabry-Perot resonances. However the data

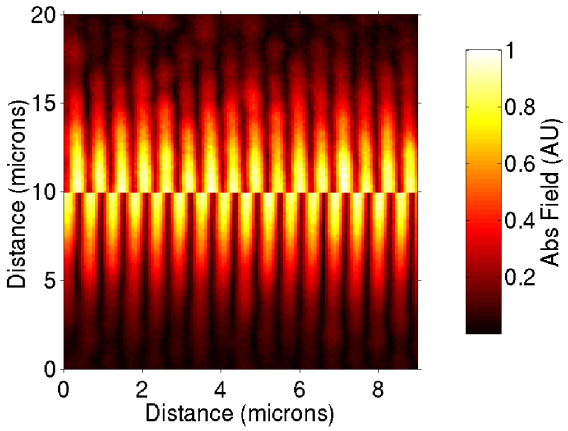

Figure 4.19: A composite plot of the electric field magnitude either side of the stop band. The top half is acquired at 1534.9 nm and the bottom at 1535.8 nm.

presented in figure 4.17 conclusively shows the standing wave shift.

4.4 Conclusions

This chapter has shown the direct imaging of the amplitude and phase of the standing waves within a fibre Bragg grating as a function of wavelength. The work has presented the first direct evidence for several intrinsic features of fibre Bragg gratings which have previously only been theoretically predicted.

The imaging is achieved by measuring the evanescent fields of the modes propagating in the fibre grating. Access to the fields is achieved by polishing the cladding of the fibre to within 1 to 2 μm of the core. Transmission spectra with orthogonal polarisations confirmed the polishing did not significantly perturb the mode.

The analysis of the evanescent field away from the resonances of the fibre Bragg grating showed no observable contrast due to the refractive index

modulation of the grating.

In the spectral region were cladding modes are excited, standing waves were observed to form between the forward propagating core mode and the backward propagating cladding modes. The visibility of the standing wave permitted the measurement of the relative amplitudes of the counter propagating modes. An association between these amplitudes and the spectral characteristics was observed, however an exact relationship requires knowledge of the modal cross section. A standing wave was also observed between the forward propagating core mode and an antisymmetric cladding mode, producing an alternating fringe pattern.

In the stop band region no optical signal is observed due to the light being completely reflected prior to the position of the probe. An investigation of the electric field amplitude in the spectra regions around the stop band showed a change in the location of the standing wave. This shift in the position of the nodes is predicted explicitly for fibre Bragg gratings. At the edges of the stop band standing waves with high visibility were observed, these resonances are thought to be associated with initial Fabry-Perot modes. The modes are generated by the effective index mismatch of the grating region and the waveguide region [14].

4.5 Future Work

There are several areas for continuation of this work. One of the most profitable would be the use of D-fibres to provide a better geometry, thereby allowing the electric field to be mapped along the whole length of the grating. This would also facilitate the imaging the electric field variation in more complex fibre gratings.

Future investigations could also analyse the extent of the perturbation induced by polishing by characterising the spectral response of the grating pre and post-polishing. Samples with a thinner cladding would allow the

refractive index of the modulation to be located relative to the standing waves at the edges of the stop band. Thereby directly demonstrating the relative location of the standing wave to the refractive index modulation.

A natural progression of this technique would be to investigate more advanced photonic band gap devices such as two or three-dimensional photonic crystals. At present samples are being awaited from a local company fabricating two-dimensional photonic crystals operating at near infrared frequencies. Investigating these structures would provide direct evidence of the electric fields within photonic crystals. Permitting a comparison with the theoretical models and providing feedback to the fabricators about defects in the structure.

4.6 References

[1] K. O. Hill and G. Meltz. "Fiber Bragg grating technology fundamentals and overview". *Journal of Lightwave Technology*, 15(8):1263–1276, 1997.

[2] K.O. Hill, Y Fujii, D.C. Johnson, and B.S. Kawasaki. "Photosensitivity in optical fiber waveguides:Application to reflection filter fabrication.". *Applied Physics Letters*, 37(10):647–659, 1978.

[3] G. Meltz, W. W. Morey, and W. H. Glenn. "Formation of Bragg Gratings in Optical Fibers by a Transverse Holographic Method". *Optics Letters*, 14(15):823–825, 1989.

[4] I. Bennion, J. A. R. Williams, L. Zhang, K. Sugden, and N. J. Doran. "UV-written in-fibre Bragg gratings". *Optical and Quantum Electronics*, 28(2):93–135, 1996.

[5] A. Othonos. "Fiber Bragg gratings". *Review of Scientific Instruments*, 68(12):4309–4341, 1997.

[6] N. M. Dragomir, C. Rollinson, S. A. Wade, A. J. Stevenson, S. F. Collins, G. W. Baxter, P. M. Farrell, and A. Roberts. "Nondestructive imaging of a type I optical fiber Bragg grating". *Optics Letters*, 28(10):789–791, 2003.

[7] J.D. Mills, C. W. J. Hillman, B.H. Blott, and W. S. Brocklesby. "Imaging of free space interference patterns used to manufacture fiber Bragg gratings.". *Applied Optics*, 39(33):6128–6135, 2000.

[8] J.D. Mills. *An investigation of Phase-Mask Diffraction Patterns And Fibre Bragg Gratings With Scanning Near-Field Optical Microscopy*. PhD thesis, University of Southampton, 2001.

[9] J.D. Mills, C. W. J. Hillman, W. S. Brocklesby, and B.H. Blott. "Evanescent field imaging of an optical fibre Bragg grating". *Applied Physics Letters*, 75(26):4058–4060, 1999.

[10] O. Painter, R. K. Lee, A. Scherer, A. Yariv, J. D. O'Brien, P. D. Dapkus, and I. Kim. "Two-dimensional photonic band-gap defect mode laser". *Science*, 284(5421):1819–1821, 1999.

[11] A. Mekis, J. C. Chen, I. Kurland, S. H. Fan, P. R. Villeneuve, and J. D. Joannopoulos. "High transmission through sharp bends in photonic crystal waveguides". *Physical Review Letters*, 77(18):3787–3790, 1996.

[12] J. I. Archambault, P. S. J. Russell, S. Barcelos, P. Hua, and L. Reekie. "Grating-Frustrated Coupler - a Novel Channel-Dropping Filter in Single-Mode Optical-Fiber". *Optics Letters*, 19(3):180–182, 1994.

[13] M. J. F. Digonnet, J. R. Feth, L. F. Stokes, and H. J. Shaw. "Measurement of the Core Proximity in Polished Fiber Substrates and Couplers". *Optics Letters*, 10(9):463–465, 1985.

[14] J. E. Sipe, L. Poladian, and C. M. Desterke. "Propagation through Nonuniform Grating Structures". *Journal of the Optical Society of America a-Optics Image Science and Vision*, 11(4):1307–1320, 1994.

[15] V. Mizrahi and J. E. Sipe. "Optical-Properties of Photosensitive Fiber Phase Gratings". *Journal of Lightwave Technology*, 11(10):1513–1517, 1993.

[16] T. Erdogan. "Cladding-mode resonances in short- and long-period fiber grating filters". *Journal of the Optical Society of America a-Optics Image Science and Vision*, 14(8):1760–1773, 1997.

[17] S.A. Vasil'ev, E.M. Dianov, O.I. Medvedkov, V.N. Protopopov, D.M. Costantini, A. Locco, H.G. Limberger, and R.P. Salathe. "Properties of the cladding modes of an optical fibre excited by refractive-index gratings.". *Quantum Electronics*, 29(1):65, 1999.

[18] A. Nesci, R. Dandliker, and H. P. Herzig. "Quantitative amplitude and phase measurement by use of a heterodyne scanning near-field optical microscope". *Optics Letters*, 26(4):208–210, 2001.

[19] V. Finazzi and M. N. Zervas. "Effect of periodic background loss on grating spectra". *Applied Optics*, 41(12):2240–2250, 2002.

[20] J.D. Joannopoulos, R.D. Meade, and J.N. Winn. *Photonic Crystals*. Princeton University Press, 1995.

[21] P. S. J. Russel, T. A. Birks, and F. D. Lloyd-Lucas. "Confined electrons and photons: New physics and applications". pages 603–605. Plenum, New York, 1995.

Chapter 5

Waveguide characterisation

5.1 Chapter introduction

This chapter details work relating to the characterisation of optical waveguides with the interferometric SNOM system described in chapter 3. Planar waveguides often have an air cladding, in which the evanescent field of the optical mode exists. As shown in chapter 4, access to this field permits SNOM characterisation of the optical device. The principal motivation of this work was to develop and validate a SNOM technique, capable of determining the microscopic propagation loss of an optical waveguide. The technique relies on the measurement of the standing wave generated in a waveguide. From the visibility of this standing wave, the loss between two points on a waveguide can be calculated. Previous techniques [1] allow the complete loss of the waveguide to be calculated. The technique proposed in this chapter is capable of measuring the microscopic loss such that the loss of individual events can be determined. Such a system can be applied to investigate defects or the components of an integrated optical waveguide. All the work presented is performed on channel waveguides fabricated by the established potassium ion exchange technique.

The chapter starts by surveying the conventional waveguide loss measure-

ment techniques and describes the proposed SNOM technique. Section 5.3 looks at the theory behind the technique and presents the method in which the loss can be calculated. Section 5.4 describes the experimental detail including the fabrication details of the samples. The majority of the chapter shows the results and analysis of the SNOM data, and closes with the conclusions drawn from the investigation and a detailed look at the future work.

5.2 Waveguide loss measurement

This section introduces the proposed loss measurement technique, and reviews the conventional waveguide loss measurement techniques. The section concludes by discussing the possible methods of characterising waveguide loss using SNOM and their potential advantages.

5.2.1 Conventional macroscopic loss measurement techniques

Propagation loss is characterised by the attenuation coefficient (α). The coefficient is defined as the fractional decrease in the optical power per unit distance. Thus,

$$\alpha = \frac{1}{L} \ln \left(\frac{1}{T} \right) \tag{5.1}$$

where L and T is the length and transmittance respectively of the waveguide. However for planar and channel waveguides the coefficient is usually defined in terms of decibels per centimeter (dB/cm) [2]. Hence equation 5.1 becomes:

$$\alpha_{dB} = \frac{1}{L} 10 \log \left(\frac{1}{T} \right) \tag{5.2}$$

Conversion between α and α_{dB} is shown in the following relation:

$$\alpha_{dB} = \left(\frac{10}{\ln 10} \right) \alpha \tag{5.3}$$

There are many problems associated with the accurate measurement of α in planar and channel waveguides. These principally stem from the low total losses associated with the typically short lengths associated with planar and channel waveguides. A successfully measurement technique must be able to accurately differentiate between true propagation loss and other mechanisms such as Fresnel reflections and coupling losses. Propagation loss in planar systems are typically a result of scattering, very little is due to absorbtion. The scattering is predominately caused by boundary defects and refractive index fluctuations. Again scattered light must also be discriminated in the measurement technique.

There are several existing techniques used in the measurement of waveguide loss. The cut-back method [3], the prism coupling technique [4, 5], side scattering detection [1, 6], internal modulation method [7], reflectometry [8] and Fabry-Perot methods [9]. The Fabry-Perot technique providing the most accurate measurement. The method proposed by Feuchter and Thirstrup [9] incorporates the waveguide into a Fabry-Perot cavity. The cavity consists of two polarisation maintaining fibres each with dielectric mirrors on one end, the other ends are butt coupled to ends of the waveguide. Light is coupled into the system through one of the dielectric mirrors, the transmission of the system is monitored from the other end. The fibres are stretched with a piezo-electric transducer, thus changing the length of the cavity. The transmission of the system displays Fabry-Perot fringes. With prior knowledge of the reflectivity of the dielectric mirrors, the contrast of the modulated transmission provides sufficient information to calculate the loss of the waveguide.

This method as well as most of other methods measure the loss of the complete system, giving the average loss of the waveguide. These systems do not give a position dependence of the loss nor are they able to determine the mechanism by which the field is lost. For fabrication feedback this type of information is crucial.

The following section discusses how SNOM can be applied to measure the

propagation loss of a waveguide.

5.2.2 Determining waveguide loss using a SNOM technique

As shown in the previous chapter SNOM has the capability of being able to measure the evanescent field along the optical axis of the waveguide, enabling the evolution of the propagating field to be surveyed. This section describes the methods by which SNOM can be used to determine the attenuation of a waveguide mode.

The simplest SNOM technique for measuring the propagation loss is to sample the magnitude of the evanescent field as a function of distance along the waveguide, as shown in figure 5.1. From the exponential de-

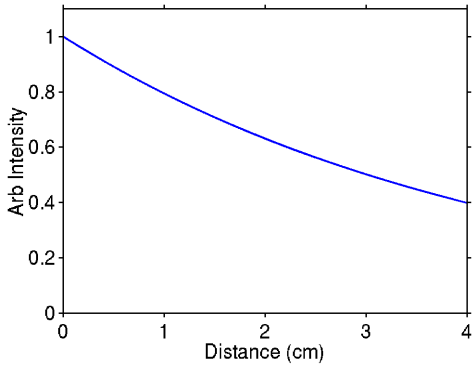

Figure 5.1: Graph showing the intensity as a function of the propagation distance along a waveguide of uniform loss. The attenuation coefficient is 1.0 dB/cm.

cay of the field amplitude along the waveguide, the loss coefficient may be calculated. However, large errors are encountered due to the artifacts discussed in sections 2.2.5.2 and 2.6. Variations in the probe/sample separation, and structure of the waveguide can induce large changes in the magnitude of the field. These artifact related problems can be reduced by

inducing a standing wave in the waveguide. This is can be easily achieved by polishing the end face to ensure the fresnel reflection is coupled back into the waveguide. The intensity of which is shown by the red line in figure 5.2(a). The counter propagating fields generate a standing wave

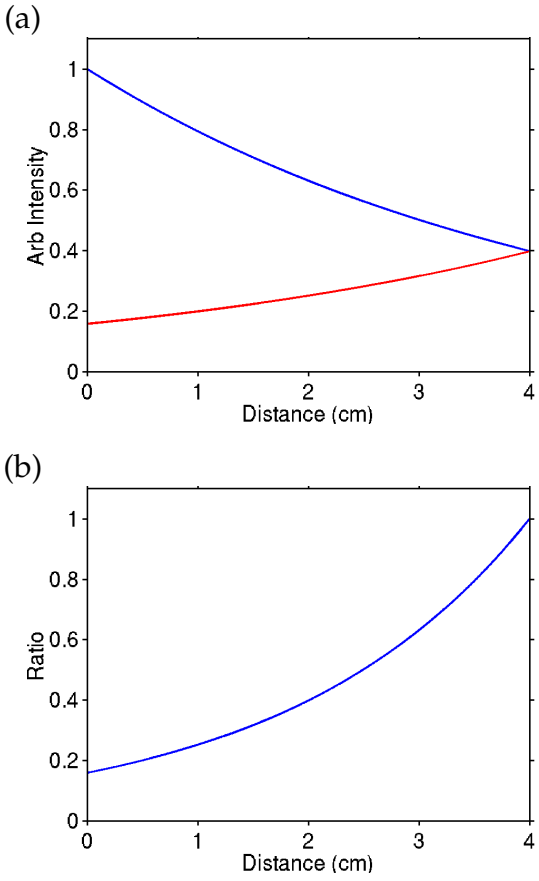

Figure 5.2: (a) Graph showing the intensity as a function of the propagation distance along a lossy waveguide. The attenuation coefficient is 1.0 dB/cm. The blue line represents the intensity of the mode launched in directly and the red line represents the intensity of a light back reflected from the end of the waveguide. The back reflection shown is 100%. (b) Plot showing the ratio (I_F/I_B) of intensities of the forward (I_F) and backward (I_B) propagating modes shown in (a).

along the waveguide. Imaging of this interference using SNOM permits the measurement of the modulation depth, from which the ratio of the amplitudes of the forward (A_f) and backward (A_b) propagating fields can be determined [10]. The ratio (A_b/A_f) is shown in figure 5.2 (b), measurement

of the ratio at two individual points enables the determination of the loss in the intervening section of the waveguide.

This method has several advantages over previous techniques, for example, it does not require prior knowledge of coupling at the end faces of the waveguide. A calibrated value of the electric field is also not required. As waveguide morphology and probe/sample separation affects both counter propagating modes by the same magnitude the ratio of the fields should be unaffected. Long term stability of the input power is also not required. However the inherent strength of this technique is its ability to measure loss in a microscopic length scale, enabling the loss of individual events to be determined.

The next section considers the system in more detail. It will highlight the method in which the loss measurement is extracted from the SNOM data and other potential experimental methods of quantifying the loss. It will also highlight the assumptions made and the requirements from the sample.

5.3 Theory

The interference generated by two counter-propagating waves has been considered in a previous section 2.3. However to acquire the attenuation coefficient it is necessary to understand the relationship between the relative amplitudes of the forward and backward propagating waves along the length of the waveguide. Figure 5.3 shows a schematic of a waveguide where P and Q represent two points on the waveguide. The position of point Q and the end facet, relative to point P are defined by the values ℓ_{Q} and ℓ_{end} respectively.

Equation 5.1 can be redefined in terms of the electric field, to express the

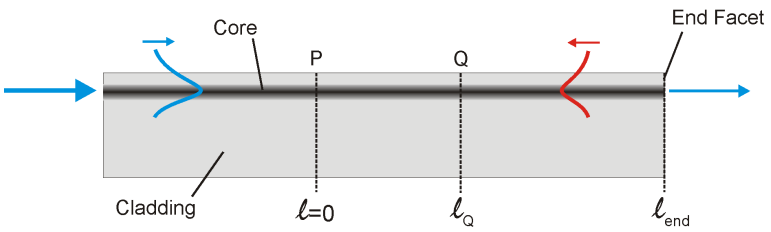

Figure 5.3: Schematic of a waveguide showing the relative positions of points P, Q and the end facet. The forward propagating mode is shown in blue and the back reflected mode is in red.

electric transmission ratio along a waveguide of length ℓ,

$$\frac{E_\ell}{E_0} = \exp\left(-\frac{1}{2}\alpha\ell\right) \tag{5.4}$$

At position P there is a forward and backward propagating field, defined by E_{PF} and E_{PB} respectively. And similarly at position Q, E_{QF} and E_{QB}. The electric fields can be described in terms of position and time as shown below,

$$\begin{aligned} E_{\mathrm{PF}} &= E_0 e^{i(\omega t)} \\ E_{\mathrm{PB}} &= E_0 e^{i(\omega t + 2k\ell_{\mathrm{end}})} e^{-\alpha\ell_{\mathrm{end}}} e^{-R} \end{aligned} \tag{5.5}$$

and

$$\begin{aligned} E_{\mathrm{QF}} &= E_0 e^{i(\omega t - k\ell_{\mathrm{Q}})} e^{-\frac{1}{2}\alpha\ell_{\mathrm{Q}}} \\ E_{\mathrm{QB}} &= E_0 e^{i[\omega t + k(2\ell_{\mathrm{end}} - \ell_{\mathrm{Q}})]} e^{-\frac{1}{2}\alpha(2\ell_{\mathrm{end}} - \ell_{\mathrm{Q}})} e^{-R} \end{aligned} \tag{5.6}$$

where E_0 is the magnitude of the electric field at point P. R is the reflectance of the end face of the waveguide, which is dependent on the fresnel reflection coefficient, the angle of the end face relative to the optical axis and the numerical aperture of the waveguide.

The ratio of the magnitude of the forward and backward propagating fields was introduced in chapter 4. It provided a convenient means to evaluate the relative magnitudes of the two fields. It was also shown that this ratio can be calculated from SNOM images. Equation 5.7 expresses

the ratio of the counter-propagating fields at the two positions, P and Q.

$$R_{\mathrm{P}} = \frac{E_{\mathrm{PB}}}{E_{\mathrm{PF}}} = e^{2ik\ell_{\mathrm{end}}} e^{-\alpha\ell_{\mathrm{end}}} e^{-R}$$
$$R_{\mathrm{Q}} = \frac{E_{\mathrm{QB}}}{E_{\mathrm{QF}}} = e^{2ik\ell_{\mathrm{end}}} e^{\alpha(\ell_{\mathrm{Q}}-\ell_{\mathrm{end}})} e^{-R} \tag{5.7}$$

Combining the ratios R_{Q} and R_{P} yields an simple relation, defining the quantity α:

$$\alpha = \frac{1}{\ell_{\mathrm{Q}}} \ln\left(\frac{R_{\mathrm{Q}}}{R_{\mathrm{P}}}\right) \tag{5.8}$$

Application of equation 5.3 to the previous relation, yields an expression for the attenuation in units of decibels.

$$\alpha_{dB} = \frac{10}{\ell_{\mathrm{Q}}} \log\frac{R_{\mathrm{Q}}}{R_{\mathrm{P}}} \tag{5.9}$$

This shows that the loss of the waveguide can be directly calculated from the values of R_{Q} and R_{P} and is independent of the reflection coefficient. It should also be noted that losses incurred between point Q and the end of the waveguide can be incorporated into the reflection coefficient. And thus the waveguide is independent of any losses other than that between points P and Q. In a situation where the loss of an individual event is characterised, the term ℓ_{Q} has no relevance and can therefore be made equal to unity.

Section 2.3.1 introduced a technique to measure the relative amplitude of the counter-propagating components. The method measures the visibility of the standing wave from which the relative amplitudes can be determined. The system previously implemented required scanning of the probe to determine the contrast. Recalling equation 2.22 which describes the standing wave generated at the surface of the waveguide, it presents three potential scanning methods to calculate the visibility. In order to measure the visibility it is necessary to measure the intensity or electric field when the term $\cos(2kx + \gamma)$ is at its limits. The technique shown in section 2.3.1 varies the value of x by scanning the tip along the surface. Visibility measurements can also be achieved with a stationary tip. In this situation γ or k can be varied, γ being the phase difference between the

forward and backward propagating components. This is realised by the probe sampling the electric field at a point on the waveguide, the visibility can be measured by changing the optical path length of the back propagating component independently to that of the forward propagating component. This can be achieved by coupling a second waveguide such as a fibre onto the end facet of the waveguide. Stretching or heating of the fibre changes the path length. A schematic of a proposed system is shown in figure 5.4. It is important that the back reflection from the couple between the waveguide and fibre is minimised. This can be achieved using careful mode matching between the waveguide and the fibre, refractive index matching oil and angle polished end faces.

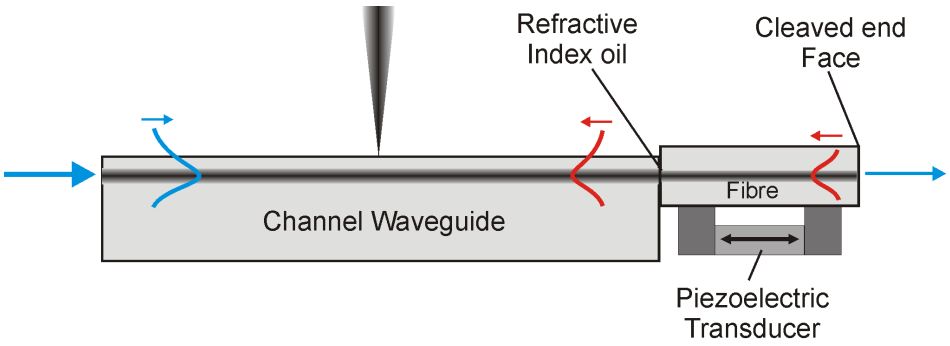

Figure 5.4: An alternative technique to measure the visibility of the standing waveguide generated in a waveguide. The piezoelectric transducer varies the length of the fibre and hence changes the optical path length of the light back reflected from the end face of the fibre.

The final potential method involves the modulation of the wave vector k of the field. This can be directly achieved by scanning the frequency of the field. Commercial diode lasers present an easy method of frequency modulation with tens of MHz accuracy. The experimental arrangement is similar to that previously described where the probe is kept stationary, however in this case the frequency of the laser is perturbed. The two later configurations have the distinct advantage of not having associated SNOM scanning artifacts. However they still require the tip to maintain a close proximity with the surface to sample the evanescence field. This

thesis focuses on two of the proposed techniques, the x and k modulation. γ modulation has not been implemented due to additional mechanical stability and additional sample preparation to reduce back reflections between the modulating fibre and waveguide. The γ technique however has the advantage in that the end cleave of the modulation fibre can be coated to increase the back reflected light. This assists in the measurement of the standing wave.

5.4 Experimental detail

This section describes the experimental techniques for the evaluation of the methods proposed in the preceding section. It begins by specifying the experimental technique and setup of the SNOM system. It then outlines the required sample properties and in doing so defines many of the systems limitations. This is continued by describing the waveguide samples selected for this investigation. This section is concluded with the experimental results and analysis.

5.4.1 Experimental technique

The experimental arrangement and procedure is similar to that used in chapter 4. An additional one dimensional stage in the y direction is included to facilitate optical coupling into different waveguides. To permit accurate placement of the probe on the surface of the waveguide a Melles Griot Nanomax-HS 3 axis piezo stage with integrated stepper motors was utilised. The stepper motors permit 4.5 mm of travel in the x-y direction with a specified 25 nm resolution allowing large areas to be analysed without disturbing the system. The piezo stage had 20μm $\times$ 20μm of travel [11]. The loss measurements were performed at 1550nm if not otherwise stated. The 633nm light from a HeNe laser was necessary to highlight the waveguide, a microscope was then used to place the SNOM

probe in proximity with the waveguide. In this investigation it was necessary to use coated SNOM probes, the reasons for which are highlighted in section 5.5.1.

5.4.2 Sample prerequisites

The most obvious requirement for the sample is the accessibility of the evanescent field. With the exception of deep buried waveguides, the evanescent field of planar and channel waveguides is accessible without additional preparation, making the process truly non-destructive. In order for the system described to work correctly, several assumptions about the samples have been made. The back reflected light is assumed to be stable and that cavity resonances in the sample do not occur. The back reflected light is also expected to counter-propagate in the same mode as that of forward propagating mode. In a situation where a standing wave is generated from different modes, evaluation of the modal overlap is required in order to determine the relative amplitude of the components. The latter condition can be fulfilled by ensuring the waveguide is single mode at the investigating wavelength.

It is further assumed that the waveguide possess sufficient birefringence perpendicular to the surface of the waveguide that a transverse electric (TE) or transverse magnetic (TM) mode does not exchange energy into the opposing mode. This prevents several adverse effects, the most significant being the reduction of the visibility of the standing wave due to the reduction in the polarisation cross section. Other effects arise from the collection mechanism of the SNOM probe which will be discussed in more detail later.

Another sample proviso is the surface quality of the waveguide. A rough surface not only produces topographical artifacts, but also generates scattered light. Scattered light is inevitable when investigating a lossy system, however the amount of stray light due to poor input/output cou-

pling must be keep minimal to reduce noise on the measurements. Other sources of scattered light are boundary defects, Rayleigh scattering and imperfections at the end face of the waveguide, the latter being the most significant. Good polishing or cleaving of the sample is required to reduce these effects, as well as frequent cleaning to remove dust. In summary the waveguide required to validate this technique should have the following prerequisite conditions; single mode operation at the investigation wavelength; low loss; minimal surface defects and negligible birefringence. The next section describes the sample used in this investigation which fulfils these requirements.

5.4.3 Waveguide samples

Channel waveguides were selected in preference to planar waveguides due to the higher optical density. One of the most established techniques for channel waveguide fabrication is the ion exchange process [12]. The maturity of the technique means that the fabrication parameters are well understand and thus generates reproducible single mode channel waveguides [13]. The nature of the fabrication process also ensures that the waveguides have low surface defects. The refractive index change is produced by the exchange of ions in a glass or crystal with ions in a molten salt. In most situations, sodium ions in the substrate are exchanged for a cation such as K^+, Cs^+, Rb^+, Li^+, Ag^+ or Tl^+. Potassium is easily incorporated in glass, but has a low diffusion rate and a smaller refractive index change. These properties make it suitable for single mode waveguides. The index change involved in the ion exchange process is isotropic, thus the effective refractive index of the propagating modes are only dependent on the structure of the waveguide. The orientation and symmetry of the index profile ensures polarisation maintenance of TE and TM modes. However the diffusion process can induce stress due to the exchange of two cations of different ionic radii, at temperatures below the stress relaxation temperature of the glass. In potassium ion exchange waveguides

this effect is observed to produce birefringent waveguides [14]. Work by Jackel *et al.* [15] has also experimentally shown that the depolarisation due to defects is less than 1% for well fabricated waveguides. The absorptive losses associated with these waveguides is extremely low and the primary loss mechanism is radiative and originates from fabrication defects.

5.4.3.1 Waveguide fabrication

The waveguides used in this investigation were fabricated for another project by Chao-Yi Tai, a brief description of the fabrication is given for completeness. A Pyrex substrate (50mm x 50mm x 1.5mm) is successively cleaned in an ultrasonic bath of acetone, iso-propanol and deionized water each for 20 minutes. A 250nm aluminium layer is then deposited onto the substrate and a layer of Microposit S1813 photoresist is spun coated on top. Using a photolithography technique the resist is selectly removed to produce a series of $1\mu\mathrm{m}$ to $9\mu\mathrm{m}$ wide grooves with a $1\mu\mathrm{m}$ increment in width. An aluminium etch ($\mathrm{H_3PO_4}$) is used to remove the aluminium exposed by the gaps in the photoresist. The remaining photoresist is then dissolved with a suitable solvent to leave the Pyrex substrate with the remaining aluminium mask. The removed aluminium strips specify the size and position of the waveguides. The sample is then placed in a furnace with a Pyrex dish containing $\mathrm{KNO_3}$ crystals and is heated to $400^{\circ}\mathrm{C}$. Once the temperature has stabilized, the sample is placed in the melt for 11 hours. Upon removal from the melt the samples are allowed to cool to room temperature. The cleaning of the samples involves rinsing off the bulk of the melt with water and then placing them in an ultrasonic bath of deionized water. The aluminium mask is removed with the aluminium etch, and again cleaned with acetone, iso-propanol and deionized water in an ultrasonic bath. The sample is then cut and the end faces polished. The final length of the sample is $\approx$40mm. The final sample contains several groups of waveguides, each group comprises of 9 waveguides varying in width. This replication allows for redundancy in the manufacture process.

The exchange process described here is based on work by Gorytch [16], in which the refractive index change at the surface of the waveguide is measured to be 0.0073 $\pm$0.0004. Using a white light spectra it was confirmed that the 1 to 5μm waveguides have a single mode cutoff below 1550nm. Far field mode profiles of all the modes can be seen in figure 5.5. The profiles were imaged using a $\times 20$ objective and a infrared sensitive CCD camera. The TE and TM modes are shown in (a) and (b) respectively and the width of the waveguides decreasing from 9μm to 1μm going down the page. It is clear from mode profiles that the 1μm waveguide does not guide at 1550nm and the 2μm is very lossy. As a result most of the work presented investigates the 3, 4 and 5μm waveguides. The figure also shows a defect at the end face of the 3μm waveguide, consequently this particular waveguide was not used during the investigation.

An atomic force microscope (AFM) image of a 4μm waveguide is presented in figure 5.6. Figure 5.6(a) is a 3D image of the topography, showing a raised strip where the waveguide is present. The dimensions of which are clearly seen in the cross-section shown in figure 5.6(b). The raised strip is generated by the exchange of smaller sodium ions (radius=0.102 nm) for the larger potassium ions (radius=0.138 nm) [17].

5.5 Results and analysis

This section presents some of the results obtained from investigating the loss of the previously described waveguides using the SNOM technique. Figure 5.7 introduces a typical waveguide scan of a 4 μm waveguide. The image in (a) shows a false colour plot of the topography of a 4μm wide waveguide, the waveguide is again defined by the raised section horizontal to the page. Light is launched in from the right side of the image and back reflected by the polished end face of the waveguide, this is the convention used in this chapter. The guided light has TM polarisation and a wavelength of 1550nm. (b) and (c) displays the corresponding false color

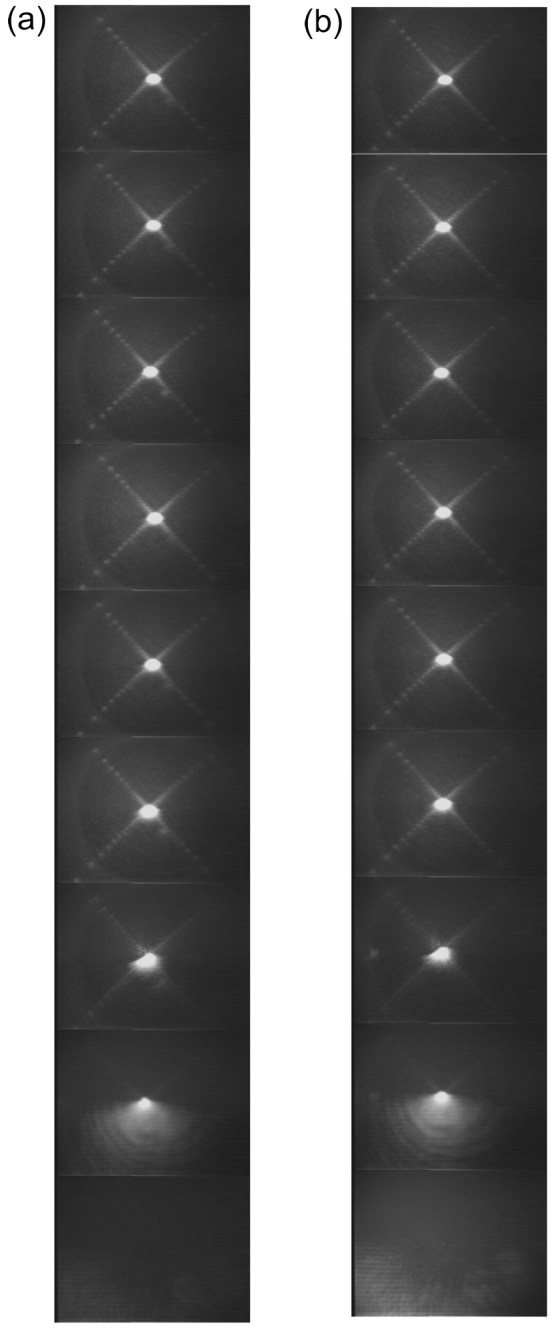

Figure 5.5: Figure showing the mode profiles of the waveguide (a) corresponds to TE modes and (b) TM modes. The width of the waveguide changes from 9μm to 1μm top to bottom with a 1μm increment. The intensity of the mode profiles are not normalised.

(a)

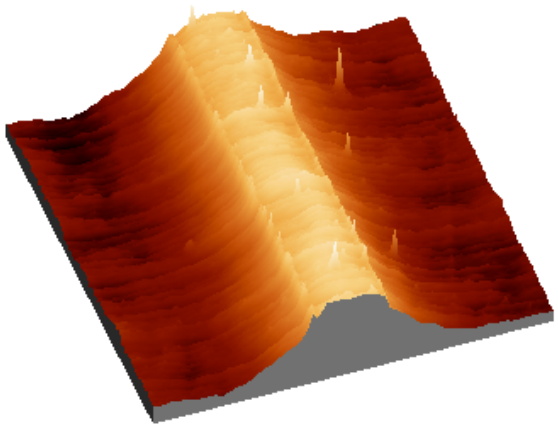

(b)

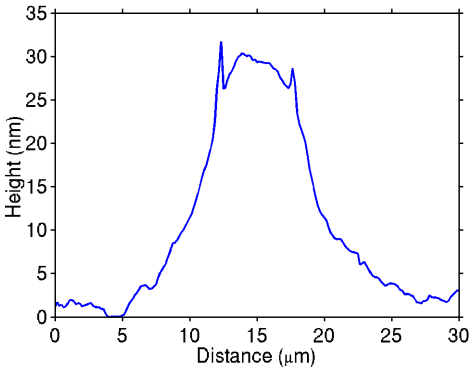

Figure 5.6: (a) A 3D AFM image 30μm by 30μm of a 4μm potassium ion exchange waveguide. (b) A cross section of (a) showing the topographical profile of the waveguide.

image of the electric field magnitude and phase of the interference pattern. As in the previous chapter the electric field images have an absolute scale if not otherwise stated. Here the electric field is seen to oscillate along the axis of the waveguide at a period of $\lambda/2n_{eff}$, where λ is the wavelength in free space and n_{eff} is the effective refractive index of the mode. The phase is seen to oscillate a half the frequency of the electric field magnitude. The cosine of the phase is shown in figure 5.7(d). The images display a slight tilt, the is a result of a linear distortion in the piezo stage described in section 3.1.3.

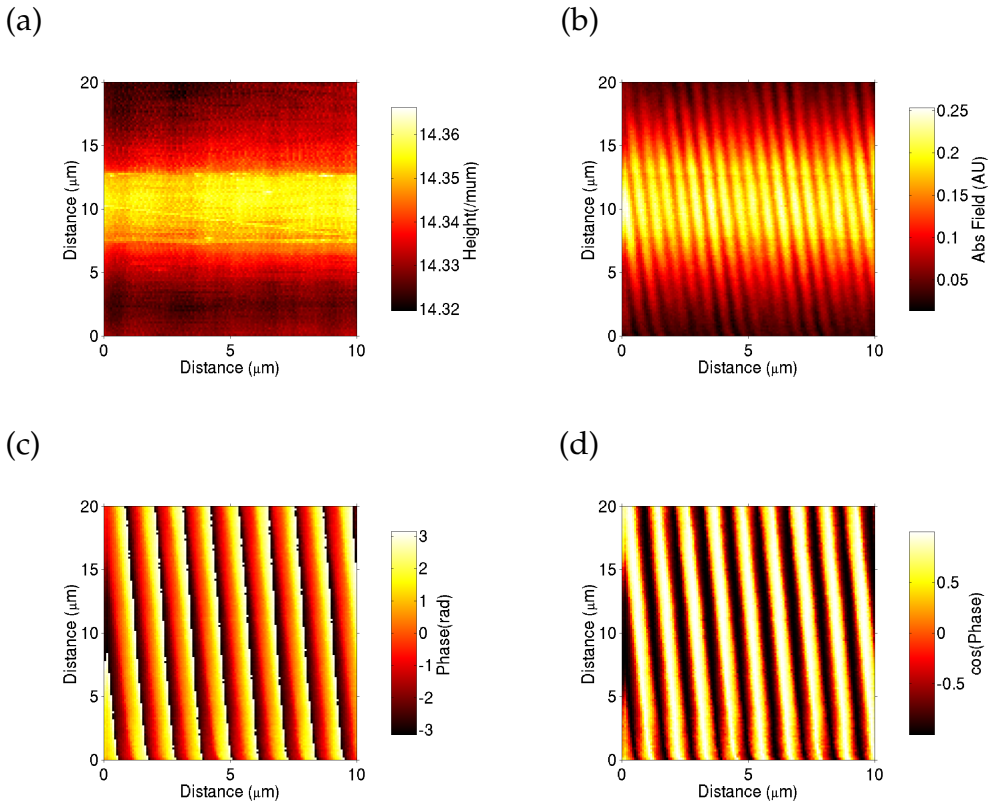

Figure 5.7: SNOM data of a 4 μm waveguide. (a) shows a false colour image of the topography of the surface of the waveguide. (b) and (c) images of the electric field magnitude and phase. (d) shows the cosine of the phase.

The cross sections in figure 5.8 along the axis of the waveguide demonstrate the variation of the optical amplitude and phase. Experimental data

is represented by the red circles and the blue line shows a fit from the expressions in section 2.3. The values of the parameters is given in the figure caption. The value for the effective refractive index is lower than expected for this waveguide, this is due to the uncertainty in the calibration of the piezo stage, see section 3.2.4.

(a)

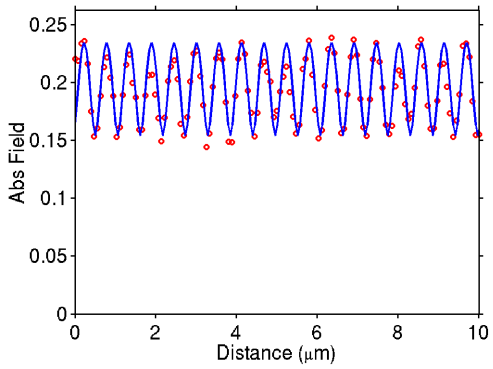

(b)

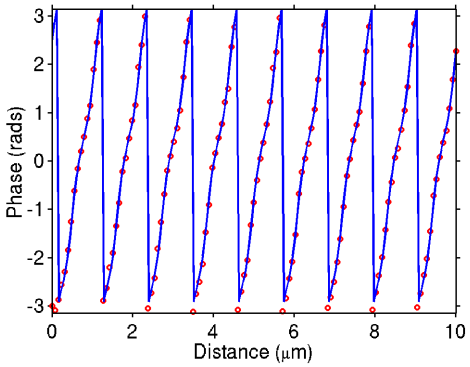

Figure 5.8: Cross section along the optical axis of the waveguide shown in figure 5.7. (a) and (b) display the electric field magnitude and phase as a function of distance along the waveguide. Experimental data is shown by red circles and a fit is shown by the blue line. The parameters of the fit are $A_f = 0.195$, $A_b = 0.042$, $\gamma = 0.44$rad and $n_{eff} = 1.40$.

In figure 5.7(a) two fine ridges at the edges of the raised section of the waveguide can be observed. The features are relics of the diffusion aperture and have also been observed by Blaize *et al.* [18]. The ridges are also visible in the AFM scan shown in figure 5.6. Careful examination of the electric field image reveals similar features to that seen in the topographical data. The raised topographical feature corresponds to a reduction in the electric field magnitude, illustrating the effect of topographical artifacts presented in section 2.2.5.2. It also exemplifies the need for waveguide samples with low topographical features. As in chapter 4 the combination of the phase and electric field magnitude yields the true electric field, shown in figure 5.9.

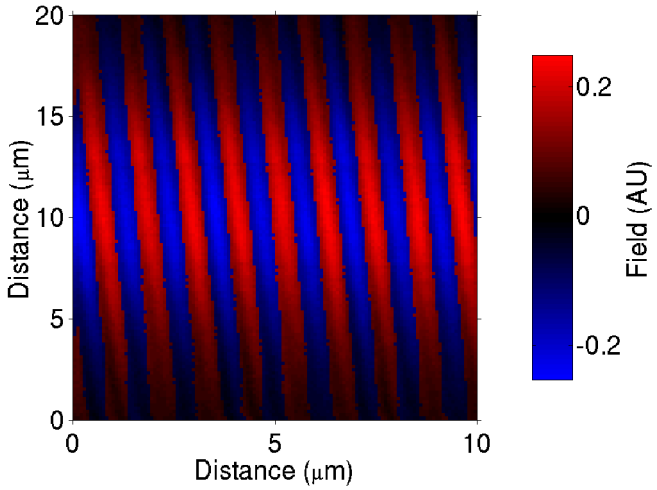

Figure 5.9: A false colour image showing the real electric field of a standing wave in a waveguide, note the negative scale of the colour bar. The figure is an alternative method of presenting the data in figure 5.7.

Finally figure 5.10 presents the electric field magnitude and phase in the vertical plane above the surface. It illustrates the exponential nature of the decay of the evanescent field. The phase of the electric field is slightly distorted, due to the long acquisition time of 75 minutes. The black region at the bottom of the scans defines the surface, the gradient of which was caused by a 2 degree tilt of the sample relative to the x axis. To highlight

the low magnitude propagating fields above the surface of the waveguide a logarithmic plot of the electric field is shown in (c). A cross section of the field magnitude is shown in (d). The plot has a logarithmic scale and thus the linear nature of the plot demonstrates the exponential decay of the evanescent field.

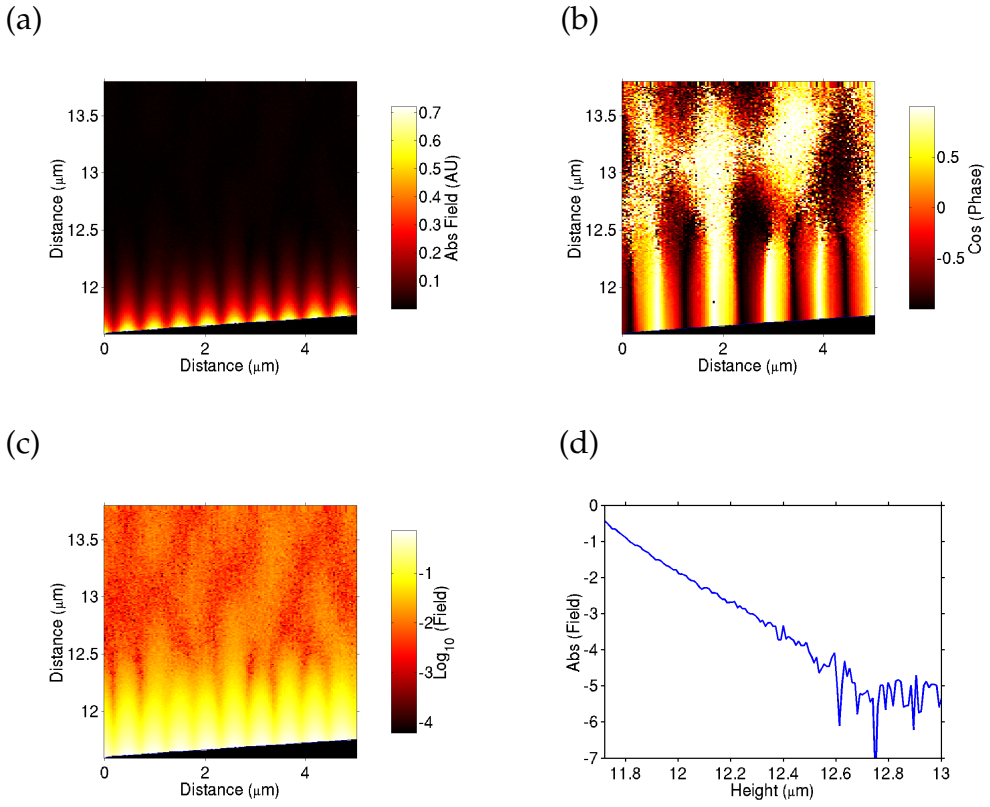

Figure 5.10: Images showing the complex electric field in the xz plane above the optical axis of the waveguide. (a) shows the electric field magnitude and (b) shows the phase evolution. (c) presents the electric field data with a logarithmic scale. (d) a cross section of (a) showing the logarithm of the electric field magnitude as a function of distance away from the surface.

5.5.1 The sources and effects of scattered light

The electric field fluctuations seen in figure 5.7 (a) which are not associated with the standing wave are generated by the combined effect of to-

pographical artifacts and scattered light. The mechanisms for producing scattered light are the same as those responsible for waveguide loss. The two principal sources for scattered light are the input and output facets of the waveguide, and surface defects. On the end faces of the waveguide, scattering occurs from polishing imperfections and fresnel reflections that are not coupled back into the waveguide. Figure 5.11 shows the electric field magnitude at 0.5mm intervals from the end face of the waveguide. Near the end face a beating is observed with a period of approximately 3μm. The beating decreases with distance away from the end face, at a distance of 2.5mm the beating is almost undetectable. Figure 5.12(a) shows a larger scale image of the intensity close to the end of the waveguide. It clearly shows the additional longer period oscillation. From the cross section shown in (b) the period of the beating is measured to be 3.18 $\pm$ 0.05μm, the large error again comes from the uncertainty in the calibration of the stage (3.2.4). This period corresponds to the beating between two optical fields with a effective refractive index difference of 0.487 $\pm$ 0.008. This corroborates the origin of the beating as the consequence of the interference between scattered light from the end face ($\mathrm{n_{air}} = 1.0$) and the mode propagating in the waveguide ($n_{\mathrm{eff}} \approx 1.48$, see section 5.5.2).

The other main source of scattered light occurs from defects at the surface of the waveguide. Nanometer features have been shown to play a dominant part of the loss mechanism in certain waveguides [19]. Figure 5.7 has already introduced the effect of such defects, however the quantity of the scattered light was relatively small. The following discussion presents some data investigating larger defects. Figure 5.13 shows a scan along the surface of a 4μm waveguide, the topography shows a couple of defects, the largest of which is approximately 40 nm height and several hundred nanometers in diameter. The corresponding electric field magnitude and phase data is shown in figure 5.13 (b) and (c). The mode propagating through the waveguide is visible in the electric field data by the horizontal modulation. This is enhanced by interference between the evanescent

(a)

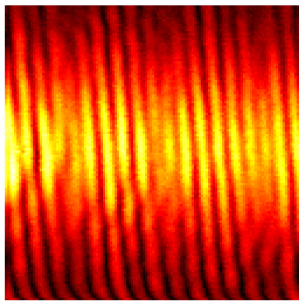

(b)

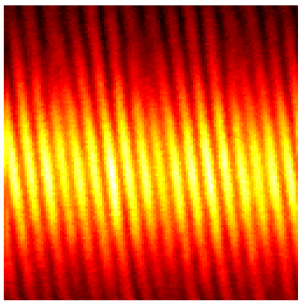

(c)

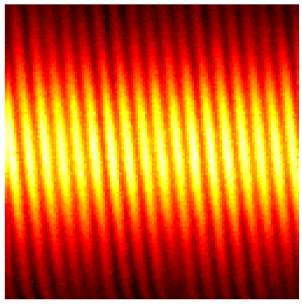

(d)

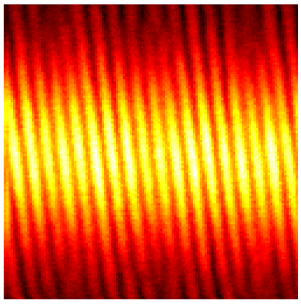

(e)

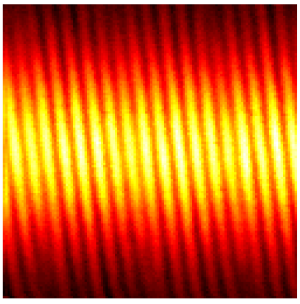

Figure 5.11: A series of images showing the evolution of the electric field magnitude as a function of distance from the end face of a 3μm waveguide with a TM mode. (a) is acquired 0.5mm away from the end, and the other images are acquired at 0.5mm intervals in alphabetical order. The images dimensions are 10μm horizontally and 20μm vertically.

(a)

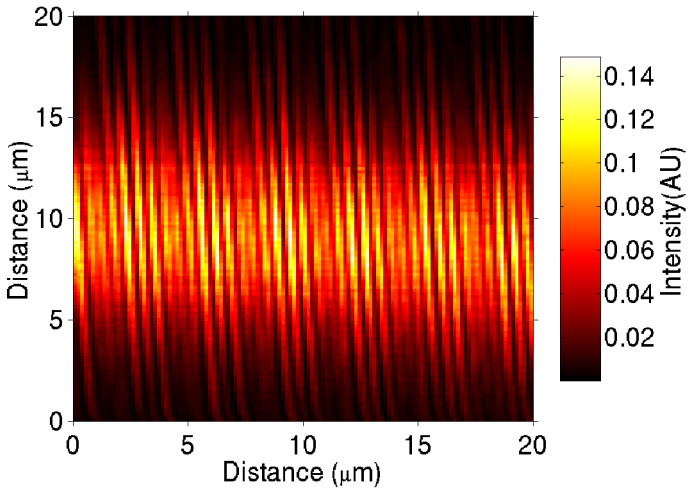

(b)

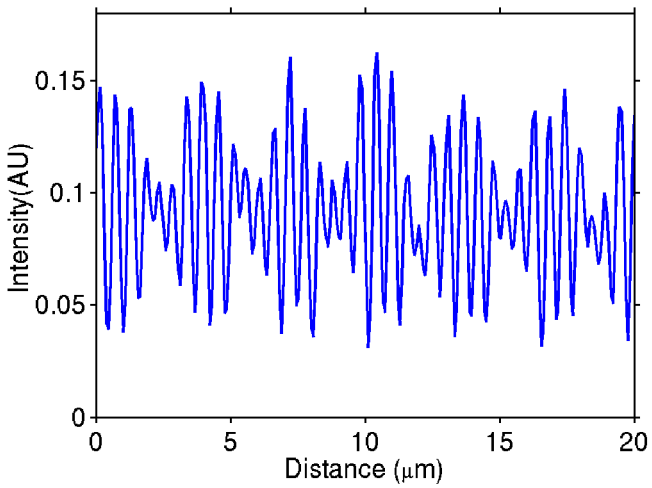

Figure 5.12: (a) Image of the intensity near the end face of a 3μm waveguide. The mode has TM orientation. (b) A plot of intensity as a function of distance along the waveguide, clearly showing the beating with a period of $3.18 \pm 0.05\mu$m.

field generated by the guided mode and free space scattered light. The large ring structure seen in (b) is thought to be generated by the finite size of the scattering defect. The ring structure in the phase approximates that expected from a point source defect.

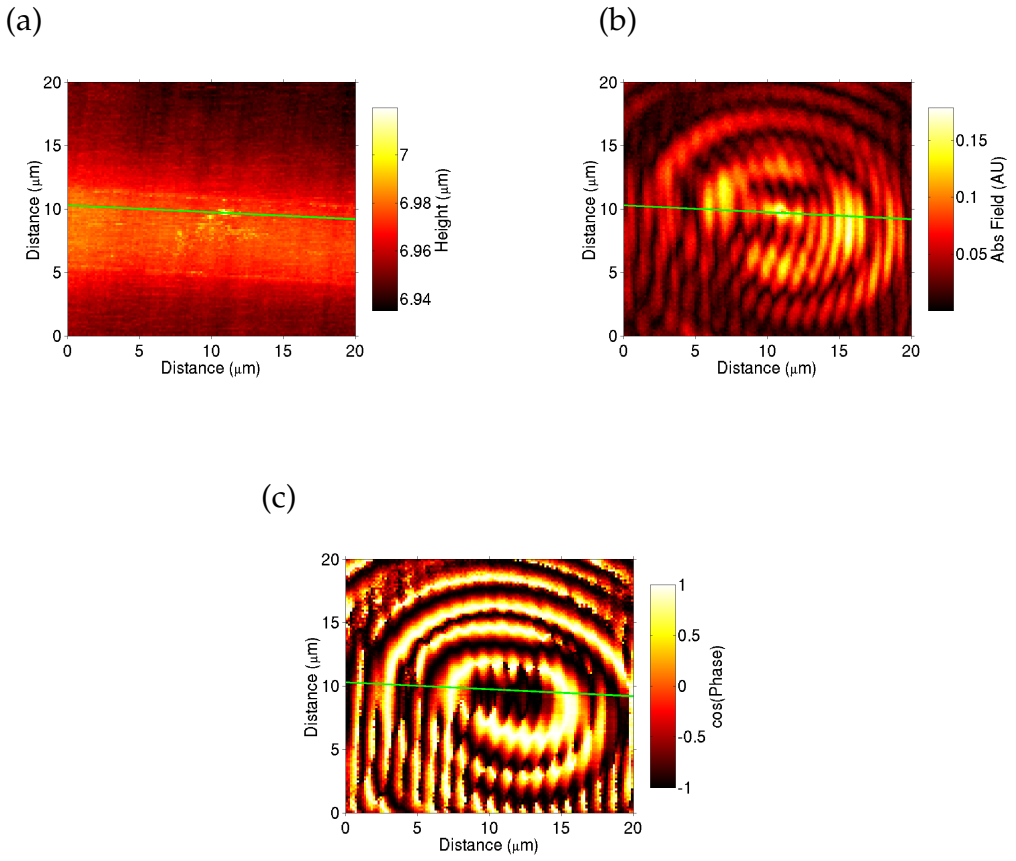

Figure 5.13: The electric field around a surface defect on a 4μm waveguide. (a) Shows the topographical image of the surface showing a complex defect. (b) and (c) Shows the electric field magnitude and phase, about the defect.

Figure 5.14 is a vertical scan, showing a cross section of the electric field in the xz plane. The green lines in figure 5.13 shows the point at which it intersects. The field image shows that the ring like structure has a large propagating field component. The slight modulation in the z direction is generated by cross coupling between the field phase and magnitude. The

cross coupling is the result of a slight bias in the magnitude of the X and Y outputs.

(a)

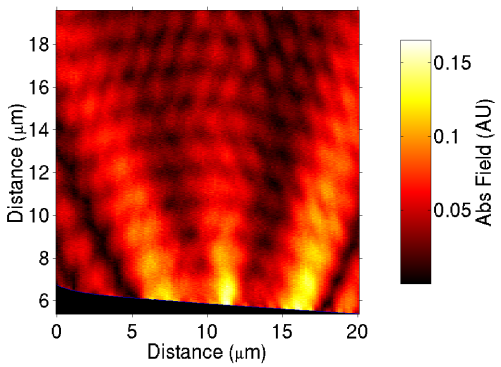

(b)

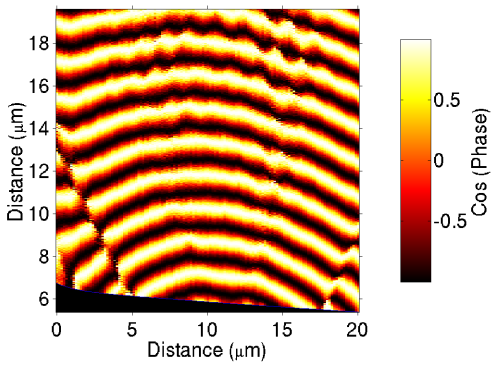

Figure 5.14: Images showing the complex electric field in the xz plane above the defect shown in the figure 5.13. (a) Shows the electric field magnitude and (b) shows the phase evolution.

To fully understand the structure of the interference, a theoretical model of the system is required. This requires an exact knowledge of the defects shape, composition and position. Much of this information can be acquired using SPM techniques, however such an analysis is not of interest in this investigation.

To reduce the amount of collected scattered light a large amount of effort was put into improving the quality of the SNOM probes using the techniques described in the section 3.1.1. For completeness figure 5.15 shows an image of the electric field magnitude of a waveguide without an aluminium coating. The image shows the effect of scattered light coupling through the side walls of the fibre probe.

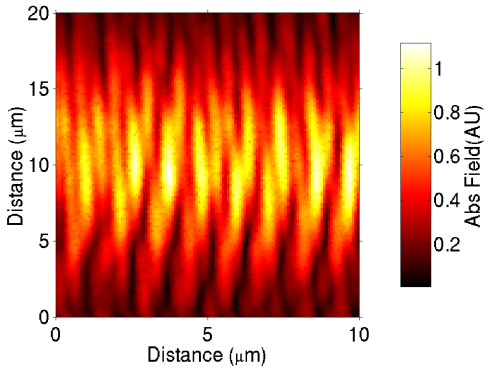

Figure 5.15: A false colour image of the electric field magnitude above a waveguide. The fibre probe was un-aluminised.

5.5.2 Characterisation of the propagation constant

Another feature of this SNOM system is the ability to measure the propagation constant of the optical mode. The spatial period of the phase gives information about the propagation constant (β) of the optical mode [20]. In this system where a standing wave is generated, the propagation constant can also be deduced from the period of the electric field amplitude. However the phase measurement from the detection system has much lower noise than the electric field magnitude [21]. Quick scans along the axis of waveguide provide the most accurate method of acquiring the data. Error in the measurement arises from the calibration of the stage, thus to minimise this error calibration of the piezo stage was completed immediately after the data was the collected. Precise calibration can be achieved using

free space detection of a plane wave with the SNOM tip or the measurement of the topography of a sample with a known period.

A convenient method of defining the propagation constant is using the effective refractive index of the mode, the relation linking this is seen in equation 2.40. Using this method the effective refractive index of the TE and TM modes of a 5μm waveguide was found to be 1.480 $\pm$ 0.011. Calibration was achieved using a 1.136 μm period phase mask and the error of the measurement derives from the accuracy of this calibration. Unfortunately a value for the refractive index of Pyrex at 1550 nm for comparison was not available from the literature. However the refractive index of Pyrex at 633 nm is given to be 1.474 [16]. Taking this value and accounting for dispersion shows that the measured value of the n_{eff} is far too high. Error in this result is expected to derive from environmentally induced phase drift.

5.5.3 The effects of the amplitude coupling function

The amplitude coupling function defines the collection efficiency of the probe. The concept derives from the optical transfer function (OTF), normally associated with far-field imaging. Typically in PSTM systems the electric field at the tip is naively considered to be directly proportional to the electric field at the photo detector. However when acquiring quantitative information the notion of an OTF must be considered. The OTF relates the electric field at the image plane with that at the object plane and therefore presents a solution to the inverse problem. Generally in SNOM the OTF is extremely complex due to the multiple scattering in the probe-sample system which breaks spatial invariance [22]. Thus in general it is impossible to apply the concept of an OTF. However the probe sample interaction has been shown to be negligible in PSTM systems with dielectric samples [23] and so applying the single scattering approximation permits the use of an OTF to describe the PSTM system.

The follow section describes a simplified interpretation of the OTF which provides a valuable insight into the image formation. A complete explanation of the image formation in the near-field can be found elsewhere [22]. It may be worth noting at this point that the concept of an OTF for SNOM has been questioned due to the supposition that there exists an object plane in SNOM [24]. However this concern originates from the influence of artifacts and as a result a nonuniform object plane. As the samples investigated approximate a flat plane, the concern is not applicable here.

The system proposed by Bozhevolnyi *et al.* [25] introduces an amplitude coupling function (ACF) that relates the near-field electric field $E(x, y, z)$ to a mode excited in the fibre probe. This function would include effects such as the depolarisation at the tip. As the work presented in this thesis employs a single mode fibre probe and thus the ACF many be represented by its simplest form of $F_{\mathrm{ij}}(k)$, where $\mathrm{i} = 1, 2$ defines the polarisation of the excited fibre mode, and $\mathrm{j} = 1, 2, 3$ corresponds to the component of the detected electric field $E(x, y, z)$. This means the ACF consists of 6 independent functions. To define the complete function for a particular system a comprehensive characterisation would be required, a task which is almost certainly impossible. However by applying the following arguments the ACF may be simplified; the probe is fabricated out of single mode fibre; the fibre probe is symmetrical about the optical axis and is normal to the surface plane and the incident field is polarised parallel to the surface plane. Employing these assumptions, the ACF for two counter-propagating fields is identical and thus ensures the measured visibility is authentic.

However this assumes the tip can be approximated by a single source, generating a single propagating mode in the collection fibre. In reality the tip is finite and is approximately 50 to 100 nm in diameter. Ideally the tip is also symmetrical, however this is not necessarily the case. The effect of the non-ideal features of the SNOM probes on the visibility of a standing wave has been investigated using a very simple model [26]. The probe is

modelled by two small spherical scatterers, where the separation and relative angle defines the tip diameter and the asymmetry. It was shown that the average power and visibility of the imaged standing wave changes significantly with separation and angle with respect to the surface. To acquire a true value for the visibility of the standing wave the tip must be symmetrical and have an aperture much smaller than the standing wave feature.

Another effect on the visibility measurement is the birefringence of the collection fibre. Birefringence in standard single mode fibre is the result of imperfections in the fibre, the most significant source is stress induced refractive index change. This is principally produced from bend and twist in the fibre. The birefringence changes the relative orientation of the polarisation of the modes. Recalling that the polarisation overlap defines the magnitude of the interference, it becomes apparent that the magnitude of the birefringence defines the visibility of the interference. Assuming the SNOM system is imperfect and thus two modes are coupled into the collecting fibre, maximum visibility will only occur when the two modes have the identical polarisation state at the fibre output. In addition the detection system requires the modes from the tip to interfere with the reference signal of the interferometer. Therefore the detected magnitude of each mode from the SNOM tip becomes a function of the relative polarisation between the mode generated by the tip and the mode of the heterodyne reference. As a result any interference system employing birefringent components can not used to determine the absolute visibility [27].

However, the requirements previously discussed are necessary for a system measuring the absolute value of the visibility of a standing wave. For the investigation undertaken here only the relative contrast between several points on a waveguide is required. By ensuring the system is stable between consecutive measurements, accurate determination of the visibility should be possible. Even so, a substantial effort was made to ensure the SNOM probes were of the highest standard, to reduce the number of

excited modes. The next section presents the measurements made to determine the microscopic loss of a waveguide.

5.5.4 Measuring the microscopic loss of a waveguide

This section investigates the microscopic loss of a waveguide using the two methods described in section 5.3.

5.5.4.1 Position modulation

Figure 5.16 shows the electric field and topographical data from a 100μm by 20μm section of a 5μm waveguide illuminated with a TE mode. The images are a composition of five successive 20μm x 20μm scans, the acquisition time for each scan was 22 minutes. Using the convention in this thesis, the forward propagating light travels from right to left across the page. Approximately half way along the scan is a small surface defect, which represents the microscopic loss under investigation. It is directly visible on the topographical data and is believed to be a fabrication relic. The first $20 \times 20\mu$m scan of the topography shows a slight drift due to thermal stabilisation of the stage. The electric field phase displays the familiar concentric rings associated with surface defects. The blue line in figure 5.16(d) shows the calculated ratio (A_b/A_f) from the data shown in (a), a value for (A_b/A_f) was acquired every 10μm along the optical axis.

At the position associated with defect there is a rapid increase in the value of the ratio, this is due to the topographical related artifacts of the surface defect, and may be disregarded. The average ratio of remaining points is 0.172. Assuming the reflection coefficient is approximately equal to the Fresnel reflection coefficient the average optical attenuation from between the position of the SNOM probe and the end facet may be calculated. The average ratio yields a waveguide loss of 0.40 dB/cm. Despite the non-ideal nature of the technique to measure the absolute ratio the value agrees

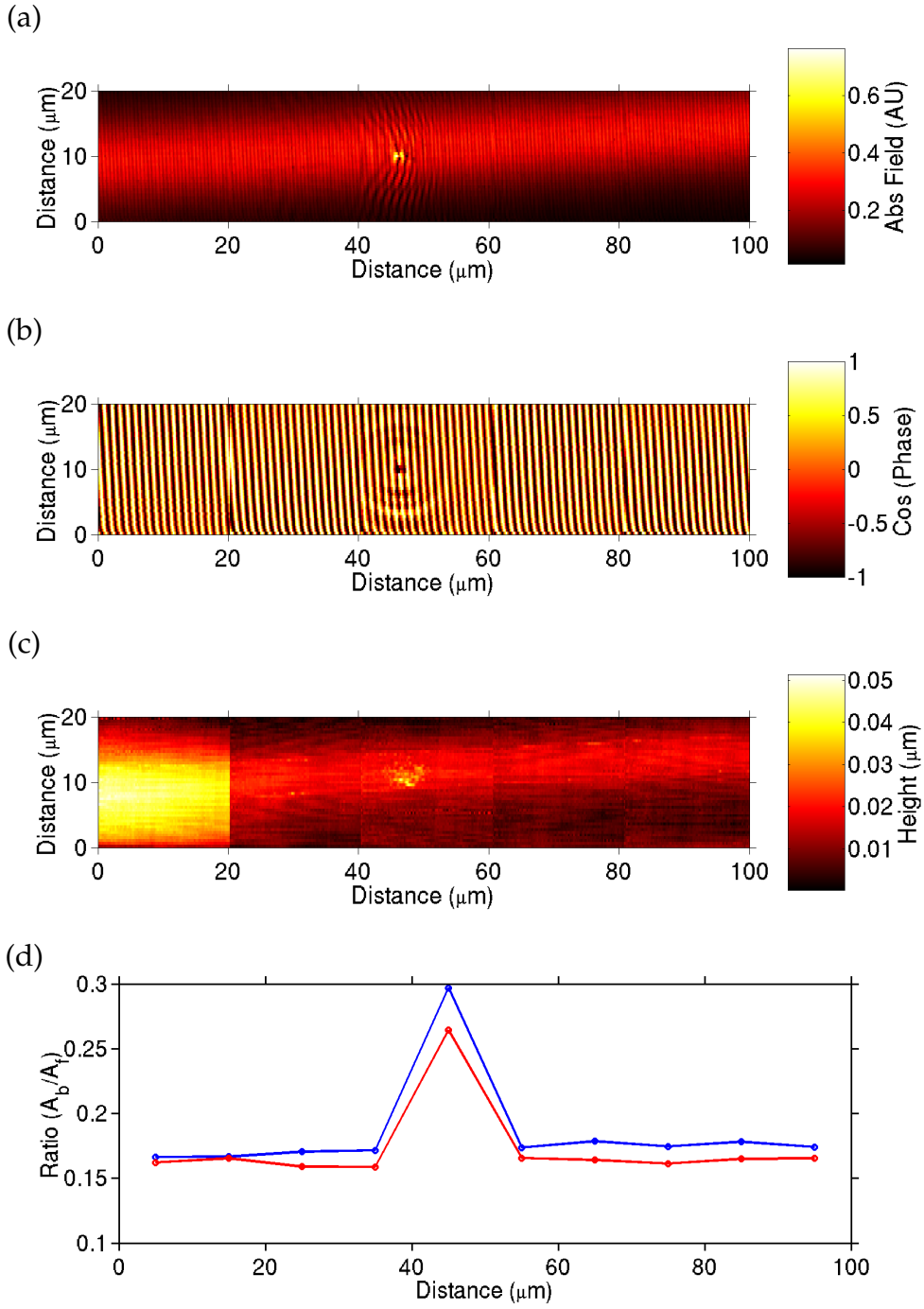

Figure 5.16: (a),(b) and (c) are the field magnitude, phase and topographical data of a 100μm by 20μm section of a 5μm waveguide with TE illumination. (d) shows the visibility ratio (A_b/A_f) as a function of distance along the waveguide.

with the loss expected from such a waveguide [13]. Further inspection in figure 5.16(d) shows an change in the ratio on either side of the defect, the average change is 4.2%. Assuming the defect is the only source of loss in this section of the waveguide the loss of the defect is 0.18 dB. For an individual defect is value is very high. However the red line in figure 5.16(d) shows the ratio of a previous identical scan and proves there is an increase in the ratio as a function of time. The drift is expected to be originate from two processes, change in the birefringence of the collection fibre and slow wear of the SNOM tip.

To observe the temporal dependence of the ratio drift, 48 scans were taken at 12 minute intervals at the same position, showing the evolution over a 10 hour period. The concatenated data is shown in figure 5.17. The sample is seen to drift by approximately 1μm in the y direction. The ratio is seen to drift by 27% in the 10 hour period. Similar scans with less frequent acquisition of the data, suggests that the dominant mechanism is the change in the birefringence of the fibre. This is also consistent with the topographical information shown in figure 5.17 (b), which shows no signs of significant tip deformation or debris from a damaged tip on the sample surface. However this evidence is not conclusive. To reduce the drift caused by birefringence the acquisition time of the scans can be reduced by scanning less points or moving the probe quicker. This has adverse effect of either reducing the number of data points, which reduces the accuracy of the measurement or increases the speed of scanning which increases the probability of tip damage. This compromise limits the accuracy of the system.

Figure 5.18 presents a scan of the same area as that in figure 5.16, except in this case the waveguide mode has TM polarisation. The values of A_b/A_f is much larger than that of the TE mode, and is not consistent with that expected for this system. Monitoring of the transmitted optical power confirmed that the loss of the TE and TM modes is identical to within 2% and thus the visibility of the surface should be approximately the same. TM

(a)

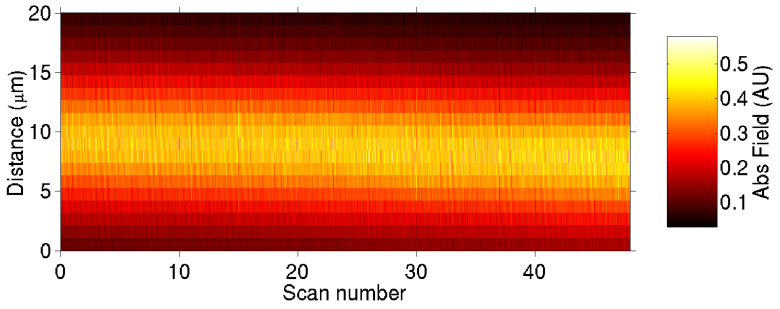

(b)

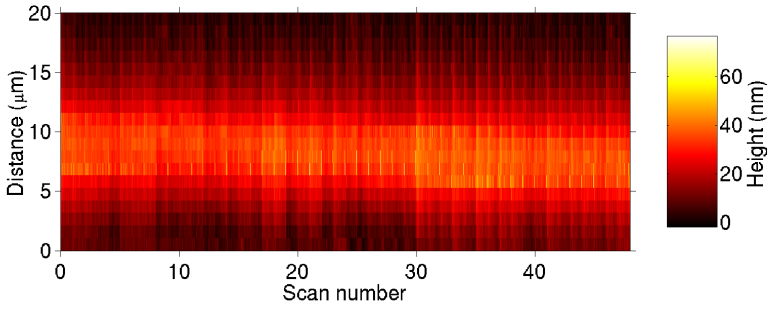

(c)

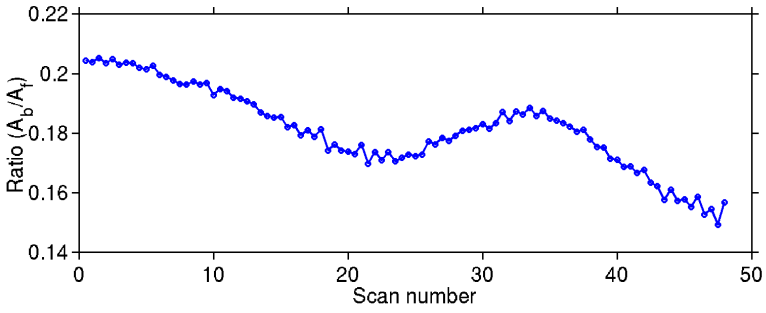

Figure 5.17: The concatenated data of 48 scans acquired in the same position. (a) shows the electric field magnitude and (b) shows the topographical data. The visibility ratio of each scan is presented in (c).

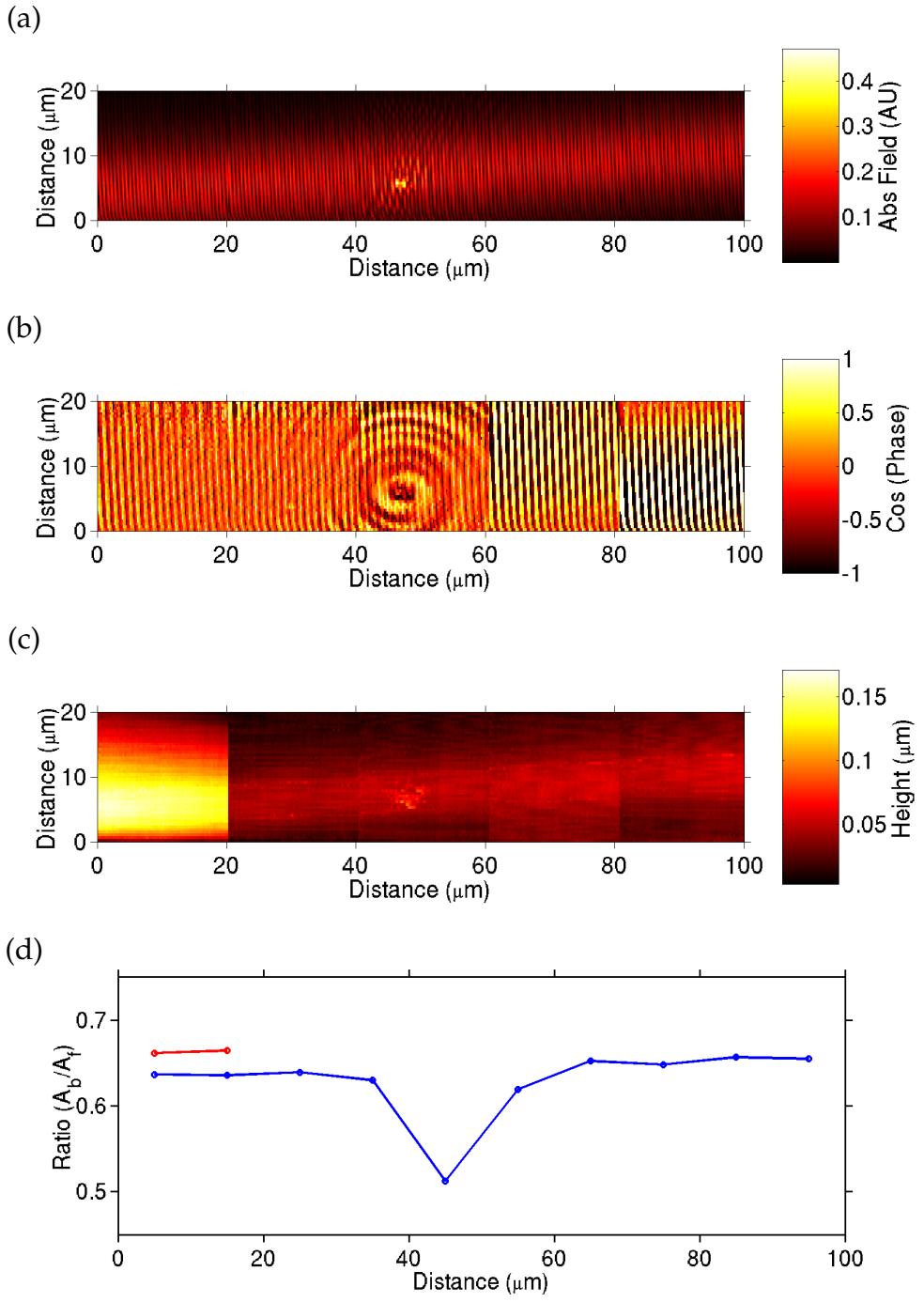

Figure 5.18: (a),(b) and (c) images of a 100μm by 20μm section of a 5μm waveguide with TM illumination. (d) shows the visibility ratio (A_b/A_f).

modes in a waveguide can be considered to be a composition of two orthogonal polarisations in the x and z direction. This therefore complicates the transfer function of the tip and it is thus more probable that several modes are coupled into the collection fibre. It was found that the TM mode generated a larger variation in the measured visibility, whereas the visibility of the TE mode was consistent about the value expected. The red line on graph (d) of figure 5.18, shows the ratio at the initial position after the scanning sequence was complete. It shows a change of $\approx 4\%$ over the 110 minutes required to take the scan. Again showing that the drift obscures the small change expected to be observed in the ratio which is associated with the propagation loss.

Figure 5.19 shows the effect of tip damage on the visibility of the standing wave. (a) shows a typical scan of a waveguide with a new tip, (b) shows a scan of the same waveguide after the tip was damaged. As expected the throughput of the tip increases as the aperture of the probe is increased through the damage. The visibility also suffers a huge decrease from 0.220 to 0.064, supporting the mechanism proposed by Bozhevolnyi *et al.* [26].

In summary the data shows that the technique is not able to measure the true visibility of the standing wave due to the finite size and asymmetry of the probe [26]. Relative visibility measurements can be obtained, however the reproducibility is poor due to slow fluctuations in the system. The accuracy of the loss measurement is presently limited by these changes. The future work section 5.7 highlights the necessary improvements to the SNOM system to reduce these fluctuations. The next section looks at the results obtained from the investigation into the wavelength modulation technique.

5.5.4.2 Wavelength modulation

The second loss measurement technique experimentally investigated, modulates the wavelength of the light in order to measure the visibility of the

(a)

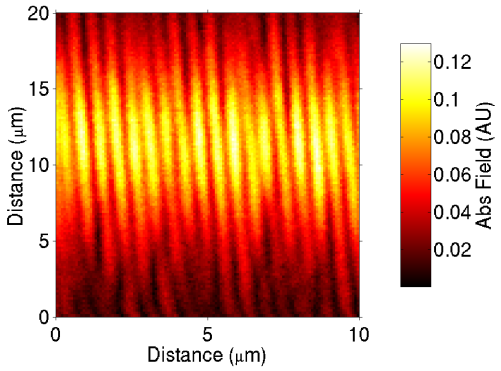

(b)

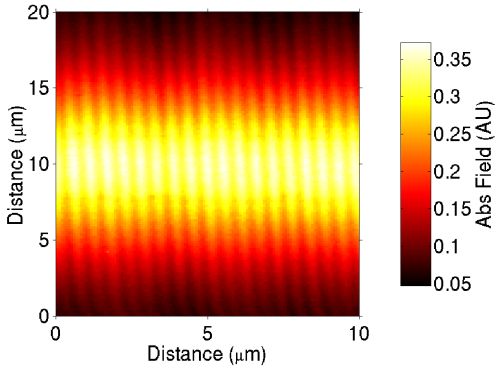

Figure 5.19: Images of the electric field magnitude above the same waveguide before (a) and after (b) the tip is damaged.The propagating mode was TE in both cases.

standing wave. The advantage of this technique is that the data is not plagued by topographical artifacts. The probe is placed in the centre of the waveguide using the shear force feedback to maintain a height of approximately 5 to 10nm away from the surface. The wavelength is then ramped and the electric field magnitude is monitored. The visibility can be calculated in the same way as shown in section 2.3.1.1. The period of the modulation ($\Delta\lambda$) also provides the distance of the probe to the end facet of the waveguide (d), the relation describing this is shown:

$$d = \frac{\lambda(\lambda + \Delta\lambda)}{2n_{eff}\Delta\lambda} \tag{5.10}$$

The wavelength accuracy defines the maximum distance from the end face of the waveguide. With the present system, loss measurements could be performed a distance of 4 meters from the end face of the waveguide. The Agilent laser allows scanning between 1495nm and 1640nm, however the power output is only sufficient to allow measurements in the range 1520nm to 1620nm.

Wavelength scanning has problems associated with cavity effects. A significant effort was made to remove oscillations with a period similar to that of the desired signal. Several components in the SNOM system produced undesirable Fabry-Perot modes, these oscillations were removed by using anti-reflection coatings and adjusting the angle of the components. The strongest effects where found to come from the acoustic optical modulators, fibre coupling objectives and the waveguide itself. The Fabry-Perot effect in the waveguide was reduced using refractive index matching oil between the end of the fibre and the waveguide, thus reducing the finesse of the system. The effect can be seen in figure 5.20, where the blue and red lines represents the intensity of the light coupled out of the waveguide with and without refractive index oil respectively. The addition of the index oil reduces the amplitude of the Fabry-Perot modulation and increases the coupling efficiency. Using the effective refractive index measured in section 5.5.2 the period of the modulation can be used to determine the length of the waveguide. Using this data the length was determined to

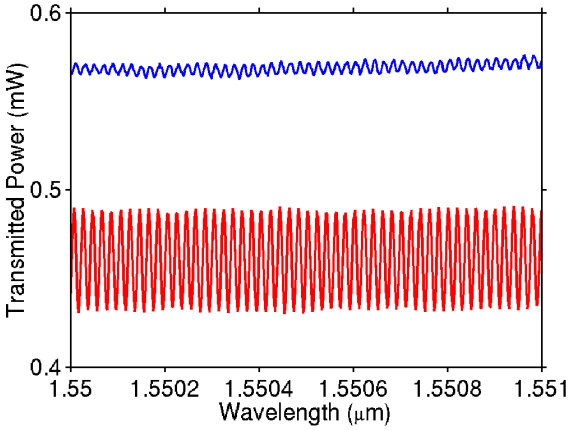

Figure 5.20: A plot of the transmission of a 4μm waveguide as a function of wavelength. In shows the effect of index matching oil, the blue and red lines display the transmission with and without index matching oil respectively.

be 4.09 $\pm$ 0.05 cm complimenting the length measurement taken with a micrometer of 4.030 $\pm$ 0.005 cm.

Figure 5.21 shows a scan of the electric field measured by the SNOM system as a function of wavelength, the data has been normalised with the monitored reference and signal strengths. The figure shows three modulations, the modulation with a period of approximately 5.5nm corresponds to that expected from tip being $\approx$ 150nm away from the end face of the waveguide. The higher and lower frequency modulation are expected to be the result of the birefringence of the optical fibre in the system. The low frequency modulation makes the visibility very difficult to determine, this is emphasized in figure 5.22 which shows another larger frequency range. The stress induced birefringence in standard fibre, produces a wavelength dependence on the output polarisation. Thus the polarisation of the mode coupled into the waveguide changes as a function of wavelength. This produces several undesirable effects as briefly mentioned in section 5.4.2. The result being the determination of the absolute visibility becomes impossible as the interference overlap (section 2.3) is no longer known. To

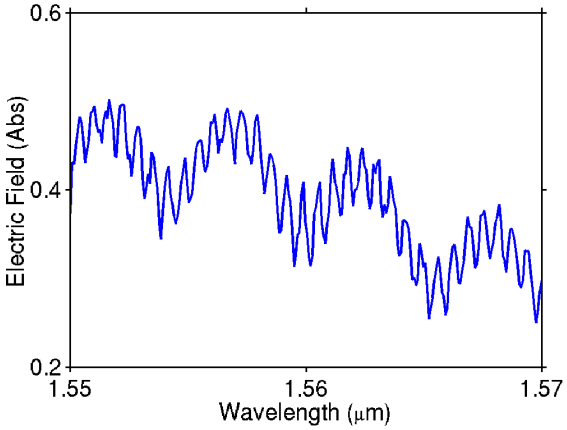

Figure 5.21: Plot showing the modulation of the electric field magnitude as a function of wavelength.

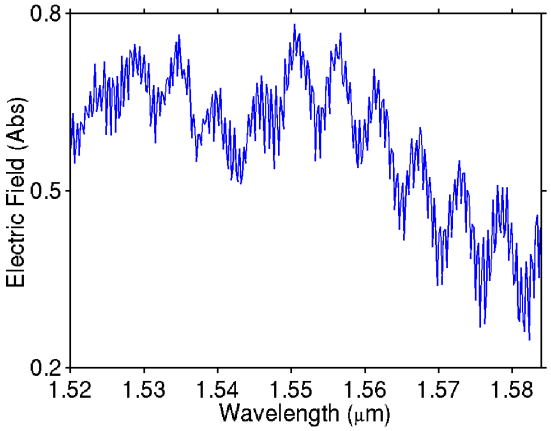

Figure 5.22: A larger scale plot of figure 5.21.

make this a viable detection system it must be made insensitive polarisation to a solution to which is discussion in section 5.7.

5.6 Conclusions

This chapter has introduced three potential methods of measuring the microscopic loss in waveguides using a SNOM technique. Two of the suggested techniques have been experimentally investigated.

The SNOM technique described uses a heterodyne interferometer system enabling low noise detection of the complex electric field in the NIR. Allowing the non-destructive measurement of telecommunication components at their specific operating wavelength. The technique also permits the measurement of the effective refractive index of the waveguide mode as 1.480 ± 0.011 [20]. This chapter also investigates a major source of the loss in the waveguides, surface defects and their associated electric field distributions.

The propagation loss is determined via the measurement of the visibility of a standing wave generated in the analysed waveguide. The methods potentially allow the measurement of the propagation loss of individual events, such as a nanoscale surface defect. It has also been shown that simultaneous characterisation of the waveguide and information about the loss defect can also be acquired using standard SNOM techniques. To enable accurate measurement of the visibility, a FFT technique was developed.

The investigation into the visibility of the standing wave showed that the measured visibility of TE modes produced similar results to those expected. However the value acquired from the TM coupled mode strongly deviated from that theorised. It is suspected that TE system approaches a simple single mode configuration, whereas the TM system deviates from this simple model due to depolarisation and thus sequential birefringent

mixing of the modes, causing the discrepancy.

Despite not being able to measure the absolute value of the visibility, the variation of the visibility around a microscopic defect was measured. However it was found that uncertainty in the technique caused by the instability of the system obscured the quantities being measured. The limitation of the system seems to originate from two possible mechanisms, slow damage of the SNOM tip or fluctuations in the birefringence of the collection fibre. Further investigation is required to establish the dominate mechanism. This investigation did however confirm the viability of the technique and highlighted the improvements necessary to make the system successful. The next section describes a proposed arrangement, capable of quantitative characterisation of planar and channel waveguides.

5.7 Future work

There are two topics of future work in this area. The first is the improvements necessary to produce a fully operational system capable of analysing the loss of a waveguide. The second topic is potential applications of such a system. The following section discusses these issues.

The two techniques for determining the microscopic loss were limited by several features most originating from the birefringence of the collecting fibre. This a familiar problem associated with precision fibre interferometers [28] and is solved by using polarising or polarisation maintaining optical fibres. These fibres allow preservation of the polarisation of an mode by an asymmetry in the fibres cross section. An improved optical arrangement using these fibres is shown in figure 5.23. The first improvement of the system is the use of PM fibre to couple light in the waveguide. This ensures the waveguide mode polarisation is independent of the wavelength. This solves one of the hindrances of section 5.5.4.2. The other change in the system is the use of PM fibre in the heterodyne detection system,

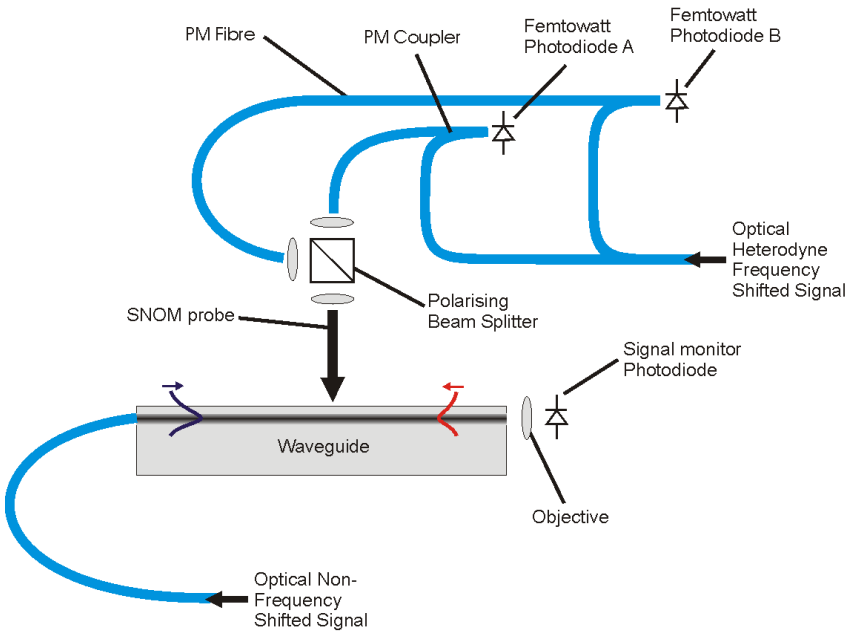

Figure 5.23: An improved optical setup, employing polarisation maintaining (PM) fibre.

thereby suppressing the birefringent noise which limited the accuracy of the measurement in section 5.5.4.1. In addition to these improvements the system shown in the figure 5.23 implements a second heterodyne interferometer; capable of independently measuring the orthogonal polarisations from the near-field probe.

The SNOM probe would still be fabricated from standard single mode fibre, however this length would be kept short and straight to minimise strain induced birefringence. The output of this fibre is then split into its two orthogonal polarisations using a polarising beam splitter. Each polarisation is then coupled into a separate PM fibre, where it is then mixed with the optical heterodyne reference beam and measured using a femto watt detector. This allows synchronous detection of the polarisations coupled into the tip. Separating the modes generated with the tip prevents energy transfer between the modes and allows accurate measurement of the visibility. This will not however, allow the absolute measurement of the visibility as this is still defined by the tip aperture. The use of PM fibres

also ensures that maximum signal is always achieved, due the intrinsic parallel polarisation of the reference and signal modes of the heterodyne interferometer. As a consequence it also removes the necessity for fibre polarisation rotators, and thus increasing the stability of the system. The heterodyne detection system also allows the relative phase shift between the orthogonal polarisations to be detected. The disadvantage of the system is the addition cost of the PM components.

An investigation is also required into magnitude of the SNOM tip wear. If the system previously described is stable, it presents an effective method of characterising the probe transmission as a function of the interaction with the surface.

The proposed system would have potential for investigating not only the propagation loss of nano or micro-scale events, but it may also provide some information about the depolarisation of the field at the aperture of the probe.

5.8 References

[1] B. M. Foley, P. Melman, and K. T. Vo. "Novel Loss Measurement Technique for Optical Wave-Guides by Imaging of Scattered-Light". *Electronics Letters*, 28(6):584–585, 1992.

[2] B.E.A Saleh and M.C Teich. "Fundementals of Photonics". pages 296–297. J. Wiley and Sons, New York, 1991.

[3] A. Ghatak and K. Thyagarajan. In *Introduction to Fiber Optics*, pages 413–416. Cambridge University Press, New York, 1998.

[4] P.K. Tien, R. Ulrich, and R. Martin. *Applied Physics Letters*, 14:291, 1969.

[5] Y.H. Won, P.C. Jassaud, and G.H. Chartier. "Three-prism loss measurements of optical waveguides". *Applied Physics Letters*, 37(3):269–271, 1980.

[6] Y. Luo, D. C. Hall, L. Kou, L. Steingart, J. H. Jackson, O. Blum, and H. Hou. "Oxidized $AlGaAs$ heterostructure planar waveguides". *Applied Physics Letters*, 75(20):3078–3080, 1999.

[7] R. Arsenault, D. Gregoris, S. Woolven, and V. M. Ristic. "Wave-Guide Propagation-Loss Measurement Technique". *Optics Letters*, 12(12):1047–1049, 1987.

[8] L. T. Wang, K. Iiyama, F. Tsukada, N. Yoshida, and K. Hayashi. "Loss Measurement in Optical Wave-Guide Devices by Coherent Frequency-Modulated Continuous-Wave Reflectometry". *Optics Letters*, 18(13):1095–1097, 1993.

[9] T. Feuchter and C. Thristrup. "High-Precision Planar Wave-Guide Propagation Loss Measurement Technique Using a Fabry-Perot Cavity". *IEEE Photonics Technology Letters*, 6(10):1244–1247, 1994.

[10] E. Fluck, E. van Dijk, J.P. Korterik, A.M. Otter, L. Kuipers, and N.F. van Hulst. "Coherent imaging of local fields in photonic crystals". In *QELS*, page 51, 2001.

[11] Melles Griot Ltd. *Nanomax-HS 3 axis flexure stage*. Instruction Handbook for the Melles Griot Nanopositioning modular system. Melles Griot, Cambridge, 1998.

[12] T. Izama and H. Nakagome. "Optical waveguide formed by electrically induced migration of ions in glass plates". *Applied Physics Letters*, 21:584–587, 1972.

[13] R. V. Ramaswamy and R. Srivastava. "Ion-Exchanged Glass Wave-Guides - a Review". *Journal of Lightwave Technology*, 6(6):984–1002, 1988.

[14] A. Brandenburg. "Stress in Ion-Exchanged Glass Wave-Guides". *Journal of Lightwave Technology*, 4(10):1580–1593, 1986.

[15] J. L. Jackel, K. Y. Lee, and F. J. Favire. "Do Glass Wave-Guides Depolarize". *Journal of Lightwave Technology*, 3(4):818–819, 1985.

[16] J. E. Gortych and D. G. Hall. "Fabrication of Planar Optical Wave-Guides by K+ Ion Exchange in Bk7 and Pyrex Glass". *IEEE Journal of Quantum Electronics*, 22(6):892–895, 1986.

[17] K. Tsutsumi, H. Hirai, and Y. Yuba. "Characteristics of Swelling of Sodium-Potassium Ion-Exchanged Glass Wave-Guides". *Electronics Letters*, 22(24):1299–1300, 1986.

[18] S. Blaize, S. Aubert, A. Bruyant, R. Bachelot, G. Lerondel, P. Royer, J. E. Broquin, and V. Minier. "Apertureless scanning near-field optical microscopy for ion exchange channel waveguide characterization". *Journal of Microscopy-Oxford*, 209:155–161, 2003.

[19] K. K. Lee, D. R. Lim, L. C. Kimerling, J. Shin, and F. Cerrina. "Fabrication of ultralow-loss Si/SiO2 waveguides by roughness reduction". *Optics Letters*, 26(23):1888–1890, 2001.

[20] A. L. Campillo, J. W. P. Hsu, C. A. White, and C. D. W. Jones. "Direct measurement of the guided modes in $LiNbO_3$ waveguides". *Applied Physics Letters*, 80(13):2239–2241, 2002.

[21] A. Nesci. *Measuring amplitude and phase in optical fields with sub-wavelength features.* PhD thesis, University of Neuchatel, 2001.

[22] J. J. Greffet and R. Carminati. "Image formation in near-field optics". *Progress in Surface Science*, 56(3):133–237, 1997.

[23] J. C. Weeber, F. deFornel, and J. P. Guodonnet. "Numerical study of the tip-sample interaction in the photon scanning tunneling microscope". *Optics Communications*, 126(4-6):285–292, 1996.

[24] D. Courjon. *Near-field microscopy and near-field optics*. Imperial College Press, 2003.

[25] S. I. Bozhevolnyi and E. A. Bozhevolnaya. "Near-field imaging of the interference pattern of counterpropagating evanescent waves". *Optics Letters*, 24(11):747–749, 1999.

[26] S. I. Bozhevolnyi, B. Vohnsen, and E. A. Bozhevolnaya. "Transfer functions in collection scanning near-field optical microscopy". *Optics Communications*, 172(1-6):171–179, 1999.

[27] P. Hariharan. *Optical Interferometry*. Academic Press, Sydney, 1985.

[28] B.A.W.H Knarren. *Application of optical fibres in precision heterodyne laser interferometry*. PhD thesis, TU Eindhoven, 2003.

Chapter 6

Characterisation of holey fibres

6.1 Introduction

This chapter describes an investigation into the optical properties of a large mode area holey fibre. Holey fibres are a form of microstructured fibres which provide unique optical properties that are not achievable with conventional fabrication methods. These include novel dispersion properties [1,2], single mode operation at all wavelengths [3] and extreme mode sizes [4]. This diversity of the waveguide structures and their properties make it an exceedingly interesting field.

The work in this chapter differs from the other work presented in this thesis as it images propagating components. As a result, the resolution of the imaging system is diffraction limited. There are several conventional characterisation techniques, however the SNOM technique has several advantages. The high numerical aperture of the SNOM probe gives the technique high spatial bandwidth. It also allows accurate positioning above the surface of the fibre with nanometer resolution. In addition the phase of the electric field can also be measured. The motivation of the work is to demonstrate the usefulness of the SNOM technique and to verify a theoretical model of the fibre mode.

The work presented here was produced as part of collaborative investigation into large mode holey fibres. Consequently some of the data presented in this chapter has featured in the thesis of the collaborator [5].

6.2 Holey fibres

Traditional optical fibres rely on a doped core such as SiO_2/GeO_2 to generate sufficient refractive index contrast to guide the light. In contrast microstructured fibres guide due to small voids or air holes along the length of the fibre, and can therefore be fabricated from a single material. The fibres normally consist of a solid rod that forms the core, surrounded by a microstructured cladding. A number of different examples can be seen in figure 6.1.

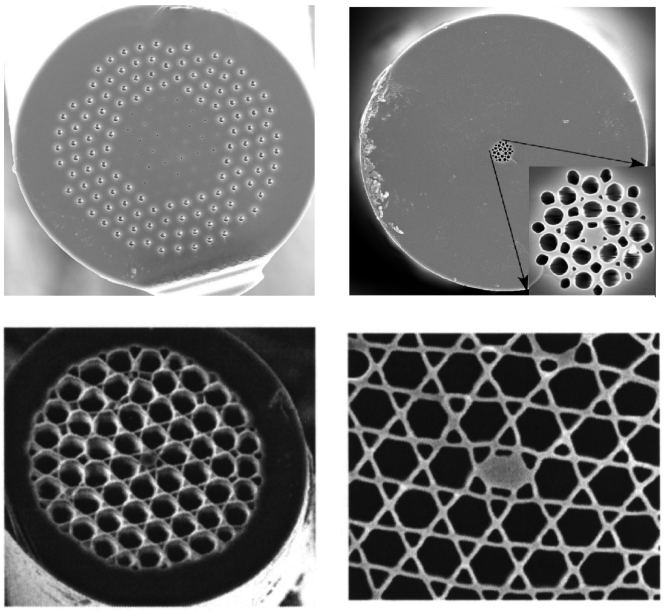

Figure 6.1: A selection of holey fibres produced at the University of Southampton, showing the variety of the different structures.

There are two categories of microstructured fibres, defined by the method in which they guide the light at a specific wavelength. One category relies on the periodicity of an array of air holes to produce a photonic band gap.

This prevents propagation perpendicular to the axis of the fibre and hence the light is confined to the core region. These are called photonic crystal fibres. The second category uses the air holes in the cladding region to lower the spatial average refractive index and thus guide in a similar manner to that used in conventional techniques. These are referred to as holey fibres. The primary advantage over conventional techniques is the extensive control over the index and profile of the cladding. It is this control that generates such extreme optical properties. A complete review of the properties and applications of holey fibres can be found elsewhere [6].

6.2.1 Fabrication

The fabrication of the holey fibres commences with the stacking of silica rods and capillaries which form the core and cladding of the final fibre. These are then incorporated into a preform which is drawn in a modified fibre pulling tower. Due to the commercial interest in these fibres the exact fabrication process has not been published.

6.2.2 Conventional characterisation techniques

The characterisation of holey fibres can be classified into physical and optical. The physical structure of the fibre is required to model the optical mode. In standard fibre fabrication the dimensions and composition of the fibre is determined from the original profile of the preform. However due to the complex structure of the perform the fabrication parameters vastly affect the final structure of the fibre. As a result the final structure of the fibre can not be determined from the initial preform. The refractive index profile must be collected from direct analysis of the fibre. The single material nature of most holey fibres simplifies the characterisation process, as the topography of the fibre returns the refractive index profile. Optical microscopy can yield some information, but the feature sizes tend

to go beyond the resolution of the technique. Thus the standard technique is SEM analysis, this provides an effective tool to acquire qualitative information about the structure. To achieve a higher resolution, atomic force microscopy can also be applied [7].

Optical characterisation can be achieved by a number of techniques, classically this is achieved by far-field collection using a CCD detector. However diffraction causes the size of the mode to alter. To prevent excessive diffraction of the mode, an optical microscopy technique can be employed. This provides an easy method of imaging the field, however these techniques are still fundamentally limited due the loss of the high spatial frequency components. SNOM imaging is potentially capable of collecting many more spatial frequency components and therefore provide an accurate measurement of the fibre mode. The next section provides an explanation of the holey fibre guidance mechanism.

6.3 Holey fibre guidance mechanism

Holey fibres guide light by the effective index different between the solid core region and the holey cladding region. The method is depicted by the diagram shown in figure 6.2. The blue line in the diagram represents the

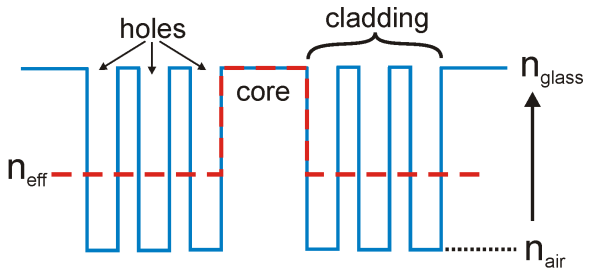

Figure 6.2: A diagram showing the principle of effective index guiding. After [8]

cross section of the holey fibres refractive index. The holes have a refractive index equal to take of air n_{air}, while the glass regions have an index of

n_{glass}. The effective index is the spatial average index of the structure and is shown by the red line. The effective index of the core is the same as that of the bulk glass, however the effective index of the cladding is between that of air and silica. The concept of the effective index allows the holey fibre system to be treated as a conventional step index fibre. However unlike a conventional fibre the index profile is dependent on the fraction of air to glass and the wavelength of the mode. Careful engineering of these parameters allow the fibre to be tailored to a large wavelength range. It is this feature that gives holey fibres the capability to be endlessly single mode.

This representation describes the basic guiding mechanism of holey fibres. Detailed analysis of the fibres modes requires a rigorous modelling and can be achieved via a number of different techniques [9, 10, 2, 11, 4]. A few approaches use scalar approximations to successfully predict holey fibre modes [2], however the approximations have been shown to limit the range of fibre geometries [2]. As a result, a full vector representation of the propagating light is necessary to accurately predict the optical properties [11, 4]. The predicted mode profiles presented in this chapter use a full vector model, and was performed by Monro and coworkers who developed the technique [4].

6.4 Imaging a holey fibre

6.4.1 The holey fibre sample

The fibre investigated here is a large mode area fibre fabricated by the holey fibre group in the Optoelectronics Research Centre. An SEM image of the fibre is presented in figure 6.3. The fibre is composed of a lattice of regularly spaced holes running the length of the fibre. The core is produced by the removal of the central hole, the resulting fibre has a large diameter

core surrounded by a cladding region with a low air to silica ratio. It has been designed for endlessly single mode operation and thus has a large cladding region. The large core also makes it applicable for high power delivery attributable to its low insertion loss and low nonlinearity.

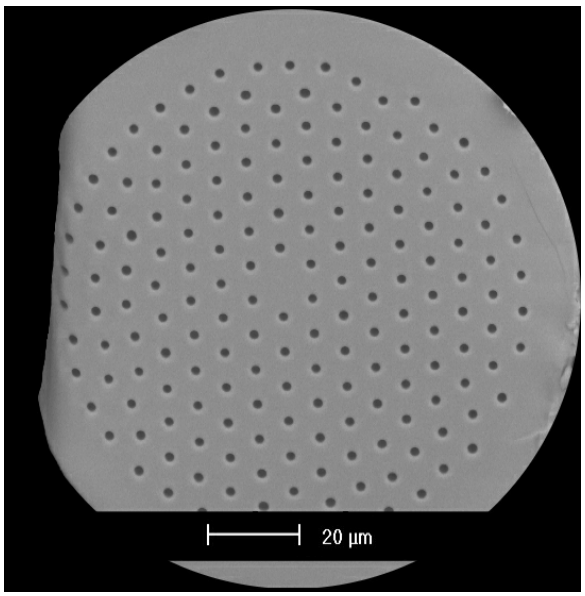

Figure 6.3: An SEM image of the large mode area holey fibre, fabricated at the Optoelectronics Research Centre.

6.4.2 Experimental procedure

A diagram of the set up is shown in figure 6.4. A coated probe was used with approximately 110nm of aluminium on the side walls of the fibre. The length of the holey fibre used was approximately 0.7 meters and was butt coupled to a single mode telecoms fibre. Care was made to ensure the holey fibre was kept as straight as possible to prevent distortion of the mode. All the measurements were taken at a wavelength of 1550nm.

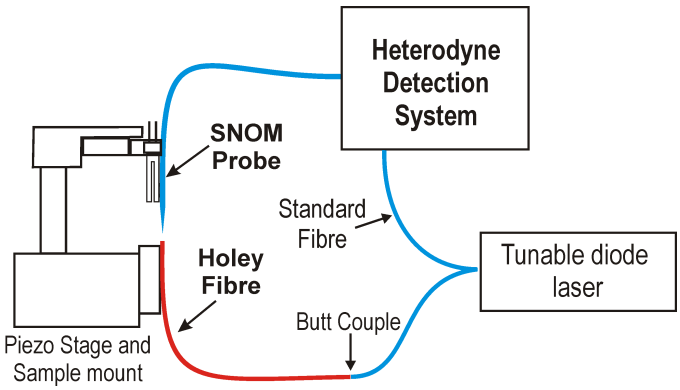

Figure 6.4: A schematic of the SNOM setup used to image holey fibres.

6.5 Results and analysis

Due to the large surface features associated with holey fibres, constant separation scans produce large topographical artifacts, as a result, this work employs constant height imaging. The technique uses the shear force detection to locate the surface, after which it scans in a plane parallel to the surface. Figure 6.5 shows false colour images of the optical field, 100nm above the surface. This separation was sufficiently large to prevent the probe from touching the surface due to thermal drift and external vibrations, but close enough to prevent excessive diffraction.

The white contour lines on the electric field data illustrate the location of the holes, which were acquired in a previous scan of the topography. The air holes in the fibre spatially correspond to the dips in the electric field magnitude. The optical phase data shows a flat phase front, however above the holes there are also fluctuations in the phase. The electric field data shows that the mode is not confined to the inner most ring of the holes. The limited spatial range of the piezo stage makes it difficult to observe the extent of the mode. Figure 6.6 shows a scan of a quarter of a mode, again taken in a constant plane above the surface. The electric field data (6.6 (a)) shows the mode interacting with the second ring of holes, it is shown more clearly with a logarithm scale shown in (b). The phase data again shows the shifts around the holes, the second ring of holes dis-

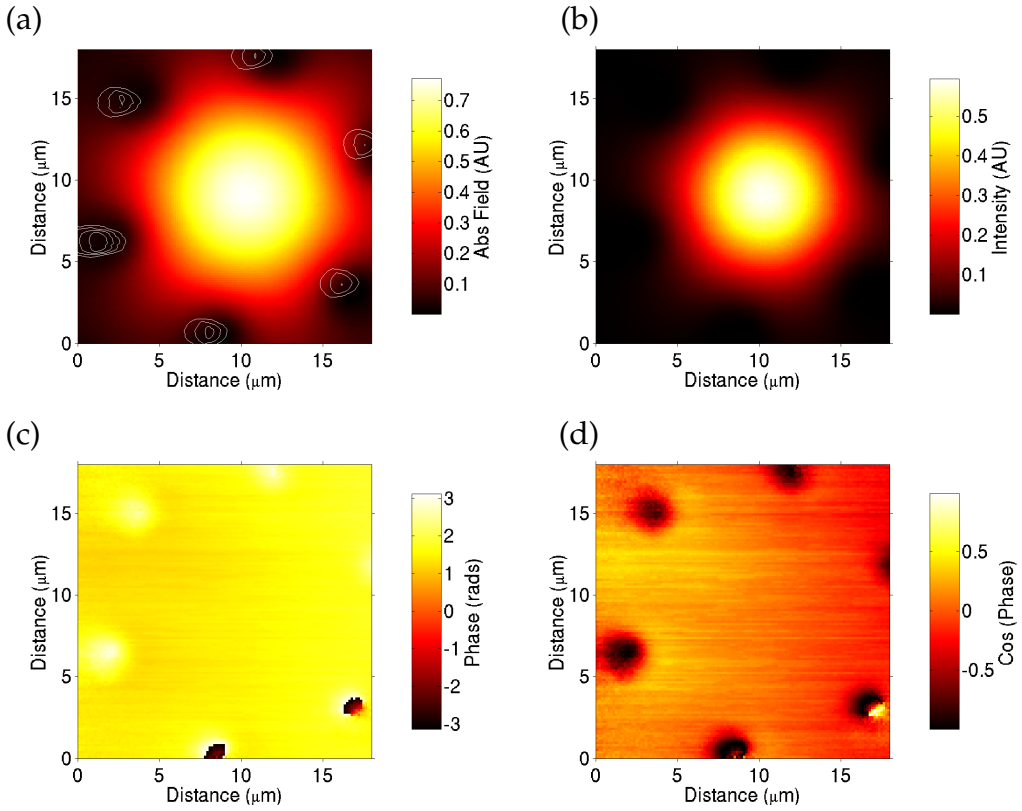

Figure 6.5: False colour images showing the mode of the holey fibre 100nm above the surface. (a) and (b) present the electric field and the intensity. (c) and (d) present the phase and the cosine of the phase [5].

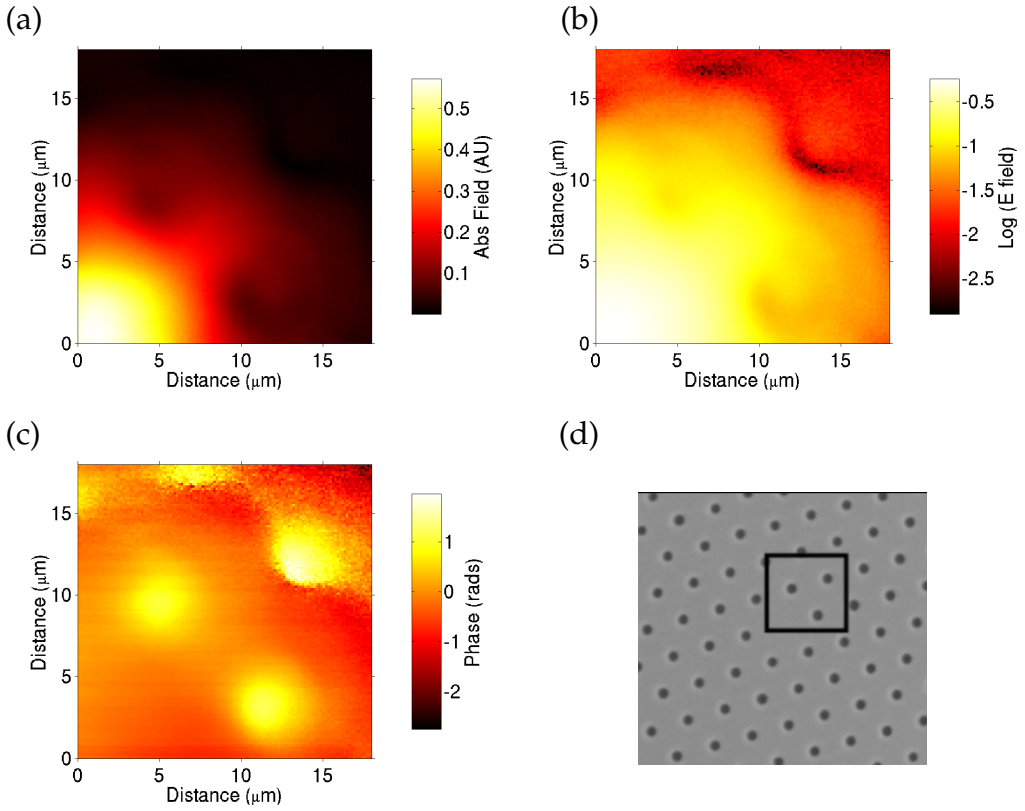

Figure 6.6: False colour images of a quarter of the mode showing the extent of the mode. (a) and (b) present the electric field with a linear and logarithmic scale respectively and (c) shows the phase. The location of the scan is shown in (d), and is defined by the square box. The scan is taken 3 μm above the surface.

plays a larger shift than that of the inner ring. A further investigation of the phase effects is shown in section 6.5.3. The next section compares the experimental results to a theoretically predicted mode.

6.5.1 Theoretical prediction

A comparison between experimental data and a theoretical model allows validation of both the practical technique and of the model. Figure 6.7 shows the predicted mode profile at 1550nm of the large mode holey fibre. The modelling was performed by the fabricators of the fibre. A visual com-

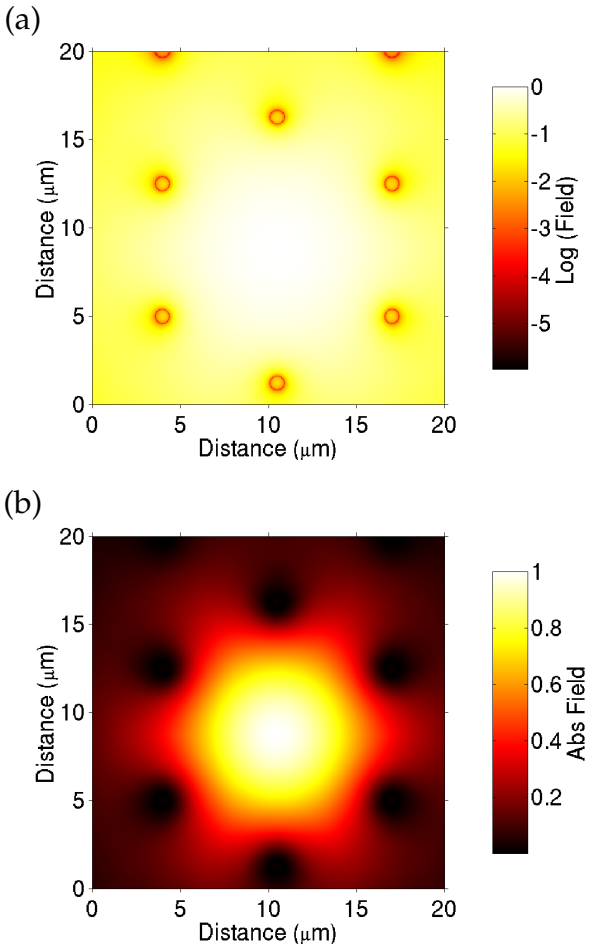

Figure 6.7: Theoretically predicted 1550nm mode of the holey fibre, (a) and (b) present the data with a linear and logarithmic electric field scale.

parison between the theoretical profile and that obtained experimentally

6.5(a), indicates agreement. However a quantitative comparison can be achieved by examining cross sections of the mode. Figure 6.8 shows cross sections of the theoretical and experimental data. The location of the cross sections is shown in (a) and are taken directly across and between the inner ring of holes corresponding to the smallest and largest parts of the mode. The cross sections show that the experimentally measured mode profile is more confined than that theoretically predicted. An error associated with the SNOM measurement such as a large aperture would generate a measured mode with a larger mode profile. However the same deviation from the model has also been acquired using conventional characterisation techniques. The error between in the FWHM of the measured and predicted cross sections is 7% in the x axis and 10 % in the y axis.

The error was initially expected to be the result of very small interstitial holes which were not capable of being imaged with a SEM. However AFM analysis showed no indication of any small holes. Recent investigation by the fabricators of the fibre, has suggested that the error is the result of a refractive index mismatch between the silica used to make the core, and that used to make the cladding. This additional increase in the core index assists in the confinement of the mode and therefore reduces its size. The next section briefy looks at the effect of the mode propagating.

6.5.2 Mode propagation

One of the advantages of using a SNOM technique is its ability to accurately characterise the optical field in a plane parallel to the end face of the fibre. Figure 6.9 shows a series of scans indicating the effect of propagation on the mode profile. The left hand column of the scans presents the electric field mode profile at 0.2, 5.0, 8.0 and 12.0 μm above the end of the fibre in descending order. The right hand column shows the same data but with a logarithm scale to aid inspection of the lower amplitudes. The data illustrates the speed of the evolution of the mode as the high spatial

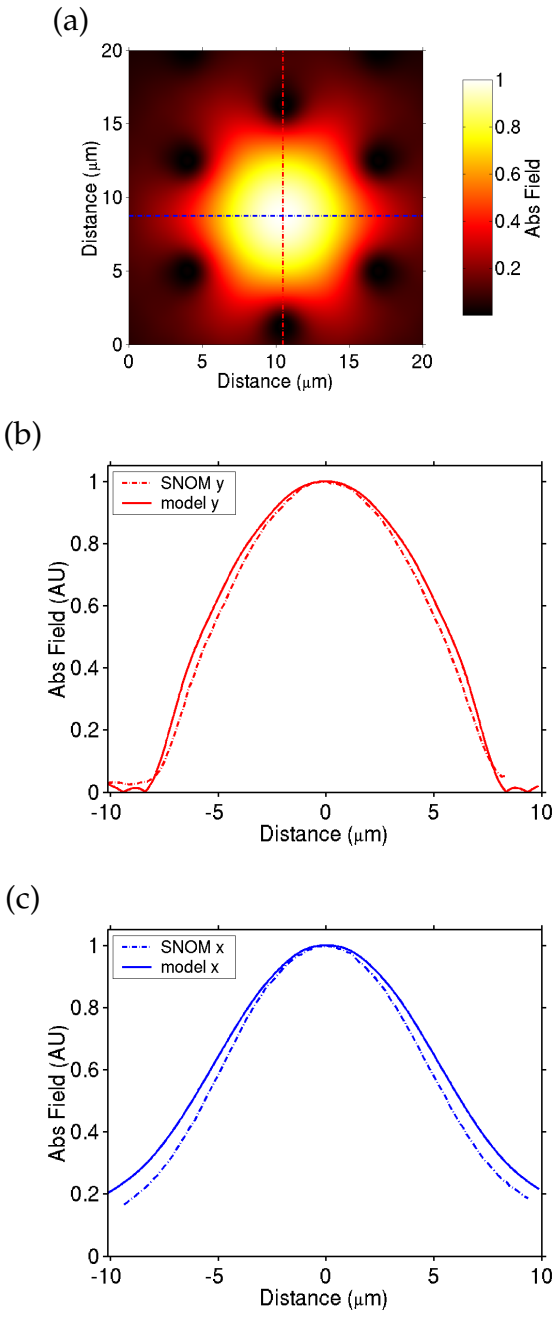

Figure 6.8: Cross sections of the theoretically predicted and the experimentally measured mode profile. (a) shows the locations of the cross sections in the x and y directions, (b) and (c) show the cross sections along these lines [5].

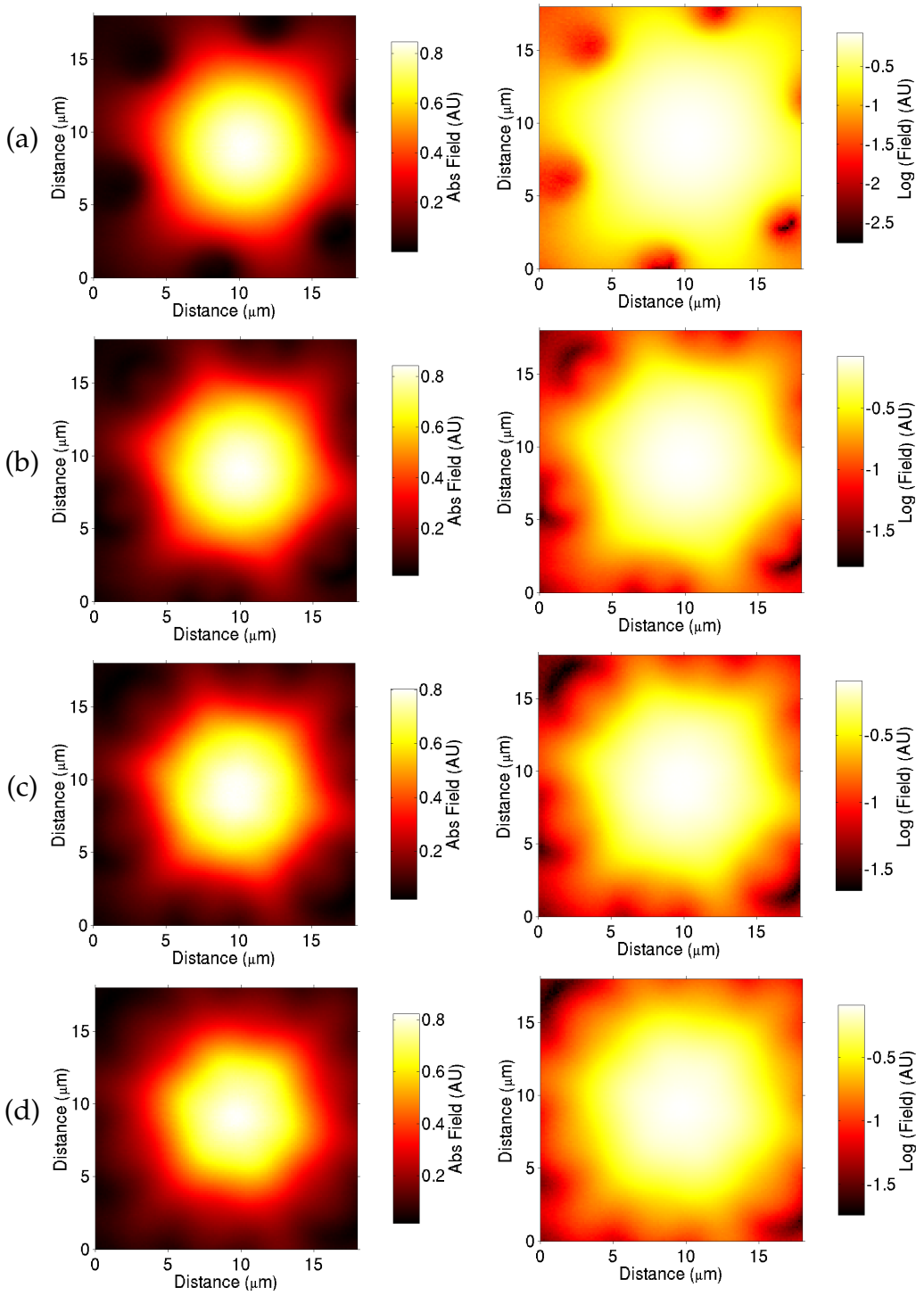

Figure 6.9: A series of images showing the electric field as a function of height away from the end face of the fibre. The left hand column shows a linear scale, the right hand column is a logarithmic scale. (a) is at a height of 200nm above the surface, (b) 5 μm, (c) 8 μm and (d) 12 μm.

frequencies are lost due to diffraction. In addition, it highlights the need for high axial resolution when imaging the modes using conventional microscopy techniques. These results support the findings of a similar investigation using standard microscopy [12]. The next section investigates the z dependence of the field by imaging in the plane normal to the surface.

6.5.3 Z scans

An extremely useful technique for investigating the propagating light is the z scan. These present the electric field in the plane normal to the surface and provide a 2-dimensional cross section of the propagating mode. There are two scanning techniques used to acquire z data. The first method uses the shear force technique to initially locate the surface, after which the probe is raster scanned in the plane. This technique is quick, and thus large areas can be characterised with minimal thermal drift. The disadvantage with the technique is that it can not be used for measurements in close proximity ($\lessapprox 100\mathrm{nm}$) of the sample. Figure 6.10 presents a cross section of the mode using this technique, with the vertical direction being the z axis. The images in (a) and (b) show the linear and logarithm scale of the electric field magnitude, the scan starts 0.5 μm above the surface and propagates up the page with increasing z. The images show the mode broadening and peak amplitude reducing with propagation distance, this effect is small due to the comparatively large confocal parameter. The data also shows a periodic oscillation in the z direction, which is most visible in figure (a) and is the result of multiple reflections between the end of the probe and surface, generating a Fabry-Perot effect. This is confirmed by the period of fluctuations (1.55/2) μm and the reduction in the amplitude of the beating as a function of distance.

The effect of the holes is highlighted using the logarithmic scale in (b) by two dark strips at the edges of the mode. To investigate the effects of the holes in more detailed z scans were taken across the holes. Due to the lim-

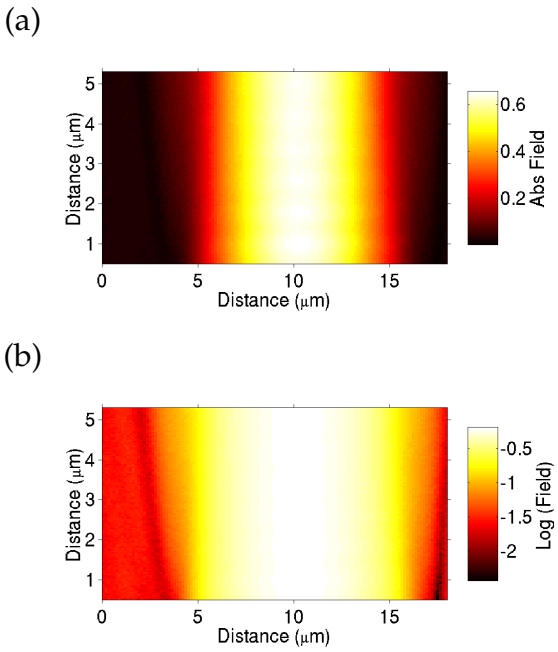

Figure 6.10: Figures showing a 2 dimensional cross section of the holey fibre mode. (a) presents the data with a linear scale, (b) is presented with a logarithmic scale.

ited scan range and the symmetry of the fibre a cross section was taken from the centre of the mode across two of the holes as shown by the green line in figure 6.11 (a). The corresponding z scan data of the electric field magnitude is shown in (b), a logarithmic scale version of the same data is shown in (c). The experimental data again exhibits similar features to that shown in the previous figure. Figure 6.11 (d) shows a theoretical prediction of the mode as it propagates away from the end of the fibre. The measured data commences at a distance of 1 μm above the surface of the fibre and moves at a position 9.5 μm above the surface. The predicted mode begins at the surface and moves to 9.5 μm above the surface. A visual comparison between the predicted and measured field shows good agreement. The predicted data is generated from the theoretical mode (figure 6.7), by a Fourier transform beam propagation technique. Details of the technique can be found elsewhere [13]. The corresponding phase information of the previous electric field images is shown in figure 6.12 and exhibits some interesting features of the mode. The measured phase data in (b) shows

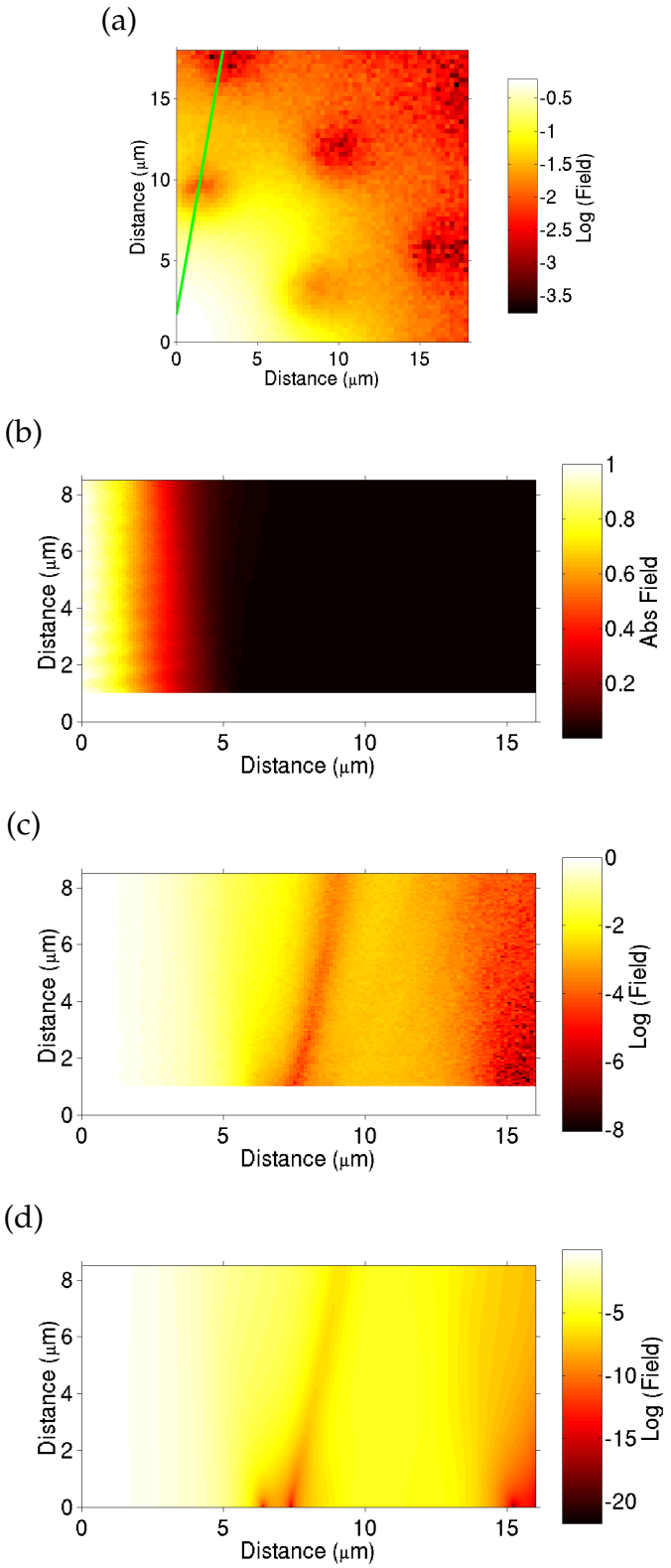

Figure 6.11: (b) and (c) show a linear and logarithmic scale of the electric field magnitude in a plane perpendicular to the surface plane of the fibre. The perpendicular plane is defined by the green line in (a). (d) shows the logarithm of the predicted electric field.

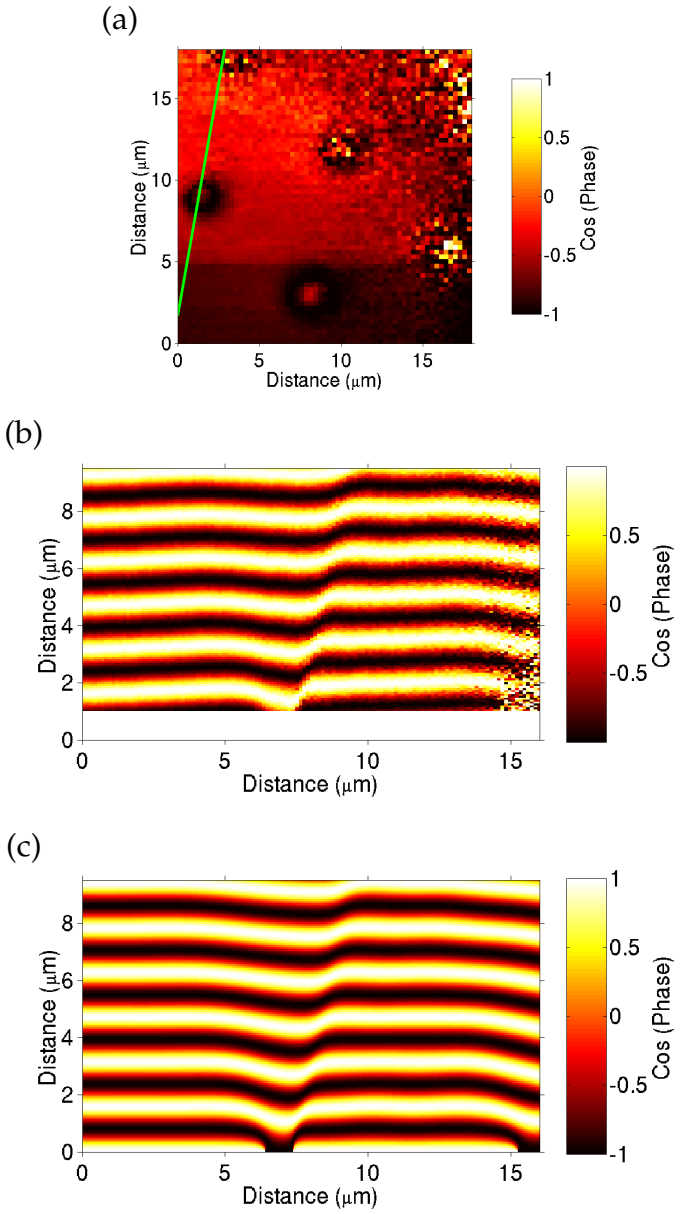

Figure 6.12: (b) and (c) shows the corresponding measured and predicted phase of the electric field presented in figure 6.11. Again (a) defines the intersection of the perpendicular plane with the plane of the fibre surface.

a fluctuation of the phase in proximity with the holes and is corroborated by very similar features shown on the predicted phase shown in (c). The slight incline of the phase relative to the surface is a result of thermal drift in the interferometer. The fluctuations are the same as those observed in figure 6.5 and are the result of the high spatial frequencies of the guided mode. The effects are seen to be most prominent at the surface of the fibre, as the high frequency components have a greater angle of propagation (see section 2.2.2), and thus only overlap with the lower spatial frequencies close to the end of the fibre.

The theoretical data in (c) shows that at the surface of the fibre the mode above the holes has an opposing phase. The predicted mode shown in figure 6.7 (b) demonstrates the turning point of the phase by a ring of low electric field at the edge of the holes.

The theoretical z scan data shown in 6.11(d) and 6.12(c) demonstrates the necessity to image the holey fibre well within 1 micron of surface, due to the large changes in the electric field magnitude and phase.

The second z scan technique uses the PID feedback to repeatedly scan the tip into the surface while collecting the optical data. Figure 6.13 shows some preliminary data, using this technique. The advantage with this technique is that it enables the measurement of the field within the holes, however the drawback is the long acquisition times. It was hoped that the period of the phase down the holes would allow the determination of the propagation constant of the fibre mode. However the small size of the holes prevented the collection of sufficient data to determine an accurate value. However the reliability of the measurement is questionable due to the unknown interaction of the probe with the electric field.

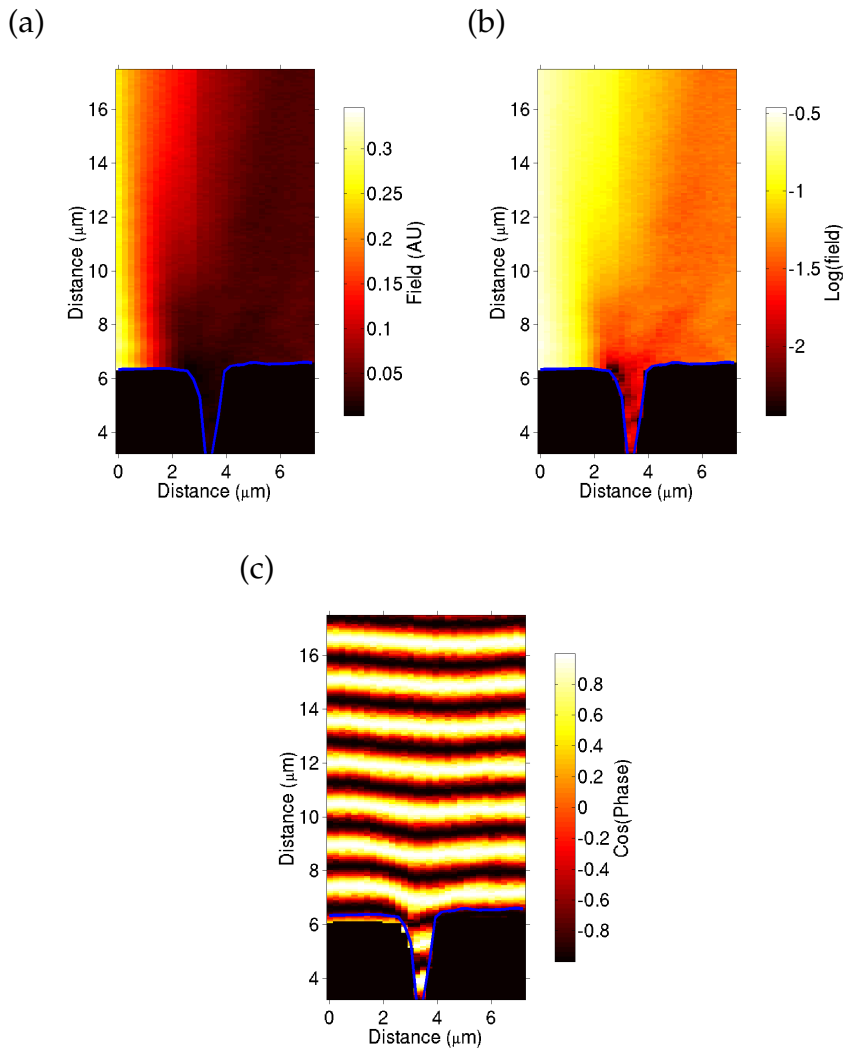

Figure 6.13: A set of z scan data presenting the electric field at the very surface and down a hole. (a) and (b) show a linear and logarithmic scale of the electric field magnitude. (c) presents the cosine of the optical phase [5].

6.6 Conclusions

The chapter has demonstrated the applicability of a interferometric SNOM technique for the complete optical characterisation of holey fibres. The method utilises coated SNOM probes to measure the propagating mode of a large mode holey fibre. The work presented differs from that used in the previous chapters by measuring propagating light and thus the resolution is limited by diffraction. To prevent the topographical artifacts associated with the microstructure of the fibre, the data was acquired using a constant height scanning technique.

The electric field magnitude of the mode was successfully imaged and found reasonable agreement, however a $\approx 7-10\%$ error was observed between the theoretical mode profile and that experimentally measured. The error is suspected to be the result of a refractive index mismatch between the core and cladding material.

The effect of propagation on the mode was demonstrated by imaging the mode at increasing distances from the fibre surface, and has highlighted potential resolution issues when imaging holey fibre modes with conventional microscopy techniques [12]. Imaging in the plane perpendicular to the fibre surface investigated the propagation effects in more detail. The results showed significant fluctuations in the phase above the holes, which were corroborated by a theoretically predicted mode. Preliminary results have been presented and show a potential method of measuring the propagation constant of the mode within the fibre.

6.7 Future work

The future work in this area would initially address the error observed between the predicted and measured mode profiles. New holey fibres fabricated with matching core and cladding indices are currently being pro-

duced. These new fibres will help determine the origin of the discrepancy and validate the modelling technique.

Recently there has been much interest into the further investigation of holey fibres with a high air/glass ratio. Theoretical modelling has shown some interesting effects of the orientation of the polarisation within close proximity of the holes. With the use of the polarisation sensitive SNOM probes mentioned in section 3.4, these changes in polarisation should be measurable.

From a system improvement perspective the investigation of large mode holey fibres would be aided by a piezo-electric translation stage with a larger scanning range. Additionally the fabrication and application of ultra sharp SNOM probes may assist in the determination of the propagation constant by probing the period of the optical phase.

6.8 References

[1] D. Mogilevtsev, T. A. Birks, and P. S. Russell. "Group-velocity dispersion in photonic crystal fibers". *Optics Letters*, 23:1662–1664, 1998.

[2] T. M. Monro, D. J. Richardson, N. G. R. Broderick, and P. J. Bennett. "Holey optical fibers: An efficient modal model". *Journal of Lightwave Technology*, 17(6):1093–1102, 1999.

[3] T. A. Birks, D. Mogilevtsev, J. C. Knight, and P. S. Russell. "Dispersion compensation using single-material fibers". *IEEE Photonics Technology Letters*, 11(6):674–676, 1999.

[4] T. M. Monro, D. J. Richardson, N. G. R. Broderick, and P. J. Bennett. "Modeling large air fraction holey optical fibers". *Journal of Lightwave Technology*, 18(1):50–56, 2000.

[5] C. W. J. Hillman. *Scanning near-field optical microscope characterisation of microstructered optical fibre devices.* PhD thesis, University of Southampton, 2002.

[6] T. M. Monro and D. J. Richardson. "Holey optical fibres: Fundamental properties and device applications". *Comptes Rendus Physique*, 4(1):175–186, 2003.

[7] C. W. J. Hillman, W. S. Brocklesby, T. M. Monro, W. Belardi, and D. J. Richardson. "Structural and optical characterisation of holey fibres using scanning probe microscopy". *Electronics Letters*, 37(21):1283–1284, 2001.

[8] T. M. Monro. "Tutorial on holey fibres". In *OFC 2002*, California, 2002.

[9] F. Brechet, J. Marcou, D. Pagnoux, and P. Roy. "Complete analysis of the characteristics of propagation into photonic crystal fibers, by the finite element method". *Optical Fiber Technology*, 6(2):181–191, 2000.

[10] M. Qiu. "Analysis of guided modes in photonic crystal fibers using the finite-difference time-domain method". *Microwave and Optical Technology Letters*, 30(5):327–330, 2001.

[11] A. Ferrando, E. Silvestre, J. J. Miret, and P. Andres. "Full-vector analysis of a realistic photonic crystal fiber". *Optics Letters*, 24(5):276–278, 1999.

[12] N.A. Mortensen and J.R. Folkenberg. "Near-field to far-field transition of photonic crystal fibers: symmetries and interference phenomena". *Optics Express*, 10(11), 2002.

[13] K. Okamoto. *Fundementals of optical waveguides*. Academic Press, 1992.

Chapter 7

Conclusions

The thesis details the investigation into various photonic structures with a interferometric scanning near-field optical microscope. This chapter provides a summary of the work presented including details of the most significant results.

As part of this project a SNOM system was developed capable of measuring the complex electric field in the near infrared. Details of the system are given in chapter 3. The control system enabled several different methods of scanning the fields above the surface, this is highlighted in chapter 6. Four different scanning techniques were employed to characterise the electric field at the output of a holey fibre.

A substantial part of the project was spent on the construction and development of the heterodyne detection system, similar to that developed by van Hulst and coworkers [1]. The heterodyne technique fulfilled a dual role, achieving optical detection with high gain, low noise and providing optical phase information. The system is relatively simple to implement, however reducing instabilities and noise required diligence and methodical analysis. The largest improvement being the painstaking thermal insulation of the equipment, this significantly reduced the effects of thermal drift and acoustic vibrations. The environmental isolation was capable

of providing an optical phase stability of 210 degrees/hour. The tunable diode laser and careful alignment of the optics permitted spectral operating range of 1500nm to 1640nm.

The most important component of any scanning probe microscope is the near-field probe, this defines the quality of the image. The fabrication process detailed in this thesis, is shown to be capable of producing reproducible probes with effective aperture sizes of $\approx$ 100nm. The necessity for high quality probes was demonstrated during the analytical investigation of waveguide loss in chapter 5.

Chapter 4 presented an investigation into the electric fields present within a fibre Bragg grating as a function of wavelength [2]. The investigation has for the first time, directly imaged some of the intrinsic features of fibre Bragg gratings, which have previously only been theoretically predicted. The most prominent result was the observation of the spatial shift in the location of the standing wave nodes by $\approx \lambda/4$. The shift shows the nodes of the standing wave moving from the lower index regions to the high index regions and is an explicit feature of fibre Bragg gratings. This result has broad scientific interest as the feature is also a property of photonic band gap systems [3]. The investigation also provided direct evidence for the internal Fabry-Perot modes suggested by Sipe *et al.* [4].

Interesting effects were also observed in the spectral regions where cladding modes are excited. The resultant standing waves provides information about the mode profile of the specific cladding mode. The imaging of the evanescent component of the mode was achieved by the partial removal of the fibre's cladding. As a result the structure of the cladding modes is not known, therefore making analytical analysis of the magnitude of the components difficult. It is hoped that future investigations may will be able to use D-fibres therefore producing better defined mode structures and quantify more of the features of fibre Bragg gratings.

This thesis also documents an analytical enquiry into the microscopic loss

of potassium ion exchange waveguides. Chapter 5 presents three potential methods of measuring the microscopic loss in waveguides. Two of which have been experimentally tested. The techniques exploit the standing wave generated in the waveguide due to the back reflection from the end face of the waveguide. The visibility of the standing wave provides sufficient information to determine the relative amplitudes of the counter propagating fields, from which the loss between two points may be derived. Due to the finite size and asymmetry of the SNOM probes the techniques were unable to measure the absolute fringe visibility [5].

Despite not being able to measure the absolute value of the visibility, the variation of the visibility around a microscopic defect was measured. The accuracy of the techniques were found to be limited by the instability of the system. The instability appeared to originate from two possible mechanisms, slow damage of the tip or fluctuations in the birefringence of the fibre probe. Further work is required to confirm the dominate mechanism. The instability of the system prevents the current SNOM system from being unable to accurately measure the loss. However, the investigation did however highlight the necessary requirements in order to develop the SNOM arrangement. Details of the proposed system are given in the future work section. A fully operating system in the future may provide a unique ability to determine the loss of individual components in an integrated photonic circuit.

The final chapter presented in this thesis presents an investigation into the mode profiles of a large mode area holey fibre. The chapter illustrates the use of SNOM to fully characterise the output mode of a holey fibre. This investigation was part of a larger research project of the modal properties of holey fibres [6].

The technique exploits the coated SNOM probes to sample the propagating mode of the holey fibre above the surface of the cleave. The work presented differs from that used in the previous chapters by measuring propagating light and thus has diffraction limited resolution. The SNOM

system provides an accurate and versatile technique, comparable to conventional measurement systems. To prevent the topographical artifacts associated with the microstructure of the fibre, the data was acquired using a constant height scanning technique. The results were compared to a theoretically predicted mode and showed an agreement of $\approx 7 - 10\%$. The error between the modes is expected to be the result of a mismatch between the core and the cladding material during fabrication.

The electric field was also acquired in the plane, normal to the end facet of the fibre. The results demonstrate the effect of propagation of the mode. The optical phase of the mode was found to have significant fluctuations above the holes of the fibre. These fluctuations were found to be the result of the high spatial frequencies of the mode, generated by the holey structure. The experimental results were again corroborated by a theoretically predicted model.

An underlying emphasis of this thesis is to prove the adeptness and versatility of this SNOM technique. This is demonstrated by the variety of the samples investigated. The project has shown that the SNOM can be used as an effective research tool capable of investigating fundamental mechanisms, such as in the fibre grating investigation. It has also been shown that it can be used as a characterisation tool for the investigation of photonic structures demonstrated by the investigations into the waveguide loss and holey fibres.

An important prerequisite for a successful SNOM investigation is the selection or preparation of a suitable sample. The work presented in this thesis has ensured that the topographical structure of the samples is minimal, thereby ensuring that the measured optical fields are an accurate representation of the underlying optical structure and not of the surface.

As photonics becomes increasingly dominated by structures with subwavelength features the role of near-field characterisation will become increasingly pertinent, and SNOM will be a key figure.

7.1 References

[1] M.L.M. Balistreri, J.P. Korterik, L. Kuipers, and N.F. van Hulst. "Phase Mapping of Optical Fields in Integrated optical waveguide structures.". *Journal of Lightwave Technology*, 19(8), 2001.

[2] J.C. Gates, J.D. Mills, and W. S. Brocklesby. "Near-field scanning optical microscopy of standing waves in fiber Bragg gratings.". *Applied Physics Letters*, 83(9):1890, 2003.

[3] J.D. Joannopoulos, R.D. Meade, and J.N. Winn. *Photonic Crystals*. Princeton University Press, 1995.

[4] J. E. Sipe, L. Poladian, and C. M. Desterke. "Propagation through Nonuniform Grating Structures". *Journal of the Optical Society of America a-Optics Image Science and Vision*, 11(4):1307–1320, 1994.

[5] S. I. Bozhevolnyi and E. A. Bozhevolnaya. "Near-field imaging of the interference pattern of counterpropagating evanescent waves". *Optics Letters*, 24(11):747–749, 1999.

[6] C. W. J. Hillman. *Scanning near-field optical microscope characterisation of microstructered optical fibre devices.* PhD thesis, University of Southampton, 2002.